

001311



**MICROSTRUCTURED OPTICAL FIBRES:  
FABRICATION, PROPERTIES, AND DEVICES**

by

Ping Lu

Master of Science

A Thesis Submitted in Partial Fulfillment of  
the Requirements for the Degree of

Doctorate of Philosophy

Department of Physics and Physical Oceanography  
Memorial University of Newfoundland

December 2011

St. John's

Newfoundland

## **Abstract**

In this thesis, several novel microstructured fibre-optic devices are investigated on their designs, fabrication techniques, characteristics, and applications. Firstly the dependences of the sensitivity and time response on the coating thickness of polyimide-coated fibre Bragg gratings (FBG) as well as factors influencing these properties are revealed. Intelligent sensing of multiple environmental parameters (salinity, saccharinity, and strain) with a single-fibre sensor system is achieved through the use of multiplexed FBGs with coatings of different polymers (acrylate and polyimide) and specifications. Simultaneous measurement of magnitude and direction of deflection using a FBG cantilever sensor with possible temperature compensation is realized based on Optical low-coherence reflectometry, which reveals the internal structure of the sensing FBG in correlation with its optical properties. Secondly, simultaneous wavelength locking and spectral filtering by a FBG embedded polarization maintaining fibre Sagnac loop mirror through temperature, strain, and polarization tuning is accomplished. The system is also applied to perform simultaneous temperature and axial strain measurement. Thirdly, various fibre Mach-Zehnder interferometers (FMZI) are fabricated using different light steering elements (fibre taper and fibre lateral-shifted junction) to form either a double elements (symmetrical and asymmetrical) or triple elements structure. Simultaneous measurement of temperature and refractive index or strain with a fibre Mach-Zehnder interferometry of high sensitivity is realized based on these FMZIs. Fourthly femtosecond laser induced micro-spots are fabricated inside optical fibres and their optical

characteristics are investigated. FMZIs consisting of the femtosecond laser induced spot and either a fibre taper or another spot are fabricated for measurement of temperature, strain, and refractive index. Lastly a femtosecond laser microfabrication approach is adopted to create several all-fibre devices such as long period fibre gratings, fibre core mode attenuators, fibre bandpass filter, and fibre mode converter. The method takes advantage of the flexibility of femtosecond laser micromachining and the specifications of these devices which can be arbitrarily modified by changing the femtosecond laser illumination parameters.

## Acknowledgements

I would like to thank my supervisor Dr. Qiying Chen for giving me the opportunity to work in his research group and for his continuous guidance. Dr. Qiying Chen offered me valuable direction in my academic and professional endeavors and gave me the freedom to explore new ideas related to my research project. I gratefully acknowledge Dr. Qiying Chen whose academic, professional, and personal support throughout my Ph. D. study, without which this work would not have been possible.

I would like to acknowledge and thank professors G. Todd Andrews and Luc Y. Beaulieu for serving in the committee and spending time on reviewing my work. I thank Dr. Liqiu Men for her assistance and helpful suggestions throughout my research project. I would also wish to express my sincere appreciation to several current and former research group members: Daiying Zhang, Van Nguyen, Yanfei Ding, Kevin Sooley, Matthew McDonald, Mark Penney, Adrian Gagnon, Matthew Ryan, and Douglas Greztic for their valuable collaboration, assistance, and discussion. I would also like to thank all the other faculty and staff of the Physics Department of Memorial University of Newfoundland for their experience and professionalism, which have supported my study and work significantly. I am grateful to thank the Department of Physics and Physical Oceanography, the School of Graduate Studies of Memorial University of Newfoundland, and my supervisor for financial support. In particular, I would like to thank Natural Sciences and Engineering Research Council of Canada for the award of the Vanier Canada Graduate Scholarship during the last two years of my Ph. D. study.

Special thanks go to my wife Jing Ping for her love and support, and my parents-in-law Donglin Ping and Zhiling Zou for their support and encouragement. Finally I would like to dedicate this work to my father Jiacheng Lu and my mother Hongying Li, for the countless years of love.

# Contents

Abstract	i
Acknowledgements	iii
Contents	v
List of Tables	vii
List of Figures	viii
List of Abbreviations	xv
<b>1 Introduction</b>	<b>1</b>
1.1 Optical Fibre Gratings	1
1.2 Optical Fibre Interferometers	7
1.3 Overview of Thesis	13
<b>2 Polymer-coated Fibre Bragg Grating</b>	<b>16</b>
2.1 Introduction	16
2.2 Tuning Sensing Response of Polymer-coated Fibre Bragg Grating	19
2.3 Multiparameter Sensing with Polymer-coated Fibre Bragg Grating	26
2.4 Deflection Measurement with Fibre Bragg Grating Cantilever Sensor	33
<b>3 Bragg Grating Imprinted Polarization Maintaining Fibre Loop Mirror</b>	<b>48</b>
3.1 Introduction	48
3.2 Wavelength Control with Grating Imprinted Fibre Loop Mirror by Polarization and Strain Tuning	50
3.3 Wavelength Locking and Spectral Filtering with Fibre Sagnac Loop Mirror by Temperature Tuning	59
3.4 Temperature and Strain Sensing with Fibre Sagnac Interferometer	65
<b>4 Tapered Optical Fibre Mach-Zehnder Interferometer</b>	<b>77</b>
4.1 Introduction	77

4.2	Symmetrical Fibre Mach-Zehnder Interferometer . . . . .	81
4.3	Asymmetrical Fibre Mach-Zehnder Interferometer . . . . .	87
4.4	Triple Tapered Fibre Mach-Zehnder interferometer . . . . .	105
<b>5</b>	<b>Microstructured Optical Fibre Fabricated by Femtosecond Laser</b>	<b>116</b>
5.1	Introduction . . . . .	116
5.2	Femtosecond Laser Modified Spot . . . . .	118
5.3	Femtosecond Laser Inscribed Fibre Interferometer . . . . .	134
<b>6</b>	<b>All Fibre Devices Fabricated with Femtosecond Laser</b>	<b>145</b>
6.1	Introduction . . . . .	145
6.2	Long Period Fibre Grating . . . . .	148
6.3	Fibre Core Mode Attenuator . . . . .	157
6.4	Fibre Bandpass Filter . . . . .	168
6.5	Fibre Mode Converter . . . . .	172
<b>7</b>	<b>Conclusions</b>	<b>180</b>
	<b>Bibliography</b>	<b>190</b>

## List of Tables

2-1 Comparison of OLCR method and Bragg wavelength monitoring method developed in this study with other recently reported bending/deflection measurement techniques . . . . .	47
4-1 Comparison of the performance of the reported FMZIs . . . . .	104
5-1 Comparison of the performance of different FMZIs fabricated in this study	141

## List of Figures

1-1 Illustration of a uniform fibre Bragg grating . . . . .	4
1-2 Illustration of a fibre Fabry-Perot interferometer. FC, fibre coupler; M, mirror . . . . .	7
1-3 Illustration of a fibre Michelson interferometer. FC, fibre coupler, M, mirror . . . . .	9
1-4 Illustration of a fibre Mach-Zehnder interferometer. FC, fibre coupler; CMEL, cladding mode excitation element . . . . .	10
1-5 Illustration of a fibre Sagnac interferometer. FC, fibre coupler; CW, clockwise; CCW, counterclockwise . . . . .	12
2-1 Transmission spectra of the polyimide-coated FBG-D with a coating thickness of 24 $\mu\text{m}$ at different degrees of salinity at 20 $^{\circ}\text{C}$ . The inset is an image of the fibre with dip-coated polyimide coating . . . . .	21
2-2 Dependences of the shifts in the Bragg wavelengths of the polyimide-coated FBGs on salinity. The polyimide coating thicknesses for FBG-A, -B, -C, and -D are 11, 17, 20, and 24 $\mu\text{m}$ , respectively. Inset shows the dependence of the salinity sensitivity on coating thickness . . . . .	23
2-3 Time-dependent evolutions of the normalized shifts in the Bragg wavelengths of the four polyimide-coated FBGs after transferred from an environmental salinity of 0 to 20% in solution: (a) experimental results, and (b) simulation . . . . .	25
2-4 Illustration of multiplexed FBGs coated with different polymers . . . . .	27
2-5 Polyimide-coated FBG for simultaneous saccharinity and salinity measurement (coating thickness 25 $\mu\text{m}$ ): (a) transmission spectra at different saccharinities with the inset on the Bragg wavelength as a function of saccharinity, and (b) shifts in the Bragg wavelength in response to the independent changes in saccharinity and salinity . . . . .	29
2-6 Polyimide-coated FBG for simultaneous saccharinity and salinity measurement (coating thickness 20 $\mu\text{m}$ ) with shifts in the Bragg wavelength in response to the independent changes in saccharinity and salinity . . . . .	30
2-7 Dependences of the shifts in the Bragg wavelengths of the acrylate- and polyimide-coated FBGs on temperature. The inset shows the redshifting transmission spectra of the acrylate-coated FBG with increasing temperature . . . . .	31
2-8 Schematic illustration of optical low-coherence reflectometry measurement of the FBG cantilever sensor . . . . .	34
2-9 Illustration of an FBG cantilever sensor in (a) pre-strained state and (b) stretched	

state	35
2-10 Simulation of the Bragg resonance wavelength as a function of the ratio of the deflection to the effective length	36
2-11 Low-coherence interferogram of the FBG used in this study. FBG is located between the air/fibre input facet and the fibre/IMG output facet	39
2-12 Interferogram close-up: (a) input air/fibre joint, (b) output fibre/IMG joint, and (c) FBG	40
2-13 Dependence of the fibre output joint position on the deflection measured by optical low-coherence reflectometry. The shift in the fibre output joint position indicates the elongation of the fibre during deflection	41
2-14 Dependence of the Bragg resonance wavelength of the cantilever-supported FBG on: (a) temperature around 20 °C, and (b) convex and concave deflections, respectively	43
2-15 Simulation of the Bragg resonance wavelength as a function of deflection at different neutral axis distances of 250 $\mu\text{m}$ , 1 mm, and 4 mm, respectively	44
3-1 Schematic illustration of the experimental setup for transmission spectrum measurement of the fibre loop mirror	51
3-2 Reflection spectrum of the fibre Bragg grating imprinted polarization maintaining fibre. The inset shows the cross section of a PANDA fibre	52
3-3 Simulated transmission spectra of the PMFBG in the Sagnac loop mirror at different polarization states: (a) 90°, (b) 70°, (c) 50°	53
3-4 Transmission spectrum switching from PMFBG filter to SLM comb filter by adjusting the polarization controller	53
3-5 Transmission spectra of the FBG-PMF in the fibre Sagnac loop mirror at 100 and 900 $\mu\text{e}$ . The inset shows the redshifting transmission spectra of the FBG-PMF from 100 $\mu\text{e}$ to 900 $\mu\text{e}$	56
3-6 Axial strain dependences of the PMFBG Sagnac loop mirror. The solid circles and open circles stand for the Bragg resonance wavelengths of the slow axis and the fast axis as a function of axial strain, respectively. The solid squares represent the fibre SLM interferometric peak wavelength as a function of axial strain for $k = 420$	57
3-7 Schematic illustration of the experimental setup. PC, polarization controller; FC, fibre coupler; HT, heating tube	60
3-8 Left: Transmission spectra of the FBG-PMF Sagnac loop mirror at 20°C and 60°C. Right: The enlarged curves show the redshifts in the Bragg wavelengths of the FBG along both the slow and fast axes	62
3-9 Temperature dependences of the FBG-PMF Sagnac loop mirror. The dots stand for the Bragg resonance wavelengths of the FBG along either the slow axis or the fast axis. The triangles represent the interferometric peak wavelengths of the SLM with $k = 420$	64
3-10 Schematic illustration of the experimental setup for transmission spectrum measurement of the fibre Sagnac interferometer with PMFBG at different input light polarization states. PC, polarisation controller; FOC, fibre-optic coupler; CW, clockwise; CCW, counterclockwise.; LPA, lightwave polarization analyzer	66
3-11 Left: The Agilent 8509C measurement screen. Right: Reflection spectrum of PMFBG when the polarization state of PC1 was aligned to the fast-axis. Inset in the	

	right figure shows the enlarged reflection spectrum of PMFBG . . . . .	67
3-12	Left: The Agilent 8509C measurement screen. Right: Reflection spectrum of PMFBG when the polarization state of PC1 was aligned to the slow-axis . . . . .	68
3-13	Left: The Agilent 8509C measurement screen. Right: Reflection spectrum of PMFBG when the polarization state of PC2 was aligned to the fast-axis . . . . .	68
3-14	Left: The Agilent 8509C measurement screen. Right: Reflection spectrum of PMFBG when the polarization state of PC2 was aligned to the slow-axis . . . . .	69
3-15	Transmission spectrum of the Sagnac interferometer with reflection spectrum of the PMFBG (a) and (b): PC1 and PC2 are set to the same polarization states along either the fast axis or the slow axis of the PM fibre; (c) and (d): PC1 and PC2 are set to the orthogonal polarization states, one along the fast axis and the other along the slow axis of the PM fibre . . . . .	70
3-16	Schematic illustration of the experimental setup for simultaneous measurement of temperature and axial strain . . . . .	71
3-17	Transmission spectra of the PMFBG in the fibre Sagnac interferometer under different temperatures and axial strains . . . . .	72
3-18	Transmission spectra of the PMFBG under different temperatures and axial strains . . . . .	73
3-19	The slow-axis and fast-axis Bragg wavelengths (solid symbols) as well as fibre Sagnac interferometer resonance peak wavelengths of $k = 401$ and $k = 411$ (hollow symbols) as functions of temperature under different axial strain values. $\square/\square$ , $0 \mu\epsilon$ ; $\blacktriangle/\triangle$ , $200 \mu\epsilon$ ; $\blacktriangledown/\triangledown$ , $400 \mu\epsilon$ ; $\star/\star$ , $600 \mu\epsilon$ ; $\bullet/\circ$ , $800 \mu\epsilon$ ; $\blacklozenge/\lozenge$ , $1000 \mu\epsilon$ . . . . .	74
4-1	Schematic illustration of the experimental setup. Inset is a photo of a tapered fibre fabricated in this study with parameters of $D_0 = 65 \mu\text{m}$ and $L_0 = 525 \mu\text{m}$ . . . . .	82
4-2	Attenuation spectra of the fibre Mach-Zehnder interferometer at different environmental conditions: (a) in air at $20^\circ\text{C}$ , (b) in water at $20^\circ\text{C}$ , (c) in 20 wt% KCl solution at $20^\circ\text{C}$ , and (d) in water at $60^\circ\text{C}$ . . . . .	84
4-3	Dependences of the shifts of the attenuation peak wavelengths on refractive index and temperature for the interference orders $m_1$ and $m_2$ . . . . .	86
4-4	(a) Schematic illustration of the fibre device developed in this study, (b) experimental setup with the left and right insets showing the optical micrographs of the fibre taper (P) and the lateral-shifted junction (J) in the interferometer, respectively . . . . .	88
4-5	Simulation of light energy density distribution along (a) a fibre taper ( $D_0 = 70 \mu\text{m}$ , $l_0 = 500 \mu\text{m}$ ) and (b) a lateral-shifted junction ( $d_0 = 5 \mu\text{m}$ ) at $\lambda = 1.55 \mu\text{m}$ . . . . .	89
4-6	(a) Attenuation spectra of single fibre tapers (P) with different length/diameter ratios ( $l_0/D_0$ ) and single lateral-shifted junctions (J) with different parameters ( $d_0$ ), (b) attenuation spectra of J+P type aFMZIs with different parameters, (c) the dependences of breaking strain limit on the waist diameter of the fibre taper, and (d) attenuation spectra of the aFMZI of J( $4 \mu\text{m}$ )+P( $580 \mu\text{m}/60 \mu\text{m}$ ) at different SOP . . . . .	91
4-7	Attenuation spectra of J+P and P+J type aFMZIs with different interferometer lengths: (a) 2 cm, (b) 5 cm, (c) 20 cm, and (d) the dependence of wavelength spacing on the interferometer length for the two types of aFMZI . . . . .	94
4-8	Spatial frequency spectra of J+P type aFMZIs with different interferometer lengths: (a) 2 cm, (b) 5 cm, (c) 20 cm, and (d) the dependences of spatial frequency on the	

interferometer length and cladding mode effective refractive index (RI) for the aFMZI of 20 cm in length . . . . .	95
4-9 Attenuation spectra of aFMZIs at different environmental temperatures: (a) P+J type, (b) J+P type, and (c) the dependences of the shifts in the attenuation peak wavelengths of the two types of aFMZI on temperature at different interference orders without strain . . . . .	98
4-10 Attenuation spectra of the aFMZIs under different axial strains: (a) P+J type, (b) J+P type, and (c) the dependences of the shifts in the attenuation peak wavelengths of the two types of aFMZI on axial strain at different interference orders at 20°C . . . . .	100
4-11 (a) Attenuation spectrum of a single fibre taper and triple tapered fibre interferometer consisting of Taper-1. (b) Spatial frequency spectrum of the triple tapered fibre interferometer. Inset of (b) is a schematic illustration of the triple tapered fibre interferometer with an optical micrograph of Taper-1 . . . . .	107
4-12 (a) Attenuation spectrum of a single fibre taper and triple tapered fibre interferometer consisting of Taper-2. (b) Spatial frequency spectrum of the triple tapered fibre interferometer. Inset of (b) is a schematic illustration of the triple tapered fibre interferometer with an optical micrograph of Taper-2 . . . . .	109
4-13 Spatial frequency spectrum of the triple fibre taper interferometer (Taper-2 + Taper-1 + Taper-2). Inset of (a) is the corresponding attenuation spectrum . . . . .	111
4-14 Spatial frequency spectrum of the triple fibre taper interferometer (Taper-1 + Taper-2 + Taper-1). Inset of (b) is the corresponding attenuation spectrum . . . . .	112
4-15 Attenuation spectrum of the triple fibre taper interferometer (Taper-1 + Taper-2 + Taper-1) at different temperature . . . . .	113
4-16 Spatial frequency spectrum at different temperatures. Insets are the magnified regions at three intensity peaks (A, B, and C) . . . . .	114
4-17 Dependence of the spatial frequency shift on temperature . . . . .	114
5-1 Schematic illustration of the femtosecond laser microfabrication system. M, mirror; BE, beam expander (magnification, 2 $\times$ ); BS, beam splitter; OL, objective lens (magnification 50 $\times$ , NA 0.80). Inset is a scheme of the fibre interferometer . . . . .	119
5-2 Schematic illustration of the experimental setup for sensing test. Insets are optical micrographs of a fibre taper and a femtosecond laser trimmed spot . . . . .	120
5-3 Attenuation spectra of a fibre with a single femtosecond laser trimmed spot, a single fibre taper, and a FMZI consisting of a fibre taper and a femtosecond laser trimmed spot spaced 30 mm apart . . . . .	122
5-4 Shifts in the attenuation spectra of the FMZI at (a) temperature of 20 °C and 100 °C, (b) axial strain of 0 and 2000 $\mu\epsilon$ . . . . .	123
5-5 Dependences of the shifts in the attenuation peak wavelengths of the FMZI at two interference orders of $m_1$ and $m_2$ on temperature and axial strain . . . . .	125
5-6 Top views of a femtosecond laser microfabricated spot (left) and a fibre taper made by a fusion splicer (right) . . . . .	127
5-7 Attenuation spectra of the FMZI at different (a) KCl solution concentrations and (c) temperatures. Dependences of the shifts in the attenuation peak wavelengths of the FMZI on (b) environmental refractive index and (d) temperature of different interference orders . . . . .	127

5-8 (a) Attenuation spectra of a fibre with a taper only and of a fibre with an ultrafast laser microfabricated spot only. Insets are the optical micrographs of a taper and a spot, respectively. (b) Attenuation spectra of a 10-mm-long fibre interferometer consisting of the taper and the spot at different environmental conditions (temperature, axial strain, and environmental refractive index) . . . . .	131
5-9 Attenuation spectra of fibre interferometers consisting of a taper and a femtosecond laser microfabricated spot with a spatial separation of (a) 15 mm, (b) 20 mm, (c) 25 mm, and (d) 30 mm, respectively . . . . .	132
5-10 Dependences of the shifts in the attenuation peak wavelengths of different fibre interferometers on (a) temperature, (b) axial strain, and (c) refractive index, respectively. (d) Temperature, axial strain, and refractive index sensitivities measured at certain attenuation peak wavelengths . . . . .	133
5-11 (a) An optical micrograph of a femtosecond-laser-irradiated single-mode optical fibre (top-view). Left and right insets are the near-field profiles of the single-mode fibre without and with a femtosecond-laser-irradiated spot. (b) SEM images of the femtosecond-laser-irradiated single-mode optical fibre without polymeric coating (left, top-view; and right, cross-section). (c) Two-dimensional finite element simulation on the distribution of light energy density along the femtosecond-laser-irradiated spot. (d) Dependence of the scattering efficiency factor $Q$ on the scattering sphere quality factor $\eta$ . Insets are simulated scattered fields by scattering spheres with different radii . . . . .	135
5-12 Attenuation spectra of FMZIs fabricated with femtosecond laser pulse energy of 20 $\mu\text{J}$ and irradiation duration of 6 s under different objective lenses: (a) 100 $\times$ (NA 0.95), (b) 50 $\times$ (NA 0.80), (c) 40 $\times$ (NA 0.65), (d) 20 $\times$ (NA 0.46), and (e) 20 $\times$ (NA 0.30). (f) shows the attenuation spectra of the FMZI fabricated with a 50 $\times$ objective lens (NA 0.80) and laser irradiation duration of 15 s. The insets are optical micrographs of the femtosecond laser irradiated spots (top-view). (g) shows the relations between the attenuation coefficient $\alpha$ and refractive index change $\Delta n$ , radius $r$ , wavelength $\lambda$ , at different values of the scattering index factor $\eta$ . . . . .	138
5-13 (a) Attenuation spectrum of a FMZI fabricated with femtosecond laser pulse energy of 20 $\mu\text{J}$ and irradiation duration of 20 seconds under a 50 $\times$ objective lens (NA 0.80). (b) Attenuation spectra of the FMZI without axial strain at 20 $^{\circ}\text{C}$ and 100 $^{\circ}\text{C}$ , respectively. (c) Attenuation spectra of the FMZI at 20 $^{\circ}\text{C}$ with axial strains of 0 and 2000 $\mu\text{e}$ , respectively. (d) Dependences of the attenuation peak wavelength of the FMZI on temperature and axial strain . . . . .	142
6-1 Schematic illustration of the femtosecond laser microfabrication system . . . . .	150
6-2 Schematic illustration of a long period fibre grating LPG-A with the optical micrograph of a single femtosecond laser irradiated spot . . . . .	151
6-3 Transmission spectrum of the long period grating LPG-A . . . . .	152
6-4 Schematic illustration of a long period fibre grating LPG-B with the optical micrograph of several femtosecond laser irradiated grating planes . . . . .	153
6-5 (a) Transmission spectrum of the LPG-B. (b) Transmission spectrum of a specific transmission dip of the LPG-B. Inset shows the enlarged curve of the transmission dip . . . . .	154

6-6	Schematic illustration of a long period fibre grating LPG-C with the optical micrograph of a femtosecond laser irradiated grating plane . . . . .	155
6-7	(a) Transmission spectra of the LPG-C at 20 °C and 200 °C. (b) Dependence of the wavelength shifts of the resonance peaks of the LPG-C on temperature . . . . .	157
6-8	Schematic illustration of femtosecond laser pulses induced refractive index modification region on the single-mode optical fibre core along the fibre axis . . .	158
6-9	(a) Schematic illustration of femtosecond laser Gaussian beam focused at different positions inside the single-mode optical fibre. (b) Attenuation spectrum of a single-spot SMF-CMA, insets are near-field images of a pristine single-mode fibre (top) and the SMF-CMA (bottom). (c) Attenuation change with different radial distances at 1540 nm and 1590 nm, respectively. (d) Attenuation change with different focus positions at 1540 nm and 1590 nm, respectively. Insets of (c) and (d) are top-viewed and side-viewed optical micrographs of the single-spot SMF-CMA, respectively	160
6-10	Simulation of energy density distribution inside the single-mode fibre with different configurations . . . . .	162
6-11	(a) Attenuation spectra of a single-spot SMF-CMA with different laser irradiation durations. (b) Attenuation spectra of a single-spot SMF-CMA with different laser pulse energies . . . . .	163
6-12	Attenuation spectra of multiple-spot SMF-CMAs of a spot interval of 200 $\mu\text{m}$ with different spot numbers (a) pulse energy of 7.5 $\mu\text{J}$ , irradiation time of 10 s, (b) pulse energy of 22.5 $\mu\text{J}$ , irradiation time of 10 s, (c) pulse energy of 7.5 $\mu\text{J}$ , irradiation time of 90 s. (d) Attenuation spectrum of a five-spot SMF-CMA with different spot intervals (pulse energy of 7.5 $\mu\text{J}$ , irradiation time of 10 s) . . . . .	164
6-13	Attenuation spectra of a single-spot SMF-CMA fabricated using different objective lenses. Insets are top-viewed optical micrographs of the SMF-CMA using 100 $\times$ (bottom) and 20 $\times$ (top) objective lenses, respectively . . . . .	166
6-14	(a) Schematic illustration of femtosecond laser crafted SMF-CMAs with and without a middle coating segments. (b) Attenuation spectra of the five-spot SMF-CMAs with and without a middle coating segments. (c) Transmission spectra of the five-spot SMF-CMA and pristine SMF with the middle coating segment . . . . .	167
6-15	Schematic illustration of an all-fibre bandpass filter . . . . .	168
6-16	Measured transmission spectra of LPG-1. Inset is a scheme of the long period fibre grating . . . . .	169
6-17	Measured transmission spectrum of single mode fibre with and without core mode attenuator . . . . .	170
6-18	Transmission spectra of LPG-2 and fibre bandpass filter . . . . .	171
6-19	Schematic illustration of the optical fibre mode converter. Inset is the optical micrograph of the femtosecond laser inscribed line . . . . .	173
6-20	(a) - (c) Transmission spectra of femtosecond laser fabricated optical fibre mode converters. Insets are near-field mode profile measurement setup, optical fibre device structures, as well as corresponding near-field images and three-dimensional near-field patterns. (f) Relative transmission spectra of femtosecond laser fabricated optical fibre mode converters . . . . .	174
6-21	Top left, simulation of light energy density distribution through a fs-laser line and a	

coating region at $\lambda = 1.55 \mu\text{m}$ . Top right, illustration of the mode conversion process at different fibre device structures. Bottom, two-dimensional near-field patterns for different structures measured at different wavelengths . . . . .	177
6-22 Transmission spectrum of the optical fibre mode converter consisting of two femtosecond laser inscribed line without a middle coating region. Insets are near-field images at different wavelengths . . . . .	178

## List of Abbreviations

aFMZI	Asymmetrical fibre Mach-Zehnder interferometer
B	Birefringence
BBS	Broadband light source
BE	Beam expander
BS	Beam splitter
CCW	Conterclockwise
CMA	Core mode attenuator
CMEL	Cladding mode excitation element
CW	Clockwise
F-P	Fabry-Perot
FBG	Fibre Bragg grating
FC	Fibre coupler
FFT	Fast Fourier transformation
FMZI	Fibre Mach-Zehnder interferometer
FOC	Fibre-optic coupler
FOG	Fibre optic gyroscope
FSI	Fibre Sagnac interferometer
GPIB	General-purpose interface bus
HT	Heating tube
IMG	Index-matching gel
IR	Infrared
KrF	Krypton fluoride
LP	Linear polarization
LPA	Lightwave polarization analyzer
LPG	Long period grating
M	Mirror
MFD	Mode field diameter
NA	Numerical aperture
OCT	Optical Coherence Tomography
OL	Objective lens
OLCR	Optical low coherence reflectometry
OSA	Optical spectrum analyzer
PC	Polarization controller
PCF	Photonic crystal fibre

PMF	Polarization maintaining fibre
RI	Refractive index
sFMZI	Symmetrical fibre Mach-Zehnder interferometer
SLM	Sagnac loop mirror
SMF	Single-mode fibre
SOP	States of polarization
SPR	Surface plasmon resonance
UV	Ultraviolet
WDM	Wavelength division multiplexed

# Chapter 1

## Introduction

Since the development of the low loss optical fibre in the early 1970's, optical fibres have become a key component in modern telecommunication systems and sensor networks. During the past decades, great efforts have been devoted to the development of new types of optical fibres to improve the performance in these applications. Novel microstructured optical fibres have attracted considerable research interest around the world due to their versatile properties. This thesis studies different types of microstructured optical fibres as well as their fabrication, properties, and device applications. A few optical fibre technologies emerged recently will be discussed in the following sections.

### 1.1 Optical Fibre Gratings

A conventional optical fibre consists of three layers: core, cladding and protective outer

coating. The core is typically a doped silica material which forms the centre of the fibre and carries the light. The cladding is the middle layer of slightly lower refractive index, which serves to confine the light to the core because of total internal reflection. There may be one or several layers of protective outer coating outside the cladding which is made of polymer materials. The coating layer increases the mechanical strength of the optical fibre and seals it against moisture or contaminations. The optical transmission characteristics of optical fibres mainly depend on the properties of the core and cladding. The numerical aperture (NA) of the optical fibre is used to define the light gathering ability of the fibre that light entering the core from within the acceptance cone will be propagated based on total internal reflection and light entering from outside the acceptance cone will not be transmitted. Optical fibres can be classified as step-index and graded-index fibres according to the radial profile of the core refractive-index. Both the step-index and graded-index fibres can be further divided into single-mode and multi-mode classes. In a step-index fibre, the refractive index of the core is uniform in the core and has an abrupt change at the core-cladding boundary. In a single-mode fibre the core is so small that only one single mode of light is permitted. In a multimode fibre light can propagate in many different modes. The larger core area of the multimode fibre makes it easier to couple optical power into the fibre and to splice two fibres together compared to the small core single-mode fibre.

With the increasing interests in the studies of all-fibre systems, fibre Bragg gratings (FBGs) have received considerable attention recently. A FBG is a type of distributed Bragg reflector constructed in a short segment of optical fibre that reflects specific

wavelengths of light and transmits all the other components. The first FBG was imprinted in Ge-doped silica single mode fibre by transverse coherent 244 nm ultraviolet (UV) beams produced by a tunable excimer-pumped dye laser with a frequency-doubled crystal [1]. Since then, FBGs have been revolutionizing telecommunication and impacting the optical fibre sensor field due to their unique advantages and versatility as in-fibre devices. Nowadays FBGs have become important components in a variety of lightwave communication applications such as fibre laser [2, 3], fibre amplifier [4], fibre Bragg filter [5-8], the wavelength division multiplexer/demultiplexer [9, 10], and dispersion compensator [11]. Meanwhile FBGs have been considered as excellent sensor elements which are suitable for measuring many environmental parameters, including temperature and strain [12], torsion and bending [13], refractive index [14], pressure [15], current [16] and solution concentration [17].

A FBG consists of a periodic modulation of the refractive index in the core of an optical fibre. The phase fronts of this type of fibre gratings are perpendicular to the fibre longitudinal axis and the grating planes are of a constant period (Fig. 1-1). Light guided along the core of an optical fibre will be scattered by each grating plane. The Bragg grating condition is simply the requirement to satisfy both energy and momentum conservation, with a simplified expression of the first-order Bragg condition  $\lambda_B = 2n_{eff}\Lambda$ , where  $\Lambda$  is the spacing between the grating planes,  $\lambda_B$  is the centre wavelength of the input light that will be back-reflected from the Bragg grating, and  $n_{eff}$  is the effective refractive index of the fibre core at the free-space centre wavelength. If the Bragg condition is not satisfied, the reflected light from each of the subsequent planes becomes progressively

out of phase and will eventually cancel out. When the Bragg condition is satisfied, the contributions of reflected light from each grating plane add constructively in the backward direction to form a back-reflected peak with a centre wavelength defined by the grating parameters, which is usually referred to as Bragg wavelength.

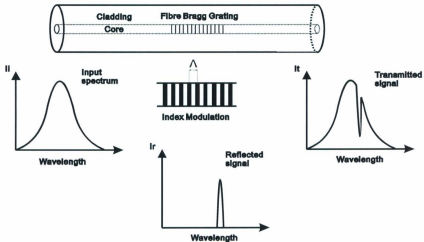


Figure 1-1: Illustration of a uniform fibre Bragg grating.

Photosensitivity in optical fibre refers to a permanent change in the index of refraction of the fibre core when exposed to light with characteristic wavelength and intensity that depends on the core material. Photosensitivity phenomenon in optical fibres was first observed by the interference between counter-propagating waves inside the fibre core in 1978 [18]. Several models have been proposed for these photoinduced refractive-index changes, for instance, the color centre model [19, 20], the dipole model [21], the compaction model [22], and the stress-relief model [23-25]. The only common elements in these theories are that the germanium-oxygen vacancy defects, Ge-Si or

Ge-Ge, are responsible for the photoinduced index changes. Photosensitivity of optical fibres can be thought of as a measure of the amount of refractive index change in a fibre core and it is desirable to fabricate photoinduced devices in standard optical fibres for compatibility with the existing systems. Different FBG fabrication techniques can be classified as internal inscription and external inscription techniques. Bragg gratings were first fabricated using the internally writing technique [18, 26]. In recent years, direct optical inscription of high quality gratings into the core of optical fibres has been achieved by various techniques, in which three leading techniques have been reported, such as interferometric technique [1], phase mask technique [27, 28], and point-by-point exposure to ultraviolet laser light [29]. According to the difference in either the grating pitch or grating plane orientation, fibre Bragg gratings can be categorized into the common Bragg reflector [30-33], the blazed Bragg grating [34, 35], and the chirped Bragg grating [36-41].

Long period grating (LPG) is another important optical component in optical communication systems, which couples the forward propagating fundamental mode in the core of a single-mode fibre into the multiple forward propagating cladding modes at specific wavelengths. The light coupled into the cladding attenuates rapidly as it propagates along the fibre due to the radiation of the cladding modes. The coupling between the fundamental core mode and the cladding modes occurs when the phase matching condition of long period gratings is satisfied [42],  $\beta_{01} - \beta_{mn} = 2\pi/\Lambda = K$ , where  $\beta_{01}$  is the propagation constant of the fundamental linearly polarized (LP<sub>01</sub>) core-guided mode,  $\beta_{mn}$  is the propagation constant of the fundamental linearly polarized (LP<sub>mn</sub>)

cladding-guided mode,  $\Lambda$  is the grating period, and  $K$  is the grating vector magnitude. An alternative form of the phase-matching condition is given by  $\lambda_{res} = \Lambda(n_{01} - n_{m1})$ , where  $n_{01}$  is the effective index of the core-guided mode,  $n_{m1}$  is the effective index of the LP<sub>m1</sub> cladding-guided mode, and  $\lambda_{res}$  is the centre wavelength of the transmission resonance. Since both propagation constants are the forward-propagation modes, they have the same direction and the magnitudes are not quite different. Because of the small difference between the two propagation constants, the grating period of a long period grating, typically on the order of hundreds of micrometers, is much larger than that of a fibre Bragg grating.

Amplitude mask technique is a regular method for inscribing long period grating [42]. The optical fibre is exposed to ultraviolet radiation through an amplitude mask which has a rectangular transmission function of an appropriate period fabricated in silica or metal. Several non-UV based grating fabrication mechanisms have also shown the capability of inducing periodic refractive index perturbation in the optical fibres, such as thermal effects by CO<sub>2</sub> laser or electric arc, photo-elastic effects by cladding etching, and femtosecond laser irradiation [43-46]. Long period gratings are highly sensitive to external perturbation such as temperature, strain and bending, which has also led to much interest for sensing applications [47, 48]. Due to their low-cost and all-fibre nature, long period gratings have also been widely used as tunable wavelength filters and other optical fibre devices in optical communications [49-51].

## 1.2 Optical Fibre Interferometers

Interferometric-based optical fibre devices take advantage of merits inherent to the interferometric nature for applications in telecommunications, sensors, medical images, and instrumental tests. Optical fibre interferometers are optical devices which utilize the effect of interference and are implemented with optical fibres and fibre couplers. Phase shift induced by perturbing environment in one fibre relative to the other can be detected precisely by an optical fibre interferometer. There are mainly four interferometric configurations: Fabry-Perot, Michelson, Mach-Zehnder, and Sagnac.

A fibre Fabry-Perot (F-P) interferometer includes two reflectors along the length of an optical fibre illustrated in Fig. 1-2. The Fabry-Perot interferometer is a multiple beam interference device in which the output depends on the successive multiple reflections of an input beam between two mirrors which form a Fabry-Perot etalon.

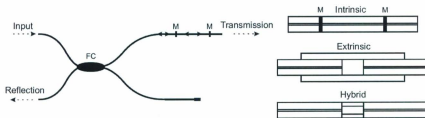


Figure 1-2: Illustration of a fibre Fabry-Perot interferometer. FC, fibre coupler; M, mirror.

According to different fibre optic configurations, fibre Fabry-Perot interferometers can be categorized into intrinsic Fabry-Perot interferometers, extrinsic F-P interferometers, and hybrid F-P interferometers shown in Fig. 1-2. The intrinsic F-P

interferometers consist of two reflectors inside the optical fibre which can be fabricated with several methods such as dielectric thin-films [52] and fibre Bragg gratings [53]. Extrinsic F-P interferometers normally comprise a lead-in fibre and a reflection mirror, for example an air cavity between two cleaved fibre ends, which are inserted into an alignment ferrule and bonded by laser welding [54]. A hybrid F-P interferometer can be fabricated by splicing a hollow core fibre in between two sections of fibre [55, 56]. The hybrid one combines the advantages of intrinsic and extrinsic F-P sensors, such as the improved mechanical strength and easy fabrication process. Fibre-optic Fabry-Perot interferometers have been widely used in sensing applications such as strain, temperature, pressure, acoustic waves, vibration, and flow sensors [57-65]. The advantages of Fabry-Perot interferometer sensors include high sensitivity, large dynamic range, ease of fabrication, high stability since light is transmitted to and from the sensor through the same fibre. Based on phase modulation, Fabry-Perot interferometer sensors are immune to optical power fluctuations. Similar structures have also been used for the construction of different tunable filters, such as fibre Fabry-Perot filters or lasers [66-68], because of their simple structure, compact size and insensitivity to environment changes.

A Michelson interferometer splits a broadband light source into a reference arm and a sample arm shown in Fig. 1-3. The reflected light from two mirrors in the two arms recombines to form an interference signal. The coherence length is the distance over which a correlation exists within the phase of an electromagnetic wave. The constructive interference in a Michelson interferometer occurs when the distance difference between the two arms of the interferometer is less than the coherence length of the light source.

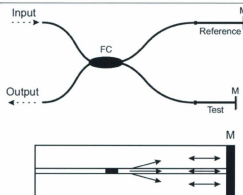


Figure 1-3: Illustration of a fibre Michelson interferometer. FC, fibre coupler; M, mirror.

Optical low coherence reflectometry (OLCR) is a white light interferometric technique based on the use of a Michelson interferometer to measure the position and magnitude of the interference fringes created by the interaction of light reflected from a sample and a moving mirror. OLCR is an interferometric technique to evaluate the structural and optical properties of materials and devices with a high spatial resolution, high reflection sensitivity, and a large dynamical range [69-71]. OLCR has been applied in medical imaging, which has resulted in the realization of a new imaging technique, Optical Coherence Tomography (OCT), in 1991 [72]. In OCT, an image is created from a series of individual OLCR measurements. These measurements are taken by moving a fibre-optic probe along the surface of the sample, and by focusing light to the depth of interest. The contrast in the created images is attributed to the varying intensity of light reflected from different tissue elements found at those depths [73-75].

Another implementation of the interferometric structure is the Mach-Zehnder

interferometer which uses one fibre coupler to split light into two optical fibres of two arms and combine them using the other fibre coupler illustrated in Fig. 1-4. Fibre Mach-Zehnder interferometer (FMZI) can be divided into two main categories, multiple optical fibre type in which the light splits and enters the reference and test fibres and is modulated separately in the test arm before being relaunched into the same fibre [76-78] and single optical fibre type in which the optical beam always remains within the same optical fibre and is guided to the measurement point through different optical fibre modes [79].

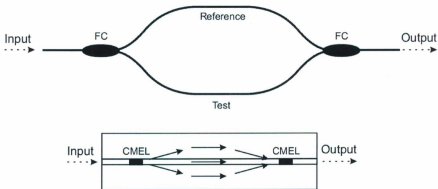


Figure 1-4: Illustration of a fibre Mach-Zehnder interferometer. FC, fibre coupler; CMEL, cladding mode excitation element.

In the FMZI of single optical fibre type, light travelling through the optical fibre encounters a cladding mode excitation element and a part of the optical power couples into the cladding mode, while the residue remains in the core and propagates as the fundamental core mode. When the two modes in the fibre core and cladding layers encounter at the position of another cladding mode excitation element, mode coupling

takes place which results in the creation of an interference fringe. Among different fibre-optic techniques, fibre Mach-Zehnder interferometers of single optical fibre type exhibit salient merits of high sensitivity, high degree of integration, simplicity and compact in-line measurement for applications ranging from waveguiding, routing, filtering, nonlinear optical probing to sensing [80-88]. Different structures of the single optical fibre Mach-Zehnder interferometers have been developed, such as a fibre-taper section between a LPG pair [80], spliced two pieces of a photonic crystal fibre (PCF) with a small lateral offset or collapsed air-holes of a single PCF [81], two core-offset attenuators on a single-mode fibre [82], two tandem fibre tapers by fusion splicing [83], two points on a single-mode fibre by CO<sub>2</sub> laser irradiations [84], a fibre multimode interferometric structure combined with a LPG [85], a nonadiabatic taper cascaded with a LPG [86], interaction of a misaligned fusion-spliced point with a LPG on a single-mode fibre [87], or on a PCF [88].

A fibre Sagnac interferometer consists of a fibre coupler whose output ports are connected by a fusion splice to form a loop shown in Fig. 1-5. The input beam is split by the fibre coupler into two beams traveling along the same fibre path, but in opposite directions. One beam propagates in the clockwise direction, and the other one propagates in the counter-clockwise direction. Upon completion of one round trip, the two beams are recombined in the fibre coupler to form a fibre Sagnac loop interferometer.

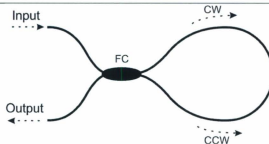


Figure 1-5: Illustration of a fibre Sagnac interferometer. FC, fibre coupler; CW, clockwise; CCW, counterclockwise.

A polarization maintaining optical fibre (PMF) is an optical fibre in which the polarization planes of light waves launched into the fibre are maintained during propagation with little or no cross-coupling of optical power between the polarization modes. When the PMF is integrated into a Sagnac interferometer structure, these fibres can be applied in optical sensing field, especially the use as a fibre optic gyroscope (FOG) which can measure instantaneously the rotational speed of a mobile objective based on the Sagnac effect discovered by Georges Sagnac in 1917. In optical sensing, besides the gyroscope application [89, 90], fibre Sagnac interferometer has been used in the measurement of many single parameters, such as temperature [91, 92], strain [93, 94], bending [95], and liquid level [96]. Simultaneous measurement of temperature and strain based on a configuration using fibre Sagnac interferometer have been realized [97-101]. The Sagnac interferometer is sensitive to disturbances of the optical path length of a fibre loop and the sensitivity is proportional to the distance of the perturbation point from the centre of the loop. Thus a Sagnac loop interferometer has also been applied in distributed

impact sensing. The location and amplitude of a time varying disturbance can be determined with potentially high sensitivity and time response speed [102-105]. A fibre Sagnac interferometer can also be used for producing comb filters and designing multi-wavelength fibre lasers to generate multiple wavelength lasing for applications in wavelength division multiplexed (WDM) communications and sensor systems [106-110]. It has the advantages of simple design, low cost, low insertion loss, polarization independence to input light and high resistance to environmental changes. An all-fibre comb filter based on a Sagnac interferometer with a FBG asymmetrically located inside a fibre loop for lasing multiple-wavelength has been reported [103]. Tunable filters and multiple wavelength lasers based on a fibre loop mirror structure using different kinds of PMF have been proposed and demonstrated [104-106].

### 1.3 Overview of Thesis

The objective of this thesis is to investigate microstructured optical fibres on their fabrication, characterization, and development. This study will facilitate the creation of important optical fibre components for applications in optical sensing. The thesis is divided into seven chapters with an introduction to give a brief review of optical fibre gratings and optical fibre interferometers in the first chapter.

Chapter 2 describes an application of polyimide-coated fibre Bragg grating as a substance sensor and an approach to achieve intelligent sensing of multiple environmental parameters with a single-fibre sensor system through the use of multiplexed fibre Bragg

gratings with coatings of different polymers and specifications. Optical low-coherence reflectometry for deflection measurement with FBG cantilever sensor will also be discussed in Chapter 2.

Chapter 3 presents approaches to achieve simultaneous wavelength locking and spectral filtering by the use of fibre Bragg grating embedded polarisation maintaining fibre Sagnac loop mirror through three techniques, i.e. temperature tuning, polarization and strain tuning. In the last part of this chapter, a fibre Sagnac interferometer with an integrated polarization maintaining fibre Bragg grating is fabricated to achieve simultaneous temperature and axial strain measurement.

In Chapter 4, simultaneous measurement of temperature and refractive index or axial strain by using a Mach-Zehnder interferometer based on tapered single-mode optical fibre or a tapered fibre and a fibre lateral shift-junction is achieved. A triple tapered fibre Mach-Zehnder interferometer with a configuration of three fibre tapers of different sizes is fabricated and temperature sensing function is realized by analyzing in the spatial frequency domain by taking the fast Fourier transformation of the attenuation spectra.

In Chapter 5, a femtosecond laser modified spot on a single mode fibre is extensively investigated. A combination of a femtosecond-laser-irradiated spot and an electrical arc induced fibre microstructure as a fibre Mach-Zehnder interferometer for sensing applications is studied. Chapter 5 also illustrates an approach to fabricate a compact fibre Mach-Zehnder interferometer by two femtosecond laser irradiated spots.

In Chapter 6, fabrication of long period fibre gratings and single-mode optical fibre core mode attenuator by point-by-point femtosecond laser irradiations is proposed and

experimentally demonstrated. A method for making a bandpass filter consisting of a core mode attenuator between two identical long period fibre gratings by point-by-point femtosecond laser exposure is presented. An optical fibre mode converter consisting of femtosecond laser inscribed lines and coating regions is fabricated for a mode conversion at the end of this chapter.

Finally, Chapter 7 summarizes the work in this thesis and the conclusions derived from this study.

## Chapter 2

# Polymer-coated Fibre Bragg Grating

### 2.1 Introduction

Fibre Bragg gratings are important components in modern telecommunication and optical sensor networks with their unique advantages such as immunity to electromagnetic interference, compact size, low cost, and the possibility of distributed measurement over a long distance [1]. FBGs have been utilized as sensor elements for monitoring many environmental parameters such as temperature, strain, pressure, displacement, and vacuum, as well as chemical sensors for detecting chemical species [2-10]. However the sensitivities and time responses of these FBG sensors have not been well understood. Bare FBGs without coating layer have been widely applied in on-line high-speed sensors for their high sensitivities in the shifts of the Bragg wavelengths on environmental axial strain and temperature. When the grating sections are recoated with different polymeric

materials, the sensitivity and response time of the sensors will be modified [11, 12]. The response times of these FBG sensors range from one nanosecond to several hours in different application fields [13]. On the other hand, in these applications, the measurand or the material to be measured needs to be known in advance because the cross sensitivity effects exist in the gratings as well as different responses of the gratings to different measurands. In most cases, the material system to be investigated is not monocomponent, in which parameters unique to specific components need to be distinguished as well as different extents in the responses of different components to the same parameters. Only a few research groups have reported the measurement of three parameters [14-19]. These techniques utilized either complicated configurations (interferometry and WDM), or special materials and structures in the fibre cores (microcrystallines), or special grating fabrication techniques (femtosecond lasers) in order to distinguish specific measurands, which resulted in bulky sensor systems restricted for special applications. Realization of simultaneous multiparameter sensing by FBGs with technically easy accessible approaches persists to be a challenge with significant merits of high integration, versatility, and low cost.

Deflection sensors with merits of flexibility, light-weighted, and versatility are highly demanded in many practical applications. Fibre deflection sensors reported so far can be classified into three categories: (1) Fibre-optic sensors on standard single-mode optical fibres use the translucent protective sheath that encases a fibre as a means of locating small displacement on an otherwise straight fibre [20]. It is also possible to determine the deflection magnitude by measuring the reduction in the fibre's core light. (2) The second

group consists of long-period gratings, which are based on the detection of the fibre-orientation dependences of the spectral responses of special eccentric core fibres or D-shaped fibres [21,22], multiple LPGs fabricated by different techniques [23], or fibres of cladding index modified by femtosecond lasers [24,25]. (3) The third group comprises fibre Bragg gratings in which the sensing processes were achieved by the intrinsic sensitivity of the D-type fibres to curvature [26], by the tight transverse confinement of an axially-offset FBG inscribed by an infrared femtosecond laser [27], or by combining a Mach-Zehnder interferometer with a cantilever-mounted FBG [28]. Among all reported sensors, direction-sensitive measurement has been achieved only on fibres with broken cylindrical symmetry in a few cases [21-24, 27] at the expense of high cost of the specialty fibres, expensive facilities to inscribe the fibre gratings, complicated processes for grating fabrication, multiple gratings in the sensor system, and dedicated interrogation techniques, which considerably reduce the practicality of these types of sensors [27]. In addition, details on the dynamics of fibre deflection have not been fully understood, especially information about the elongation of the grating or fibre and the *in situ* change in the optical properties.

Section 2.2 demonstrates the application of polyimide-coated fibre Bragg grating as a substance sensor and reveals the dependences of the sensitivity and time response on the coating thickness as well as factors influencing these properties. In section 2.3, an approach to achieve intelligent sensing of multiple environmental parameters with a single-fibre sensor system is demonstrated through the use of multiplexed fibre Bragg gratings with coatings of different polymers and specifications. An approach to realize

simultaneous measurement of magnitude and direction of deflection based on single FBG

inscribed on a standard single-mode optical fibre with possible temperature compensation is presented in section 2.4.

## **2.2 Tuning Sensing Response of Polymer-coated Fibre Bragg Grating**

In this section, we will demonstrate the application of polyimide-coated FBG as a substance sensor and reveal the dependences of the sensitivity and time response on the coating thickness as well as factors influencing these properties. Since the standard FBG fabrication technique needs to strip the protective plastic coating off the fibre before FBG inscription and recoat a polymeric layer afterwards to protect the grating, revelation of the coating-dependent properties is extremely important which provides additional possibility to discriminate different measurands by adopting different polymers and specifications without extra cost or complexity in the FBG fabrication. On the other hand, identification of the sensitivity and time response of the polymer-coated FBG is another crucial aspect for sensing applications. Our experiments indicated that the sensitivity and time response vary significantly with different coating materials. Even for the same coating material, different coating thicknesses can impact on the sensitivity and the response time of the measurement as well. Judging on either of the sensitivity or time response or both of these two parameters of a polyimide-coated FBG, it is possible to detect environmental

measurands and discriminate different substances.

The Bragg resonance wavelength  $\lambda_B$  of a FBG depends on the effective refractive index  $n_{\text{eff}}$  (or modal index, depending on both the wavelength and the guided propagation mode) of the fibre core and the grating periodicity  $\Lambda$  by the equation  $\lambda_B = 2n_{\text{eff}}\Lambda$ . The effective refractive index  $n_{\text{eff}}$  is sensitive to changes in temperature and strain because of thermo-optic effect (density and electronic polarizability change with temperature [29]) and photo-elastic effect (mechanical perturbation induced the Pockels coefficients change [30]). The grating periodicity  $\Lambda$  will also change due to the thermal expansion effect [31]. The shift in the Bragg wavelength due to changes in temperature,  $\Delta T$ , and changes in axial strain,  $\Delta\epsilon$ , which is the relative change in the length defined as  $\Delta l / l$ , can be described by [32, 33]

$$\Delta\lambda = \Delta\lambda_{B,T} + \Delta\lambda_{B,S} = \lambda_B(\alpha + \zeta)\Delta T + \lambda_B(1 - \hat{P}_e)\Delta\epsilon \quad (2-1)$$

where  $\alpha$  is the thermal expansion coefficient of the fibre and the parameter  $\zeta$  represents the thermo-optic coefficient,  $\hat{P}_e$  is an effective photoelastic constant.

Four FBGs of 1 cm each in the grating length were inscribed on hydrogen-loaded standard telecommunication single-mode optical fibres (Corning SMF-28) using a KrF excimer laser and a phase mask which is a high-spatial-frequency binary grating produced by holography and etched in fused silica. The excimer laser beam passing through the phase mask is diffracted to induce a refractive index modulation in the optical fibre core in contact with the corrugations of the phase mask. The polyimide from HD Microsystems [34] was then coated on the bare grating sections to obtain different

coating thicknesses by multiple dip coating processes at an appropriate withdraw rate of the fibre. The fibre was treated in an oven at 150°C for 5 minutes after each dip coating cycle and was finally cured in an oven at 200°C for one hour to imidize and harden the coating. From an optical microscopy, the thickness of the polyimide-coated optical fibre was observed and compared with the standard SMF-28 optical fibre with a cladding diameter of 125  $\mu\text{m}$ . The thicknesses of the polymeric coating layers of the four different FBGs were 11  $\mu\text{m}$  (FBG-A), 17  $\mu\text{m}$  (FBG-B), 20  $\mu\text{m}$  (FBG-C), and 24  $\mu\text{m}$  (FBG-D), respectively.

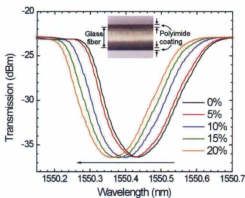


Figure 2-1: Transmission spectra of the polyimide-coated FBG-D with a coating thickness of 24  $\mu\text{m}$  at different degrees of salinity at 20°C. The inset is an image of the fibre with dip-coated polyimide coating.

The inset of Fig. 2-1 illustrates the polyimide-coated FBG-D used in this study. The transmission spectrum of the FBG was measured by a broadband light source (EBS-7210, MPB Communications) and an optical spectrum analyzer (OSA, Ando AQ6315E) with a

measurement resolution of 0.05 nm and accuracy of 0.05 nm. Figure 2-1 shows the transmission spectra of the FBG-D at different degrees of salinity with an initial Bragg resonance wavelength of 1550.436 nm and a reflection signal of 13.53 dB in water at a temperature of 20°C. When the salinity was changed from 0 to 20% at the same temperature, the Bragg wavelength exhibited a blue-shift and the shift in the Bragg wavelength of the polyimide-coated FBG as a function of salinity indicated a sensitivity of 3.70 pm/%. Swelling of the polyimide coating was mainly due to its water sorption property and was further attributed to the water molecules bound to the polymer chains and not the free water molecules [35]. When the polyimide-coated FBG was first immersed in the water bath, the bound water to the polymer chains and the free water in the space between the polymer chains were in a saturated equilibrium state. As the salinity of the solution increased, water egressed out of the polyimide material and the volume of the coating layer shrunk. No apparent change in the fibre coating thickness was found during the water diffusion process and thus the blue-shifted Bragg wavelength induced by an axial shortening  $\Delta l$  of the fibre coating could be described by Eqn. (2-1). As shown in Fig. 2-2, similar measurements on the dependences of the shifts in the Bragg wavelengths of the other three FBGs on the salinity were performed at 20°C with the salinity sensitivities of 1.45 pm/% (FBG-A), 2.45 pm/% (FBG-B), and 2.95 pm/% (FBG-C), respectively. The inset of Fig. 2 shows a linear dependence of the salinity sensitivity on the coating thickness with a coefficient of  $1.72 \times 10^{-1}$  pm%/μm. Since the degrees of polymer chain orientations slightly increase as the film thickness decreases [36], the FBG with a thicker polyimide coating possesses lower modulus and lower

strength properties, and thus a higher salinity sensitivity. Figure 2-2 clearly indicates that the salinity sensitivity of the polyimide-coated FBG is strongly dependent on the coating thickness with a higher sensitivity for a thicker coating.

In some specific cases the response time or the diffusion time of the polymer-coated FBG should be evaluated in order to identify a coating thickness with suitable sensitivity and time response. Firstly the polyimide-coated FBG is placed in the water bath where the environmental medium is water of a constant concentration source.  $C_{ext}$  is defined as the constant water concentration outside the fibre coating which equals 1. Then water will consequently diffuse into the fibre coating until a saturated equilibrium state is reached. Given a sufficient water diffusion time ( $t \rightarrow \infty$ ), the initial water concentration inside the fibre coating  $c_i$  will be equal to  $C_{ext}$  from the following equation:

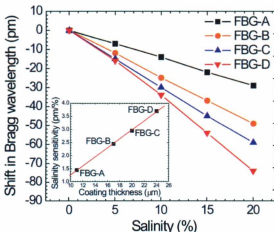


Figure 2-2: Dependences of the shifts in the Bragg wavelengths of the polyimide-coated FBGs on salinity. The polyimide coating thicknesses for FBG-A, -B, -C, and -D are 11, 17, 20, and 24  $\mu\text{m}$ , respectively. Inset shows the dependence of the salinity sensitivity on coating thickness.

$$c_i(r, t) = C_{\text{ext}} \operatorname{erfc}\left(\frac{r}{\sqrt{4Dt}}\right), \quad (2-2)$$

where  $D$  is the diffusion coefficient of the water,  $t$  is the diffusion time, and  $r$  is the radial distance from the center of the fibre.

When salinity of the environmental medium is increased, the water concentration in the fibre coating will be higher than that in the environmental medium and the water will egress into the environmental medium from the fibre coating until an equilibrium state is reached. The final water concentration inside the fibre coating  $c_f$  can be expressed as

$$c_f(r, t) = C_{\text{ext}} \operatorname{erf}\left(\frac{r}{\sqrt{4Dt}}\right). \quad (2-3)$$

During the process of adding salt into the water bath, the change in the water concentration in the polyimide coating is expressed by

$$\Delta c = c_i - c_f = 1 - C_{\text{ext}} \operatorname{erf}\left(\frac{r}{\sqrt{4Dt}}\right), \quad (2-4)$$

and  $\Delta c = 0$ , when  $t = 0$ .

Based on the facts that the external salinity change results in a longitudinal expansion of the coated fibre only and the shift in the Bragg wavelength is proportional to the axial strain, the normalized blue-shift in the Bragg wavelength is proportional to the change in the water concentration in the coating material. Therefore, we obtain the relation between the normalized shift in the Bragg wavelength and the salinity,

$$\Delta\lambda = \lambda_{\text{salt}, t} - \lambda_{\text{water}, 0} = \gamma \Delta c = \gamma \left[ 1 - C_{\text{ext}} \operatorname{erf}\left(\frac{r}{\sqrt{4Dt}}\right) \right], \quad (2-5)$$

or

$$\lambda_{\text{salt},t} = \lambda_{\text{water},0} + \gamma \left[ 1 - (1-S) \operatorname{erf} \left( \frac{r}{\sqrt{4Dt}} \right) \right], \quad (2-6)$$

where  $S$  is the salinity of the environmental medium and  $\gamma$  is a proportionality coefficient.  $\lambda_{i,t}$  stands for the Bragg wavelength of the fibre in either saline solution ( $i = \text{salt}$ ) or water solution ( $i = \text{water}$ ) at time  $t$ . Obviously,  $\lambda_{\text{salt},0} = \lambda_{\text{water},0}$  when  $t = 0$ .

The normalization of the Bragg wavelength defines  $\lambda_{\text{water},0} = 0$  and  $\lambda_{\text{salt},t \rightarrow \infty} = 1$ . It is easy to find out that  $\gamma = 1$  when  $t \rightarrow \infty$ . Therefore,

$$\lambda_{\text{salt},t} = \lambda_{\text{water},0} + \left[ 1 - (1-S) \operatorname{erf} \left( \frac{r}{\sqrt{4Dt}} \right) \right]. \quad (2-7)$$

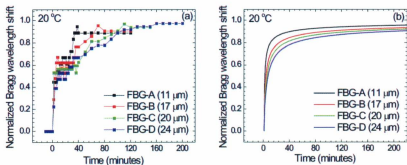


Figure 2-3: Time-dependent evolutions of the normalized shifts in the Bragg wavelengths of the four polyimide-coated FBGs after transferred from an environmental salinity of 0 to 20% in solution: (a) experimental results, and (b) simulation.

Due to the limitations of the measurement apparatus (i.e. resolution of the optical spectrum analyzer) and finite measurement time in practical applications, the value of  $\gamma$  deviates from 1. Figure 2-3(a) shows the experimentally observed time-dependent evolutions of the normalized Bragg wavelengths of the polyimide-coated gratings with

different coating thicknesses transferred from an environmental salinity of 0 to 20% in solution. For the FBG-A, -B, -C, and -D, the diffusion times observed from the times needed for the transmission spectra of the gratings to be stabilized were 38, 70, 110, and 160 minutes, respectively. By using Eqn. (2-6) and the diffusion coefficient  $D$  of  $10^{-12}$  m<sup>2</sup>/s [37], the values of  $\gamma$  corresponding to FBG-A, -B, -C, and -D can be calculated to be 1.06, 1.08, 1.10, and 1.11, respectively. This increasing proportionality coefficient  $\gamma$  indicates that the same change in the environmental salinity induces a larger blue-shift of the Bragg wavelength for a FBG with a thicker polyimide coating. Figure 2-3(b) depicts simulated time-dependent evolutions of the normalized shifts in the Bragg wavelengths of the four polyimide-coated FBGs, calculated with Eqn. (2-5) or (2-6). Both the experimental results and analysis demonstrate that the grating with a thicker polyimide coating has a longer response time and a higher sensitivity.

## 2.3 Multiparameter Sensing with Polymer-coated Fibre Bragg Grating

In this section, intelligent sensing of multiple environmental parameters with FBGs of different polymer coatings and specifications is achieved. As a demonstration of this approach, simultaneous measurement of saccharinity, salinity, and temperature will be accomplished with a single-fibre sensor system, in which two FBGs are coated with polyimide layers of different thicknesses and the other one is coated with an acrylate layer.

Since the standard FBG fabrication technique needs to strip the protective plastic coating off the fibre before grating inscription and recoat a polymeric layer afterwards to protect the grating, the coating of FBGs with different polymeric materials proposed here does not complicate the procedures or add extra cost in the FBG fabrication, which can be easily achieved by fibre recoaters or dip coating technique. Furthermore, without additional optical devices or spectroscopic techniques as used in the reported literatures, this approach realizes one-fibre solution for versatile applications of the FBGs rather than single specialized use.

The technique of using a polyimide-coated FBG to detect salinity can be generalized to detect other analytes (for example, saccharinity) in solution. However, in case several substances coexist in the solution, it becomes indiscernible if only the change in the Bragg wavelength is monitored. In order to distinguish these different substances, FBGs with different polyimide coating thicknesses are employed here.

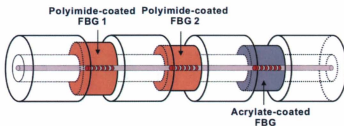


Figure 2-4: Illustration of multiplexed FBGs coated with different polymers.

As shown in Fig. 2-4, three FBGs of 1 cm each in the grating length were inscribed on a standard telecommunication single-mode optical fibre (Corning SMF-28) followed by coating of acrylate and polyimide on the grating sections by the use of Vytran fibre

recoaters PTR-200 and dip coating, respectively. The acrylate and polyimide materials used for coating were DSM950-200 (Fibre Optic Center™, Inc.) [38], and PI2525 from HD MicroSystems L.L.C. [39], respectively. The polyimide coatings were prepared by dip coating with a translation stage (ATS100) through a motion controller (U511, Aerotech, Inc.). Polyimide layers of different thicknesses can be obtained by multiple dip coating processes at an appropriate withdraw rate of the fibre. The fibre was treated in an oven at 150°C for 5 minutes after each dip coating cycle and was finally cured in an oven at 200°C for one hour to imidize and harden the coating. The thicknesses of the polymeric coating layers in this study were 25 and 20 µm for the two polyimide-coated gratings, and 20 µm for the acrylate-coated one.

Figure 2-5(a) shows the transmission spectrum of the polyimide-coated FBG1 with a coating thickness of 25 µm at different saccharinities with an initial Bragg resonance of 1551.488 nm and a reflection signal of 8.18 dB in water. If the saccharinity of the solution is changed without the presence of salinity at 20°C, the Bragg wavelength will blueshift and the Bragg wavelength of the polyimide-coated FBG as a function of saccharinity is shown in the inset of Fig. 2-5(a), which indicates a saccharinity sensitivity  $\Delta S_{ac}$  of  $-1.10 \times 10^{-3}$  nm/%. Figure 2-5(b) shows the dependence of the shift in the Bragg wavelength on the saccharinity and salinity where both of the two parameters are varied independently. The salinity sensitivity  $\Delta S_{ac}$  of the polyimide-coated FBG1 is calculated to be  $-3.80 \times 10^{-3}$  nm/%. The figure clearly indicates that any change in either saccharinity or salinity, or the combination of them will result in the blueshift of the Bragg wavelength, however, it is impossible to distinguish the contribution from each factor using the single

polyimide-coated FBG. A similar measurement on the dependence of the shift in the Bragg wavelength on the saccharinity and salinity was performed on a polyimide-coated FBG2 with a polyimide thickness of 20  $\mu\text{m}$  at 20°C, as shown in Fig. 2-6.

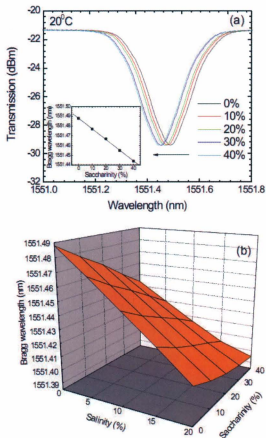


Figure 2-5: Polyimide-coated FBG for simultaneous saccharinity and salinity measurement (coating thickness 25  $\mu\text{m}$ ): (a) transmission spectra at different saccharinities with the inset on the Bragg wavelength as a function of saccharinity, and (b) shifts in the Bragg wavelength in response to the independent changes in saccharinity and salinity.

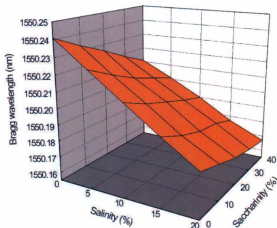


Figure 2-6: Polyimide-coated FBG for simultaneous saccharinity and salinity measurement (coating thickness 20  $\mu\text{m}$ ) with shifts in the Bragg wavelength in response to the independent changes in saccharinity and salinity.

The saccharinity and salinity sensitivities of this FBG are  $-0.73 \times 10^{-3}$  and  $-2.95 \times 10^{-3}$  nm/%, respectively. Figure 2-7 shows the Bragg wavelength shifts of the three FBGs (redshifted) as a function of temperature and the inset gives the transmission spectra of the acrylate-coated FBG at different temperatures. The temperature sensitivities  $\Delta T$  of the acrylate-coated FBG and the polyimide-coated FBG1 and FBG2 in water were found to be  $1.10 \times 10^{-2}$ ,  $1.04 \times 10^{-2}$ , and  $1.01 \times 10^{-2}$  nm/ $^{\circ}\text{C}$ , respectively. The sensing responses of these FBGs have been observed to be reversible and the reset of the responses can be realized by placing the gratings in de-ionized water. The different responses of these acrylate- and polyimide-coated FBGs lie in the differences in the thermo-optic and elasto-optic performances of their coatings.

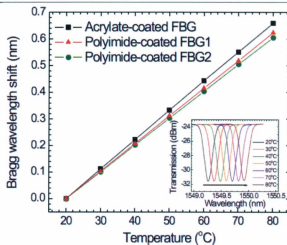


Figure 2-7: Dependences of the shifts in the Bragg wavelengths of the acrylate- and polyimide-coated FBGs on temperature. The inset shows the redshifting transmission spectra of the acrylate-coated FBG with increasing temperature.

The experiment of simultaneous measurement of saccharinity, salinity and temperature indicates that not only the different polymeric coating materials will affect the FBG sensing performance, but for the same polymeric coating material, different thicknesses of the coating will modify the grating sensitivities of the environmental parameters as well. The shifts in the Bragg resonance wavelengths of the FBGs discussed here can be expressed as

$$\begin{bmatrix} \Delta\lambda_{\text{acrylate}} \\ \Delta\lambda_{\text{polyimide1}} \\ \Delta\lambda_{\text{polyimide2}} \end{bmatrix} = \begin{bmatrix} 1.10 \times 10^{-2} & 0 & 0 \\ 1.04 \times 10^{-2} & -1.10 \times 10^{-2} & -3.80 \times 10^{-2} \\ 1.01 \times 10^{-2} & -0.73 \times 10^{-2} & -2.95 \times 10^{-2} \end{bmatrix} \begin{bmatrix} \Delta T \\ \Delta S_{\text{ac}} \\ \Delta S_{\text{cl}} \end{bmatrix} = M_{TSS} \begin{bmatrix} \Delta T \\ \Delta S_{\text{ac}} \\ \Delta S_{\text{cl}} \end{bmatrix}, \quad (2-8)$$

which is equivalent to the following equation through a matrix transposition:

$$\begin{bmatrix} \Delta T \\ \Delta S_{ac} \\ \Delta S_{al} \end{bmatrix} = M_{TSS}^{-1} \begin{bmatrix} \Delta \lambda_{acrylate} \\ \Delta \lambda_{polyimide1} \\ \Delta \lambda_{polyimide2} \end{bmatrix}. \quad (2-9)$$

In this case, a character matrix  $M_{TSS}$  can be used to determine the absolute values of the saccharinity, salinity and temperature from the shifts of the Bragg wavelengths of the three gratings. When this approach is extended to a general case of distinguishing multiple measurands, the character matrix  $M$  for quantifying multiparameters becomes:

$$\begin{bmatrix} \Delta P_1 \\ \Delta P_2 \\ \vdots \\ \Delta P_n \end{bmatrix} = \begin{bmatrix} M_{11} & M_{12} & \cdots & M_{1n} \\ M_{21} & M_{22} & \cdots & M_{2n} \\ \vdots & \vdots & \vdots & \vdots \\ M_{n1} & M_{n2} & \cdots & M_{nn} \end{bmatrix} \begin{bmatrix} \Delta \lambda_1 \\ \Delta \lambda_2 \\ \vdots \\ \Delta \lambda_n \end{bmatrix} = M^{-1} \begin{bmatrix} \Delta \lambda_1 \\ \Delta \lambda_2 \\ \vdots \\ \Delta \lambda_n \end{bmatrix}, \quad (2-10)$$

in which  $P_1, P_2, \dots,$  and  $P_n$  stand for multiple parameters to be measured, such as strain, temperature, force, or pressure, and  $\Delta \lambda_1, \Delta \lambda_2, \dots,$  and  $\Delta \lambda_n$  correspond to the shifts in the Bragg wavelengths of multiple FBGs with different polymeric coatings and thicknesses. Once the sensor system is calibrated, the operation of the sensor does not require prior knowledge of the measurands to be measured, an intelligent sensing is achieved. The current optical fibre salinity/saccharinity sensor works on very general principles, i.e., the solutes control how much water is absorbed by the polyimide coating. Alternative sensor configurations will be further explored to make very specific sensors by recoating the fibre Bragg gratings with other functional polymer coating materials, i.e., hydrogels.

## 2.4 Deflection Measurement with Fibre Bragg Grating

### Cantilever Sensor

In this section, we present an approach to realize simultaneous measurement of magnitude and direction of deflection based on single FBG inscribed on a standard single-mode optical fibre with possible temperature compensation. The spatial-resolved dynamics of fibre deflection and the simultaneous changes in the optical properties will be revealed by optical low-coherence reflectometry (OLCR). The sensing signal is the light coupled into the fibre from an external light source, which changes its optical properties when propagating in the deflected fibre as well as passing through the grating. The set point, i.e., Bragg resonance wavelength, triggering time, responsivity, and dynamic range of the sensor system can be adjusted in order to satisfy the requirements of specific applications. The selection of the cantilever material with different mechanical properties provides an additional capability to change the set point of the sensor. Furthermore, the cantilever serves as a good protection for the fibre in practical applications. In the following sections, we will discuss the design and performance of our sensor system as well as comparisons with theoretical analysis and other reported bending or deflection measurement methods.

A FBG with a grating length of  $\sim 1$  cm was recoated with acrylate polymer to a diameter of  $190 \mu\text{m}$  at the bare fibre grating section. The transmission spectrum of the FBG at  $20^\circ\text{C}$  was measured by the optical spectrum analyzer with a reflection signal of 9.24 dB at a Bragg wavelength of 1549.020 nm. Two ends of the CPC<sup>®</sup> (trademark of

Corning Inc.) coated fibre with the grating section at the center were mounted on a spring steel cantilever (ASTM A228) using epoxy glue, as shown in Fig. 2-8.

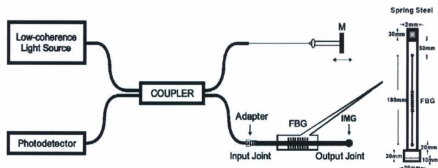


Figure 2-8: Schematic illustration of optical low-coherence reflectometry measurement of the FBG cantilever sensor.

When an optical fibre with a Bragg grating section is mounted to a steel substrate to form a cantilever, as shown in Fig. 2-9(a), the Bragg resonance wavelength of the FBG will redshift or blueshift when the cantilever experiences a convex or concave deflection. The relationship between the change in the length of the fibre  $\Delta l$  and the deflection  $D$  is

$$\Delta l = \frac{2d}{L} \arctan\left(\frac{D}{L}\right), \quad (2-11)$$

where  $d$  is the neutral axis distance between the optical fibre and the cantilever, and  $L$  is the initial effective length of the cantilever. The shift of the Bragg resonance wavelength  $\Delta\lambda_B$  induced by the deflection is

$$\Delta\lambda_B = \frac{2d(1-\bar{P}_e)}{L} \arctan(D/L) \quad (2-12)$$

where  $\bar{P}_e$  is an effective strain optic constant.

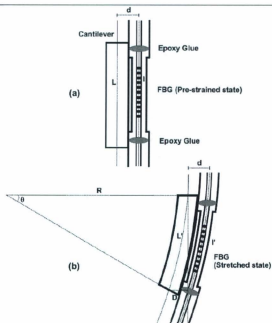


Figure 2-9: Illustration of a FBG cantilever sensor in (a) pre-strained state and (b) stretched state.

Figure 2-9(b) shows a schematic illustration of the fibre elongation due to a convex deflection of the cantilever. Figure 2-10 simulates the Bragg wavelength as a function of the ratio of the deflection to the effective length following Eqn. (2-12). Three segments can be identified on the curve, which are labeled as I, II, and III. The segment I exhibits a linear behavior when the FBG is stretched or compressed away from the pre-strained position within the proportionality limit. In segment III when the deflection goes beyond the limit, the Bragg wavelength approaches an extreme. The segment II is a transition region where the slope of the Bragg wavelength versus deflection/effective length decreases as it moves away from the proportionality region. When the FBG is attached on

the cantilever, an optimal pre-strain value has to be chosen in order to satisfy the requirements of different deflection measurement. For a small deflection, a low pre-strained value is appropriate, however, an extremely low set point will result in a nonlinear and nonsymmetrical performance of the sensor in the convex and concave deflection because the Bragg wavelength falls into the segment II or even III due to a complete relaxation of the fibre. On the other hand, for a large deflection, a high pre-strained value is suitable as long as it will not cause break of the FBG or relative movement between the coating and the cladding of the fibre. The set point of the pre-strained value for the FBG cantilever used in this study was  $100 \mu\epsilon$ , which was carefully selected to ensure that no break or relative movement between the fibre cladding and its polymeric coating take place in the measurement.

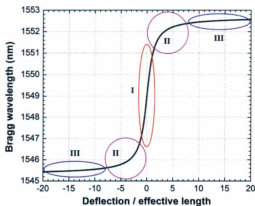


Figure 2-10: Simulation of the Bragg resonance wavelength as a function of the ratio of the deflection to the effective length.

OLCR is an interferometric technique to evaluate the structural and optical properties of materials and devices with a high spatial resolution, high reflection sensitivity, and a large dynamical range [40-42]. A high-resolution reflectometer (Ando AQ7410B) with a sampling resolution of 2  $\mu\text{m}$  and a spatial resolution of 20  $\mu\text{m}$  was utilized to analyze the internal structure of the cantilever sensor in this study. As shown in the illustration of the OLCR measurement system (Fig. 2-8), a low-coherence LED light source (AQ7413, Yokogawa Electric Corp.) with peak wavelength at 1.55  $\mu\text{m}$  is launched into a fibre coupler and divided into two light paths in which part of light propagates into a test arm with the FBG while the other part is introduced to a reference arm where the optical delay is varied by the movement of a reference mirror. In the test arm, the light passes through a fibre adapter, the FBG, and to the cleaved fibre end immersed in an index-matching gel (IMG, Norland index matching liquid 150) where it is back reflected. The reflection from the FBG is recombined with the signal from the reference arm and received by the InGaAs photodetector (AQ7410, Yokogawa Electric Corp.). When the two optical path lengths are within the coherence length,  $L_C = \lambda^2/n\Delta\lambda$ , where  $n$  is the refractive index of the fibre core,  $\lambda$  and  $\Delta\lambda$  are the center wavelength and the spectrum bandwidth of the light source, respectively, the envelope of the interference signal can be detected. The location of the reflection can be obtained by precisely scanning the position of the moving mirror, while the reflectivity is measured by the intensity of the interference signal [43],

$$I(\tau) = R \left| \int_{-\infty}^{\infty} S(\omega) I(\omega) e^{j\omega\tau} d\omega \right|, \quad (2-13)$$

where  $R$  is the responsivity of the photodetector,  $S(\omega)$  is the source spectral density,  $I(\omega)$  is the frequency-dependent reflectivity, and  $\tau$  is the time difference between the two arms.

Figure 2-11 plots the backscattered interferogram from the cantilever sensor as a function of fibre geometric length. A reflection peak of the Bragg grating appears between the peaks corresponding to the lights reflected from the two ends of the fibre, i.e., the input air/fibre joint and the output fibre/IMG joint. A close-up of the three specific interferograms shown in Fig. 2-12 indicates that the corresponding peak reflectance/fibre geometric length are -14.65 dB/4.344 mm, -32.83 dB/848.25 mm, and -42.36 dB/508.024 mm, respectively. Several small peaks appear behind the strong grating (reflection 90%) region due to the strong multiple reflections [44]. Using OLCR method to measure deflection with the cantilever sensor requires simultaneous monitoring of the reflected lights from the two ends of the fibre. The reflection signals at these points are expected to be strong enough in order to obtain exact locations of the joints. In this study, the reflection at the input air/fibre joint through a fibre connector is -14.65 dB, which is of suitable signal level to be distinguished from those at the FBG and the output joint. In other applications where the reflection at the input joint needs to be eliminated, fibre splicing may be adopted. Since the refractive index of the IMG is 1.52 (at 589 nm), which is slightly different from the corresponding value of 1.4682 (at 1550 nm) for the fibre core, the back-reflection carries a signal of -32.83 dB, which is ideal for the application here to give a suitable signal level different from those reflections at the input air/fibre joint or at grating section. In the case no IMG is used, the reflection from the output joint will be overwhelmingly greater than those from other locations, leading to the difficulty in identification. In addition, the IMG can be used as an indication whether the fibre is intact or connected well during the experiment.

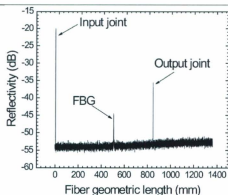


Figure 2-11: Low-coherence interferogram of the FBG used in this study. FBG is located between the air/fibre input facet and the fibre/IMG output facet.

When the FBG sensor system was placed in a temperature-controlled room with the temperature maintained at  $20.0 \pm 1.0$  °C throughout the experiment, the top end of the cantilever was anchored onto a vertical frame and the bottom was contacted by a motor-driven linear stage (ATS100, Aerotech Inc.) with a motion accuracy of  $0.5 \mu\text{m}$  and a repeatability of  $0.3 \mu\text{m}$ . The deflection effect was generated by the translation stage controlled by a computer through a general-purpose interface bus (GPIB) interface system and LabVIEW™ programming control. The translation stage moved forward from either side of the cantilever to change the deflection direction. When the translation stage moved from the side of the cantilever with the FBG, a convex deflection was induced on the cantilever and hence the FBG stayed in a stretched state. On the other hand, when the translation stage moved from the opposite side of the cantilever, the FBG experienced a concave deflection and stayed in a compressed state.

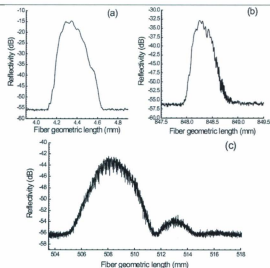


Figure 2-12: Interferogram close-up: (a) input air/fibre joint, (b) output fibre/IMG joint, and (c) FBG

Since the two ends of the fibre with the grating section at the center were attached to the cantilever, the increase in the fibre output joint position corresponding to the elongation of the whole fibre was due to the deflection induced extension of fibre section between the two fixed points. For the FBG cantilever sensor, the thickness of the cantilever and the CPC<sup>®</sup> coating diameter of the optical fibre were both 250  $\mu\text{m}$ . Thus the neutral axis distance between the cantilever and the optical fibre was 250  $\mu\text{m}$ . As illustrated in Fig. 2-8, the top section (30 mm) of the cantilever was fixed and the bottom section (10 mm) was pushed by the translation stage. The initial effective length of the cantilever  $L$  was 270 mm with an initial fibre attaching length  $l$  of 180 mm. When the translation stage, which was located at the same side of the fibre with regard to the

cantilever, moved forward 100 mm with a step of 20 mm, the FBG experienced a convex deflection. An increase in the fibre length of 0.118 mm was observed. When the translation stage moved backward 20 mm with a step of 5 mm, the FBG experienced a concave deflection and a decrease in the fibre length of 0.025 mm was observed. In the case when the translation stage is moved backward further, the fibre departs from the cantilever surface and no further change in the fibre output point position is observed due to the complete relaxation of the fibre. The fibre output joint position, which indicates the change in the fibre length as a function of the deflection, is shown in Fig. 2-13. The simulation obtained by using Eqn. (2-11) exhibits good agreement with the experimental result. Figure 2-13 indicates that monitoring the change in the length of the cantilever-supported fibre can distinguish both the magnitude and the direction of deflection by OLCR measurement.

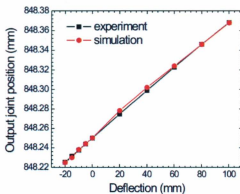


Figure 2-13: Dependence of the fibre output joint position on the deflection measured by optical low-coherence reflectometry. The shift in the fibre output joint position indicates the elongation of the fibre during deflection.

If the environmental temperature is stable, it is possible to carry out the deflection measurement by OLCR without the FBG. However, if the temperature variation can not be negligible, it will be necessary to have a FBG integrated in the cantilever sensor in order to achieve temperature compensation. The Bragg wavelength of the FBG as a function of temperature is shown in Fig. 2-14(a). The shift in the Bragg resonance wavelength of the grating due to a temperature fluctuation  $\Delta T$  can be expressed as  $\Delta\lambda_{B,T} = K_{T,FBG}\Delta T$ , where  $K_{T,FBG}$  is the temperature coefficient of the FBG, measured to be 0.00975 nm/°C. Figure 2-14(b) gives the experimental and simulated results on the dependence of the Bragg wavelength of the FBG cantilever sensor on deflection in both the convex and concave cases. At 20 °C a red-shift in the FBG resonance peak wavelength over the convex deflection up to 90 mm was found to be 0.716 nm, which is close to the simulation value of 0.727 nm following Eqn. (2-12). Operating in the linear segment I, the shift in the Bragg resonance wavelength of the grating due to a convex deflection  $D$  can be expressed as  $\Delta\lambda_{B,+D} = K_{+D,FBG}\Delta D$ , where  $K_{+D,FBG}$  is the convex deflection coefficient of the FBG, measured to be 0.00796 nm/mm. Similarly, a blue-shift in the FBG resonance peak wavelength over the concave deflection up to 11 mm was 0.097 nm, which is close to the simulation value of 0.100 nm. The concave deflection coefficient of the FBG,  $K_{-D,FBG}$ , is measured to be 0.00882 nm/mm.

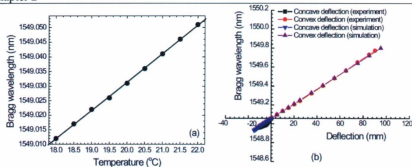


Figure 2-14: Dependence of the Bragg resonance wavelength of the cantilever-supported FBG on: (a) temperature around 20 °C, and (b) convex and concave deflections, respectively.

Thus the change in the length of the cantilever  $\Delta L$  and the Bragg wavelength shift can be expressed as

$$\begin{bmatrix} \Delta L \\ \Delta \lambda_{\text{FBG}} \end{bmatrix} = \begin{bmatrix} K_{T,\Delta L-\text{fib}} & K_{D,\Delta L-\text{fib}} \\ K_{T,\text{FBG}} & K_{D,\text{FBG}} \end{bmatrix} \begin{bmatrix} \Delta T \\ D \end{bmatrix}. \quad (2-14)$$

Simultaneous measurement of length change of the fibre and Bragg wavelength shift of FBG will provide a dynamic temperature compensation mechanism.

The use of a FBG in a cantilever configuration provides a capability to change the performance of the sensor system in addition to the obvious benefit of protection to the fibre. The neutral axis distance between the optical fibre and the cantilever is an important factor affecting the deflection sensitivity. The simulation of the dependence of the Bragg wavelength on the deflection under different neutral axis distances obtained by using Eqn. (2-12) is shown in Fig. 2-15. The simulated shifts in the Bragg wavelength with the same 150 mm deflection for three neutral axis distances of 250  $\mu\text{m}$ , 1 mm, and 4 mm are 1.197, 4.787, and 23.935 nm, respectively. It is obvious that the Bragg

wavelength of the FBG attached on the cantilever with a larger neutral axis distance will

have a larger shift when the FBG sensor experiences the same deflection.

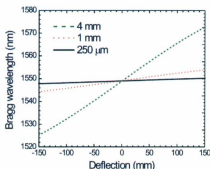


Figure 2-15: Simulation of the Bragg resonance wavelength as a function of deflection at different neutral axis distances of 250  $\mu\text{m}$ , 1 mm, and 4 mm, respectively.

For the steel cantilever, the deflection due to an external impaction force is [45],

$$D = \frac{F \cdot L^3}{3E \cdot I}, \quad (2-15)$$

where  $F$  is the force acting on the end of the cantilever,  $L$  is the length of the cantilever,  $E$  is the Young's modulus of the steel, and  $I$  is the area moment of the inertia for the cantilever. With the same force acting on the cantilever, the smaller the cantilever width, the larger the deflection will be. Therefore, the cantilever sensor with a large cantilever width is suited for measuring a small deflection and vice versa. The availability of different cantilever materials with various mechanical properties provides an ample opportunity to design a sensor system satisfying specific requirements of applications.

In many applications of utilizing optical fibres to monitor bending, bending information must be indirectly recovered through proper determination of strain and

subsequently transduction to bending. LPGs were found to possess better bend sensitivities than the FBGs. However, LPGs are very sensitive to temperature, unable to operate on reflection, impossible for localized measurements, and difficult for embedding in composite materials [26]. In addition, their interrogation and multiplexing is not straightforward, which limits their practical applications. Even if the LPG sensor achieves simultaneous measurement of the magnitude and direction of a bend, a measurement independent of temperature and strain can only be achieved in the case that the LPGs are replaced by FBGs, when the cross-sensitivity between bend and temperature, or bend and strain, is resolved [23]. A comparison of the OLCR method and the Bragg wavelength monitoring method developed in this study with other recently reported bending/deflection measurement techniques is listed in Table 2-1, which indicates advantages of the OLCR method including direct deflection measurement, highest spatial accuracy, possible temperature compensation, possibility of quasi-distributed measurement, low cost, and achievable with standard single-mode telecommunication fibre. The OLCR method realizes real-time spatial-resolved monitoring of deflection dynamics through direct deflection measurement, which is ideal for applications requesting highest spatial resolution or measurement in reflection mode. The OLCR method developed in this study does not possess vector-sensing capability to monitor fibre orientation, which could be achieved by the addition of fibre gratings or improvement in the interrogation system.

OLCR has been utilized to study the spatial-resolved dynamics of deflection with a FBG cantilever sensor and proved to be an effective technique in revealing the internal

structure of the sensing fibre as well as realizing *in situ* deflection measurement for both magnitude and direction simultaneously. The interferograms of the OLCR measurement indicate the peak reflectance and fibre geometric length during the dynamic deflection measurement. An increase in the fibre length of 0.118 mm and a decrease of 0.025 mm were observed for the convex and concave deflection of the cantilever sensor with deflections of 100 and 20 mm, respectively. In addition to the deflection measurement achieved by the OLCR method, Bragg wavelength monitoring method has been demonstrated to be an alternative approach to realize simultaneous measurement of the magnitude and direction of deflection. From the transmission spectrum measurement of the FBG, a temperature compensation mechanism is realized. The adoption of a FBG in a cantilever configuration provides an additional capability to change the performance of the sensor system in addition to the obvious benefit of protection to the fibre. The experimental results have a good agreement with the theoretical analysis. Some important aspects to designing a suitable FBG cantilever sensor for different applications have been discussed, which include selection of pre-strain set point, effects of the mechanical properties of the cantilever. For the study here, the FBG is needed because the selection of pre-strain set point and effects of the mechanical properties of the cantilever to be discussed in the following sections have been investigated with the existence of a FBG. Also, the FBG is needed in order to make a comparison with the results obtained from the Bragg wavelength monitoring method. In addition, the analysis of spatial-resolved dynamics and changes in the optical properties of the FBG provide a possibility of quasi-distributed point deflection monitoring.

Table 2-1 Comparison of OLCR method and Bragg wavelength monitoring method developed in this study with other recently reported bending/deflection measurement techniques.

Parameter	LPG sensor in SMF [23]	D-shaped LPG sensor [22]	D-type FBG sensor [26]	Cantilever-mounted FBG sensor [28]	OLCR deflection sensor (this study)
Fibre	Corning SMF-28	D-shaped fibre	D-type fibre	SMF	Corning SMF-28
Sensing element	3 LPGs	2 LPGs	2 FBGs	1 FBG	1 FBG
Sensing mechanism	Shifts in the resonance wavelengths of LPGs	Shifts in the resonance wavelengths of D-shaped LPGs	Shifts in the resonance wavelengths of D-type FBGs	Shifts in the FBG resonance wavelength	Rayleigh backscattering of reflected light
Sensitivity	Curvature sensitivity $5.2 \text{ nm m}^{-1}$	Curvature sensitivity $-2.5$ and $+2.85 \text{ nm m}^{-1}$	Curvature sensitivity depends on the value of the radius of curvature	Deflection sensitivities $0.135 \text{ nm mm}^{-1}$ (vertical), and $0.602$ or $-0.572 \text{ nm mm}^{-1}$ (horizontal)	Direct deflection measurement, sampling resolution $2 \text{ }\mu\text{m}$
Accuracy	—	$0.4 \text{ m}^a$	$730 \text{ }\mu\text{m Hz}^{-1/2}$ at measurement bandwidth of $1 \text{ Hz}$	$7.4 \text{ mm}$ (vertical); $1.7 \text{ mm}$ (horizontal) <sup>a</sup>	$20 \text{ }\mu\text{m}$
Temperature compensation	Impossible unless LPGs replaced by FBGs	—	Yes	Possible with one additional FBG	Yes
Detection limit	<ul style="list-style-type: none"> <li>• Multiple LPGs prepared by different techniques</li> <li>• Curvature and bending direction measured by different LPGs</li> </ul>	<ul style="list-style-type: none"> <li>• Different bending sensitivities at different bend orientations</li> <li>• Measurement at discrete fibre orientations</li> </ul>	<ul style="list-style-type: none"> <li>• Observed non-Gaussian profile in FBG spectral response due to the degradation</li> <li>• Without vector-sensing capability</li> </ul>	<ul style="list-style-type: none"> <li>• Complicated interrogation system</li> <li>• Without vector-sensing capability</li> </ul>	Without vector-sensing capability

<sup>a</sup> Calculated from information available in the reference.

— Data not available.

## **Chapter 3**

# **Bragg Grating Imprinted Polarization Maintaining Fibre Loop Mirror**

### **3.1 Introduction**

Precision and stable wavelength control is of great importance for telecommunication networks, test and measurement systems [1]. Examples include high-power wavelength stabilized semiconductor pump lasers in erbium doped fibre amplifiers and Raman fibre amplifiers [2], wavelength-division multiplexers (WDMs) [3], and multiwavelength fibre lasers [4, 5]. In many applications wavelength locking and spectral filtering are critical requirements. Several techniques have been reported to achieved wavelength locking, including the use of a Fabry-Perot etalon to lock the laser modes in an erbium fibre ring laser with increased insertion loss of the cavity [6], an unbalanced Mach-Zehnder interferometer driven by electronic signal with high probability of unexpected shift in the

laser wavelength due to environmental perturbation [7], and a fibre Bragg grating to lock the output from a semiconductor laser at single wavelength [2, 8]. In all these techniques, the polarization properties of the lasers are ignored. Recently, a fibre Sagnac loop mirror (SLM) incorporating polarization maintaining fibre (PMF) has attracted considerable attention as an optical comb filter due to its intrinsic merits such as low insertion loss, polarization independence to input light, broad useful spectral bandwidth and high resistance to environmental changes [4, 9-12]. In applications such as multi-wavelength fibre lasers, wavelength tunability is required, which is accomplished through a wavelength-selective comb filter. A wavelength-selective comb filter incorporating a fibre SLM shows significant advantages over other reported techniques with regard to the wavelength control capability. Most optical comb filters reported so far lack flexibility, except that some of them are tunable in the absolute position of the output or the channel space with the use of specialty fibres or complicated configurations [4, 9, 11]. The comb filter can be tuned by changing the operating temperature of the SLM using a pumped erbium-ytterbium co-doped PMF [4], high-birefringence elliptical core side-hole fibre [9], or additional active devices in the fibre loop mirror [13]. An SLM based on polarization maintaining photonic crystal fibre with reduced temperature sensitivity was also reported [10]. Fibre Sagnac interferometers or Sagnac loop mirrors have also received much attention for use in optical fibre sensing field. Recent work has reported the measurement of many single parameters, such as temperature [14, 15], strain [16, 17], bending [18], and liquid level [19]. Simultaneous measurement of temperature and strain based on a configuration using polarization maintaining fibre Sagnac interferometer are

realized [20-24]. Fibre Bragg grating sensor interrogation systems that use a polarization maintaining fibre Sagnac loop filters are investigated [25-27]. The fibre Bragg grating demodulation system is stable compared with other interference demodulators due to the low temperature sensitivity of the photonic crystal fibre or its high birefringence of the polarization maintaining fibre. In section 3.2, wavelength control by the use of fibre Bragg grating imprinted polarization maintaining fibre Sagnac loop mirror is realized through polarization and strain tuning. Section 3.3 presents an approach to achieve simultaneous wavelength locking and spectral filtering by the use of fibre Bragg grating embedded polarization maintaining fibre Sagnac loop mirror through temperature tuning. In section 3.4, we use a fibre Sagnac interferometer with an integrated polarization maintaining fibre Bragg grating to achieve simultaneous temperature and axial strain measurement. The fibre Sagnac interferometer sensor possesses the possibility to simultaneously measure multiple measurands by monitoring the changes in the fast axis and slow axis polarization maintaining fibre Bragg resonance wavelengths and multiple interference peak wavelengths of the fibre Sagnac interferometer.

### **3.2 Wavelength Control with Grating Imprinted Fibre Loop Mirror by Polarization and Strain Tuning**

In this section, a fibre Bragg grating imprinted polarization maintaining fibre Sagnac loop mirror is adopted to control transmission spectrum through polarization and strain tuning.

The operation principle to realize wavelength control with Bragg grating imprinted PMF is basically a SLM with the broadband light source (EBS-7210, MPB Communications) and detection of the interference signal using the optical spectrum analyzer (Ando AQ6315E). As shown in Fig. 3-1, broadband light is launched into a singlemode 50:50 fibre coupler and divided into two arms where beams propagate clockwise and counterclockwise. An SLM is formed when a polarization controller (HP 11896A) and a 10cm-FBG inscribed PMF (PANDA, Thorlabs) of 210 cm in length connect the two ends of the fibre coupler. The reflection spectrum of the FBG is detected by the OSA, which shows the fast-axis Bragg resonance wavelength at 1546.073 nm with a reflection of 3.20 dB and the slow-axis Bragg resonance wavelength at 1546.440 nm with a reflection of 4.59 dB (Fig. 3-2).

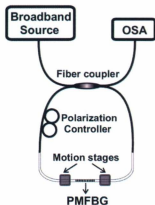


Figure 3-1: Schematic illustration of the experimental setup for transmission spectrum measurement of the fibre loop mirror.

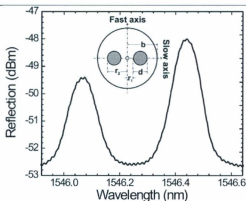


Figure 3-2: Reflection spectrum of the fibre Bragg grating imprinted polarization maintaining fibre. The inset shows the cross section of a PANDA fibre.

The FBG imprinted in the SLM can work as a reflector only at the Bragg grating resonance wavelengths and not affect the other wavelength regions where the Sagnac interference forms in the fibre coupler. The optical intensity transmission spectrum  $T(\lambda)$  of the SLM can be calculated using the Jones matrix method with an expression [28]

$$T(\lambda) = \sin^2(\pi LB / \lambda) \cos^2 \theta, \quad (3-1)$$

where  $L$  and  $B$  are the length and the birefringence of the PMF, respectively.  $\lambda$  is the operation wavelength.  $\theta$  is the angle between the input light and the fast axis of the PMF.

When the polarization controller is set to produce different input light polarization states, the transmission spectrum of the PMFBG superimposed SLM will alter. The simulated transmission spectra of the PMFBG in the SLM at different polarization states are shown in Fig. 3-3. At  $90^\circ$ , the transmitted output of the filter is zero except that the resonance peaks of the PMFBG appear in the spectrum. This case is a pure PMFBG filter.

At  $50^\circ$ , the interference intensity of the SLM increases and exceeds that of the PMFBG, thus a comb filter forms. At  $70^\circ$ , PMFBG resonance peaks are superimposed on the SLM interferometric pattern. Figure 3-4 shows the experimental transmission spectrum changed from the PMFBG filter to SLM comb filter by adjusting the polarization controller. The experimental results are consistent with the theoretical analysis.

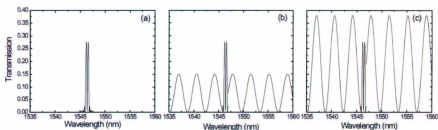


Figure 3-3: Simulated transmission spectra of the PMFBG in the Sagnac loop mirror at different polarization states: (a)  $90^\circ$ , (b)  $70^\circ$ , (c)  $50^\circ$ .

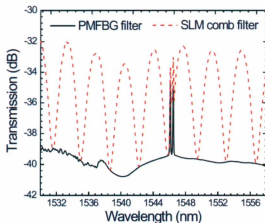


Figure 3-4: Transmission spectrum switching from PMFBG filter to SLM comb filter by adjusting the polarization controller.

When the axial strain changes from an initial axial strain  $\varepsilon_0$  to  $\varepsilon$  along a segment of the PMFBG with a length of  $l$ , a second-order Taylor series expansion around  $\varepsilon_0 = 0$  can be derived from Eqn. (3-1)

$$\begin{aligned} T(\lambda) &\approx \sin^2 \left( \frac{\pi((L-l) + l(1+\varepsilon))}{\lambda} \left( B(0) + \frac{dB(\varepsilon)}{d\varepsilon} \varepsilon \right) \right) \\ &= \sin^2 \left( \frac{\pi(L+l\varepsilon)}{\lambda} B(0) + \frac{\pi l(1+\varepsilon)\varepsilon}{\lambda} \frac{dB(\varepsilon)}{d\varepsilon} \right) \end{aligned} \quad (3-2)$$

From the Eqn. (3-2), the SLM peak wavelength requires

$$\lambda_k = \frac{(L+l\varepsilon)B(0)}{k} + \frac{l(1+\varepsilon)\varepsilon}{k} \frac{dB}{d\varepsilon} \quad (3-3)$$

Thus the gradient of the SLM peak wavelength due to the changes in the longitudinal strain and the corresponding change in the birefringence is

$$\frac{d\lambda_k}{d\varepsilon} = \frac{lB(0)}{k} + \left[ \frac{l}{k} \frac{dB}{d\varepsilon} + \frac{l\varepsilon}{k} \frac{d^2B}{d\varepsilon^2} \right] + \left[ \frac{2l\varepsilon}{k} \frac{dB}{d\varepsilon} + \frac{l\varepsilon^2}{k} \frac{d^2B}{d\varepsilon^2} \right] \quad (3-4)$$

The birefringence  $B$  of the PMF can be expressed as  $B = n_s - n_f$ , where  $n_s$  and  $n_f$  are the effective refractive index corresponding to the slow axis and fast axis of the PMF, respectively. The parameter  $B$  of a PMF is given by [29]

$$B = B_G + B_{S_0} + B_S, \quad (3-5)$$

where  $B_G$  is the geometrical component,  $B_{S_0}$  is the self-stress component, and  $B_S$  is the outer stress-component. In the PANDA fibre, the modal birefringence components  $B_G$  and  $B_{S_0}$  are zero.  $B_S$  can be expressed as [29]

$$B_S = \frac{\alpha_T (T - T_S) n_1^3 (P_{11} - P_{12})(1 + \nu) (r_2 - r_1)}{(1 - \nu^2) (r_2 + r_1)} \left\{ 1 - \frac{3}{b^4} (r_2 - r_1)^4 \right\}. \quad (3-6)$$

Where  $T$  is the environmental temperature around the fibre,  $T_S$  is the softening temperature of the optical fibre core (about 690 °C),  $r_1$  and  $r_2$  are the corresponding inner and outer radii of the stress-applying parts to the fibre core,  $b$  is the outer cladding radius, and all the other parameters are constants as defined in [29], i.e.,  $\alpha_T$  is the difference of thermal coefficient between the core and the cladding,  $n_1$  is the fibre core index,  $P_{11}$  and  $P_{12}$  are the strain-optic constants,  $\nu$  is Poisson's ratio. The inset of Fig. 3-2 illustrates the cross section of a PANDA fibre where the diameter of the stress-applying part is denoted by  $d$ .

If the parameters of the stress applying part,  $r_1$ ,  $r_2$ , and  $d$ , are assumed unchanged as the PMF is axially stretched from  $l$  to  $l+\Delta l$ , the outer cladding radius will change from  $b$  to  $b'$

$$b' = b\sqrt{\frac{l}{l+\Delta l}} = b\sqrt{\frac{1}{1+\varepsilon}}. \quad (3-7)$$

Following Eqn. (3-6), the birefringence  $B(\varepsilon)$  of a PANDA PMF in an environment of constant temperature can be written as

$$B(\varepsilon) = c_1 \left( 1 - \frac{3d^4}{b^4} \right) = c_1 \left( 1 - \frac{3(1+\varepsilon)^2 d^4}{b^4} \right) = -c_0 (1+\varepsilon)^2 + c_1, \quad (3-8)$$

where  $c_0$  and  $c_1$  are positive constants. For environmental temperature of 20°C,  $c_0$  and  $c_1$  are calculated to be  $0.96 \times 10^{-4}$  and  $4.64 \times 10^{-4}$ , respectively.

Through adjusting the polarization controller, the PMFBG resonance peaks were superimposed on the SLM interferometric pattern. The axial strain on a length of 40 cm PMF with the PMFBG in the center was changed from 0 to 1000  $\mu\varepsilon$  while the

temperature was kept at room temperature of 20 °C.

Figure 3-5 shows the transmission spectra of the FBG imprinted polarization maintaining fibre SLM with the axial strain changing from 100  $\mu\epsilon$  to 900  $\mu\epsilon$  and the inset gives the redshifts in the resonance peaks of the FBG under the two axial strains. When a grating is inscribed in a PMF, two Bragg resonance wavelengths corresponding to the slow and fast axes of the FBG, i.e.  $\lambda_S$  and  $\lambda_F$ , are  $\lambda_{S,F} = 2n_{S,F}\Lambda_{\text{FBG}}$ , where  $\Lambda_{\text{FBG}}$  is the grating period [30].

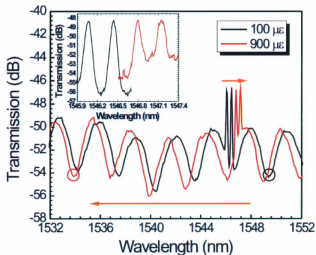


Figure 3-5: Transmission spectra of the FBG-PMF in the fibre Sagnac loop mirror at 100 and 900  $\mu\epsilon$ . The inset shows the redshifting transmission spectra of the FBG-PMF from 100  $\mu\epsilon$  to 900  $\mu\epsilon$ .

The slow-axis and fast-axis Bragg wavelengths of the FBG exhibit redshifts from 1546.437 and 1546.071 nm to 1547.140 and 1546.802 nm, respectively. However the difference in their Bragg wavelengths decreases from 0.366 nm to 0.338 nm. This is

because the birefringence will decrease with the increasing axial strain from Eqn. (3-7).

From the applied strain value of  $100 \mu\epsilon$  to  $900 \mu\epsilon$ , the SLM peak wavelength of  $1549.400 \text{ nm}$ , corresponding to the mode number  $k = 420$ , blueshifts to  $1533.850 \text{ nm}$  with a wavelength shift of  $15.550 \text{ nm}$ . The Eq. (3-4) can be rewritten with Eq. (3-7) as

$$\frac{d\lambda_k}{d\epsilon} = \frac{B(0)}{k} - \frac{2c_0 l}{k} (1 + 4\epsilon + 3\epsilon^2) \approx \frac{B(0)}{k} - \frac{2c_0 l}{k} \quad (3-9)$$

The higher order strain effect on the birefringence can be neglected for axial strain  $\sim 10^{-3}$  and thus the SLM peak wavelength responds linearly to small axial strain. Furthermore, it is indicated that different mode number will induce different changes of FSI peak wavelengths due to axial strain and a smaller mode number has a larger wavelength gradient.

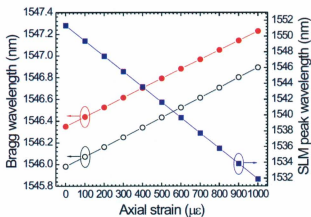


Figure 3-6: Axial strain dependences of the PMFBG Sagnac loop mirror. The solid circles and open circles stand for the Bragg resonance wavelengths of the slow axis and the fast axis as a function of axial strain, respectively. The solid squares represent the fibre SLM interferometric peak wavelength as a function of axial strain for  $k = 420$ .

When the applied axial strain was changed from 0 to 1000  $\mu\epsilon$ , the Bragg resonance wavelength of FBG as a function of the increasing axial strain is shown in Fig. 3-6. The two Bragg resonance wavelengths redshift linearly with the increasing axial strain. The axial strain sensitivities for the Bragg resonance wavelengths along the slow axis and fast axis are  $8.77 \times 10^{-4}$  and  $9.11 \times 10^{-4}$  nm/ $\mu\epsilon$ , respectively. The SLM peak wavelength ( $k = 420$ ) as a function of the axial strain is also shown in Fig. 3-6, which exhibits a blueshift with an axial strain sensitivity of  $1.9437 \times 10^{-2}$  nm/ $\mu\epsilon$ , respectively.

The wavelength spacing  $\Delta\lambda$  is inversely proportional to the birefringence and the total length of the PMF due to  $\Delta\lambda = \lambda^2/BL$  [28]. When axial strain applied on a section of the PMF including the PMFBG, the wavelength spacing can be expressed as

$$\Delta\lambda = \frac{d^2\lambda_k}{d\epsilon dk} = \frac{(2c_0 - B(0))l}{k^2} \quad (3-10)$$

It is indicated that different mode number has different wavelength spacing and strain applying length of the PMF determines the change of wavelength spacing. In this case, the wavelength spacing for the mode number of 420 is changed from 3.86 nm to 3.71 nm. A shorter strain applying fibre length can minimize the strain effect on the wavelength spacing.

In this section laser wavelength control by the use of fibre Bragg grating imprinted polarization maintaining fibre Sagnac loop mirror has been demonstrated through polarization and strain tuning. The combination of fibre Bragg grating and fibre loop mirror realizes transmission spectrum switching from PMFBG filter to SLM comb filter. The interferometric peak wavelengths of the Sagnac loop mirror exhibit blueshifts with

the increasing strain in comparison with the redshifts for the Bragg resonance wavelengths of the grating, which provides an opportunity to achieve wavelength selectivity and compensation. Furthermore, the pronounced difference in the bandwidths of the resonance peak of the fibre Bragg grating and the interferometric peak of the Sagnac loop mirror as well as their tunability, offer a possibility to achieve arbitrary switching from PMFBG filter to SLM comb filter easily realized by polarization control. In addition to the versatility in the selection of the Bragg wavelength of a FBG and the interferometric peaks of a loop mirror to satisfy specific applications, the realization of the technique on a standard PANDA fibre provides a simple and low-cost approach, which is compatible with the existing fibre-optic systems.

### **3.3 Wavelength Locking and Spectral Filtering with Fibre Sagnac Loop Mirror by Temperature Tuning**

In this section, a tunable fibre Sagnac loop mirror incorporating a fibre Bragg grating embedded polarization maintaining fibre to achieve simultaneous wavelength locking and spectral filtering by temperature tuning is studied. The proposed scheme combines the advantages of the Bragg resonance peak of the FBG and the interferometric pattern of the SLM for wavelength control, which renders FBG with more functionalities in wavelength control in addition to the wavelength locking. As shown in Fig. 3-7, the experiment was carried out on a fibre SLM with a broadband light source (EBS-7210, MPB

Communications) incident on a single-mode 50:50 fibre coupler and the detection of the transmission spectra was achieved by an optical spectrum analyzer (Ando AQ6315E) after the two light beams passing through a polarization controller (HP 11896A) and a 10cm-FBG embedded 210cm-PMF (PANDA, Thorlabs), for which a section of 35 cm containing the grating section was placed in a heating tube with a temperature resolution of 0.1°C. The fast-axis Bragg resonance wavelength of the FBG is 1546.013 nm with a reflection of 3.30 dB and the slow-axis Bragg resonance wavelength is 1546.385 nm with a reflection of 4.39 dB.

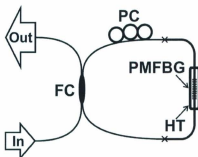


Figure 3-7: Schematic illustration of the experimental setup. PC, polarization controller; FC, fibre coupler; HT, heating tube.

The optical intensity transmission spectrum  $T(\lambda)$  of the SLM can be calculated using the Jones matrix representation with an expression [10]

$$T(\lambda) = \sin^2\left(\frac{\pi LB}{\lambda}\right), \quad (3-11)$$

where  $L$  and  $B$  are the length and the birefringence of the PMF, respectively.  $\lambda$  is the operation wavelength. When the temperature changes along a length  $l$  of the PMF

containing the FBG, a second-order Taylor series expansion around an initial temperature

$T_0$  can be deduced from Eqn. (3-11)

$$T(\lambda) = \sin^2 \left( \frac{\pi L}{\lambda} B(T_0) + \frac{\pi L}{\lambda} \frac{dB(T)}{dT} (T - T_0) \right). \quad (3-12)$$

An SLM interferometric peak occurs when the phase of the sine function in Eqn. (3-12) equals  $k\pi$ , where  $k$  is an integer. The corresponding SLM interferometric peak wavelength is

$$\lambda_k = \frac{LB(T_0)}{k} + \frac{l}{k} \frac{dB}{dT} (T - T_0). \quad (3-13)$$

Thus the gradient of the SLM peak wavelength due to the changes in the environmental temperature and the birefringence is

$$\frac{d\lambda_k}{dT} = \frac{l}{k} \frac{dB}{dT} + \frac{l}{k} \frac{d^2B}{dT^2} \Delta T. \quad (3-14)$$

The birefringence  $B$  of a PMF can be expressed as  $B = n_s - n_f$ , where  $n_s$  and  $n_f$  are the effective refractive indices corresponding to the slow-axis and the fast-axis of the PMF, respectively. The Bragg resonance wavelengths of a FBG in a PMF,  $\lambda_i$ , in which the subscript  $i$  stands for the slow axis ( $i = s$ ) or fast axis ( $i = f$ ), correspond to the center wavelength of the light back-reflected from the grating along slow- and fast-axis, which depends on the effective index of refraction of the core ( $n_i$ ) and the periodic spacing of the grating ( $\Lambda_{\text{FBG-PMF}}$ ) through the relationship  $\lambda_i = 2n_i \Lambda_{\text{FBG-PMF}}$ . Parameters such as  $n_i$  and  $\Lambda_{\text{FBG-PMF}}$  are both sensitive to a change in strain or temperature. Figure 3-8 shows the transmission spectra of the FBG embedded SLM with the environmental temperature varying from 20 °C to 60 °C and the enlarged curves indicate the redshifted transmission

spectra of the FBG at the two temperatures. The SLM interferometric pattern indicates a relatively broad bandwidth with a 3-dB bandwidth of 2.10 nm, however, the FBG exhibits a narrow 3-dB bandwidth (0.13 nm) in its Bragg resonance wavelength. The birefringence  $B$  of a PMF is given by  $B = B_G + B_{S_0} + B_S$  [29], where  $B_G$  is the geometrical component,  $B_{S_0}$  is the self-stress component, and  $B_S$  is the outer stress-component. In the PANDA fibre the modal birefringence components  $B_G$  and  $B_{S_0}$  are zero.  $B_S$  can be expressed as

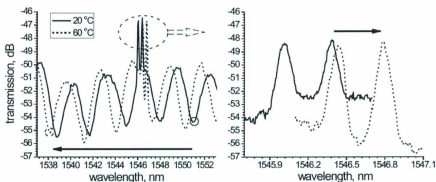


Figure 3-8: Left: Transmission spectra of the FBG-PMF Sagnac loop mirror at 20°C and 60°C. Right: The enlarged curves show the redshifts in the Bragg wavelengths of the FBG along both the slow and fast axes.

$$B_S = \frac{\alpha_r(T - T_S)n_1^3(P_{11} - P_{12})(1 + \nu)}{(1 - \nu^2)} \frac{(r_2 - r_1)}{(r_2 + r_1)} \left\{ 1 - \frac{3}{b^4}(r_2 - r_1)^4 \right\}. \quad (3-6)$$

where  $T_S$  is the softening temperature of the optical fibre core (about 690 °C),  $T$  is the environmental temperature surrounding the fibre, and all other parameters are constants. Therefore, the birefringence  $B$  of a PMF can be written as  $B = -aT + b$ , where  $a$  and  $b$  are constants, calculated to be  $4.4 \times 10^{-7} \text{ } ^\circ\text{C}^{-1}$  and  $3.1 \times 10^{-4} \text{ } ^\circ\text{C}^{-1}$ , respectively.

Figure 3-8 indicates that the slow-axis and fast-axis Bragg resonance wavelengths of the FBG redshift with the increasing temperature from 1546.385 nm and 1546.013 nm to 1546.78 nm and 1546.43 nm, respectively. However, the difference between the two Bragg wavelengths decreases from 0.372 nm to 0.350 nm due to the decrease of the birefringence with the increasing temperature, which is evident from the simplified expression of  $B$  and the relationship between the Bragg wavelength and the refractive index of the fibre. One SLM peak wavelength of 1550.900 nm at 20 °C with the corresponding  $k$  value of 420 blueshifts to 1538.025 nm at 60 °C, exhibiting a wavelength shift of 12.875 nm. For the interferometric peak wavelength of the FBG as a function of increasing temperature, the two Bragg resonance wavelengths redshift linearly with the increase in temperature, as shown in Fig. 3-9. The temperature sensitivities of the Bragg resonance wavelengths along the slow axis and fast axis are  $9.875 \times 10^{-3}$  and  $10.425 \times 10^{-3}$  nm/°C, respectively. The SLM peak wavelength at  $k = 420$  as a function of temperature shown in Fig. 3-9 indicates blueshift with a temperature sensitivity of  $3.219 \times 10^{-1}$  nm/°C. The Eqn. (3-14) can thus be expressed as  $d\lambda_x/dT = -a/k$ ,  $d(d\lambda_x/dT)/dk = a/k$ . The values of the fibre length or the interference order, which are experimentally selectable, can be used to change the output transmission properties, in which change of the fibre length is easier to achieve. The value of  $d(d\lambda_x/dT)/dk$  here is 5.2 pm/°C, indicating that the wavelength difference of neighbouring maxima during a temperature change of 40 °C can be resolved by the OSA (maximum wavelength resolution 50 pm). On the other hand, a short fibre can be adopted to tune the spectral characteristics as a whole without changing the wavelength difference between neighbouring transmission

maxima during temperature change. If the fibre is shorter than 0.5 m in this case, the change in the wavelength difference will be negligible as it cannot be detected by the OSA. The possibility of adjusting the fibre length provides an opportunity to satisfy specific applications.

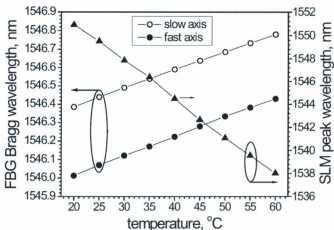


Figure 3-9: Temperature dependences of the FBG-PMF Sagnac loop mirror. The dots stand for the Bragg resonance wavelengths of the FBG along either the slow axis or the fast axis. The triangles represent the interferometric peak wavelengths of the SLM with  $k = 420$ .

In this section we present a tunable SLM incorporating an FBG embedded polarization maintaining fibre to achieve spectral filtering by temperature tuning. In this scheme, the interferometric peaks of the SLM and the Bragg resonance wavelengths of the FBG exhibit opposite temperature sensitivities. The proposed SLM possesses comb-like transmission characteristics, where the spectral characteristics can be tuned as a whole through temperature adjustment and the wavelength differences between neighbouring transmission maxima during temperature change can be intentionally set to

### 3.4 Temperature and Strain Sensing with Fibre Sagnac Interferometer

In this section, simultaneous temperature and axial strain measurement with a fibre Bragg grating imprinted polarization maintaining fibre Sagnac interferometer is achieved. The fibre Sagnac interferometer (FSI) sensor is capable of simultaneously measuring two measurands by monitoring the changes in the fast axis and slow axis polarization maintaining fibre Bragg resonance wavelengths and multiple interference peak wavelengths of the fibre Sagnac interferometer. A character matrix of the fibre Sagnac interferometer sensor is defined to represent its multiparameter sensing performance.

Figure 3-10 shows the experimental setup for transmission spectrum measurement of the fibre Sagnac interferometer with a PMFBG. Light emitted from a broadband light source (BBS) was received by the optical spectrum analyzer (OSA) after passing through a fibre optical polarizer and a singlemode 3-dB fibre-optic coupler (FOC) with 50:50 split ratios. A fibre Sagnac interferometer is formed when a polarization maintaining fibre Bragg grating connects the ends of the two arms where beams propagate clockwise (CW) and counterclockwise (CCW). Two optical fibre polarization controllers (PC) are set to adjust the input light polarization states in both beam propagation directions. The first polarization controller, PC1 (HP 11896A), changes angle  $\theta_1$  between the CW beam and

the fast axis or the slow axis of the PMF. A three-paddle manual fibre polarization controller, PC2, controls angle  $\theta_2$  between the CCW beam and the fast axis or slow axis of the PMF.  $\theta_1$  and  $\theta_2$  will not change because the polarization states are maintained in PMF for both the CW and CCW beams. The two beams recombine at the FOC and the interference signal due to a phase difference is detected by the OSA. The transmission spectrum  $T(\lambda)$  of the FSI can be calculated using the Jones matrix method and written as [18, 24]

$$T(\lambda) = \left[ \cos\left(\frac{\pi L B}{\lambda}\right) \sin(\theta_1 + \theta_2) \right]^2 \quad (3-15)$$

where  $L$  and  $B$  are the length and the birefringence of the PMF, respectively.  $\lambda$  is the operation wavelength.

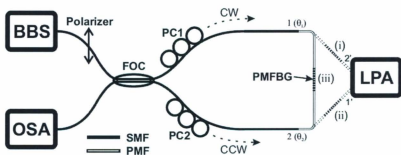


Figure 3-10: Schematic illustration of the experimental setup for transmission spectrum measurement of the fibre Sagnac interferometer with PMFBG at different input light polarization states. PC, polarization controller; FOC, fibre-optic coupler; CW, clockwise; CCW, counterclockwise; LPA, lightwave polarization analyzer.

When the polarization controllers are set to produce different input light polarization states, the transmission spectrum of the PMFBG superimposed FSI will alter. A lightwave

polarization analyzer (LPA, Agilent 8509C) was used to examine the output light polarization states from the polarization controller and obtain an input light into the polarization maintaining fibre with well-defined orthogonal linear polarization states along the slow axis or the fast axis of the PM fibre. The transmission spectra of the PMFBG in the FSI at three different polarization states are discussed with the results shown in from Fig. 3-11 to Fig. 3-15. (I) In this case, one end of the polarization maintaining fibre, 2, was connected to the lightwave polarization analyzer. The Sagnac loop was broken and only a reflection spectrum of the PMFBG was recorded by the OSA. When the PC1 was set at  $\theta_1 = 0^\circ$ , a reflection spectrum of the PMFBG with a fast-axis Bragg resonance wavelength  $\lambda_F$  of 1546.039 nm is observed, as shown in Fig. 3-11. When the PC1 was set at  $\theta_1 = 90^\circ$ , a reflection spectrum of the PMFBG with a slow-axis Bragg resonance wavelength  $\lambda_S$  of 1546.408 nm is observed, which is shown in Fig. 3-12.

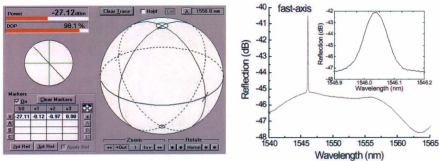


Figure 3-11: Left: The Agilent 8509C measurement screen. Right: Reflection spectrum of PMFBG when the polarization state of PC1 was aligned to the fast-axis. Inset in the right figure shows the enlarged reflection spectrum of PMFBG.

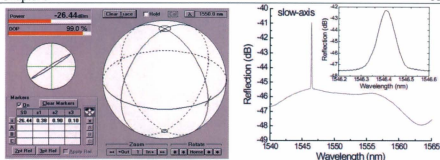


Figure 3-12: Left: The Agilent 8509C measurement screen. Right: Reflection spectrum of PMFBG when the polarization state of PC1 was aligned to the slow-axis.

(II) In this case, the other end of the polarization maintaining fibre, 1, was connected to the lightwave polarization analyzer. When the PC1 was set at  $\theta_2 = 0^\circ$ , a reflection spectrum of the PMFBG with a fast-axis Bragg resonance wavelength  $\lambda_F$  of 1546.032 nm is observed shown in Fig. 3-13. When the PC2 was set at  $\theta_2 = 90^\circ$ , a reflection spectrum of the PMFBG with a slow-axis Bragg resonance wavelength  $\lambda_S$  of 1546.416 nm is observed shown in Fig. 3-14.

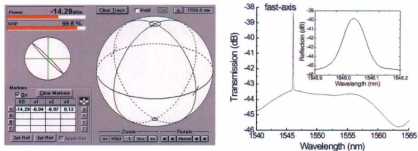


Figure 3-13: Left: The Agilent 8509C measurement screen. Right: Reflection spectrum of PMFBG when the polarization state of PC2 was aligned to the fast-axis.

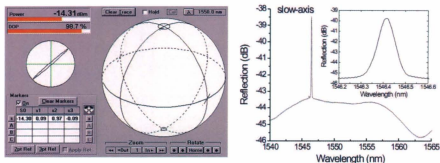


Figure 3-14: Left: The Agilent 8509C measurement screen. Right: Reflection spectrum of PMFBG when the polarization state of PC2 was aligned to the slow-axis.

(III) Two ends of the polarization maintaining fibre, 1 and 2, were connected to the polarization controllers, PC1 and PC2, respectively. A Sagnac loop was formed and a transmission spectrum of the Sagnac interferometer was recorded by the OSA. When the PC1 and the PC2 were set at  $\theta_1 = 0^\circ$  and  $\theta_2 = 0^\circ$ , the transmitted output of the Sagnac interferometer reaches a minimum and only a reflection spectrum of the PMFBG with a fast-axis Bragg resonance wavelength  $\lambda_F$  is observed as shown in Fig. 3-15(a). When the PC1 and the PC2 were set at  $\theta_1 = 90^\circ$  and  $\theta_2 = 90^\circ$ , the transmitted output of the Sagnac interferometer also reaches a minimum and only a reflection spectrum of the PMFBG with a slow-axis Bragg resonance wavelength  $\lambda_S$  is observed shown in Fig. 3-15(b). When the two polarization controllers were set at orthogonal linear polarization states, e. g.  $\theta_1 = 0^\circ$  and  $\theta_2 = 90^\circ$ , or  $\theta_1 = 90^\circ$  and  $\theta_2 = 0^\circ$ , the transmission spectrum of the Sagnac interferometer has a maximum extinction ratio shown in Fig. 3-15(c) and (d).

Simultaneously two PMFBG resonance peaks corresponding to the fast-axis and slow-axis are superimposed on the Sagnac interferometric pattern.

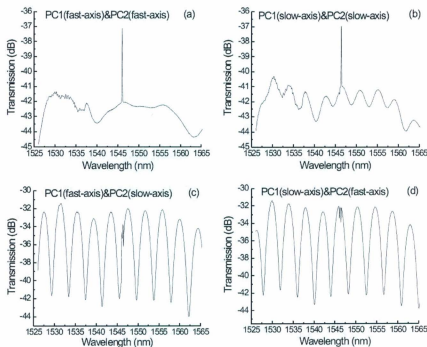


Figure 3-15: Transmission spectrum of the Sagnac interferometer with reflection spectrum of the PMFBG. (a) and (b): PC1 and PC2 are set to the same polarization states along either the fast axis or the slow axis of the PM fibre; (c) and (d): PC1 and PC2 are set to the orthogonal polarization states, one along the fast axis and the other along the slow axis of the PM fibre.

Figure 3-16 illustrates the schematic diagram of the simultaneous temperature and axial strain measurement setup. The transmission spectrum of the fibre inscribed with the PMFBG was measured by the OSA, which shows the fast axis Bragg resonance wavelengths at 1546.098 with reflection signals of 4.763 and the slow axis Bragg

resonance wavelengths at 1546.470 nm with reflection signals of 4.595 dB. The length of the PMF was 170 cm. A length of 20 cm with the PMFBG was placed on a thermal platform (Sigma Systems, Corp.) which has a resolution of 0.1 °C and two ends of the fibre with a length of 40 cm were fixed to two motion stages (ATS100, Aerotech, Inc) using epoxy glue. The angle  $\theta_1$  was adjusted using the PC1 to achieve a scan rotation of 180° with an interval of 5° and the angle  $\theta_2$  was kept the unchanged. A resultant PMFBG spectrum can be superimposed on the FSI spectrum to achieve an optimum fringe visibility of the fibre Sagnac interferometer by properly choosing  $\theta_1$ . The environmental temperature was changed from 20 °C to 80 °C with a step of 10 °C and the axial strain was changed from 0 to 1000  $\mu\epsilon$  with a step of 200  $\mu\epsilon$ .

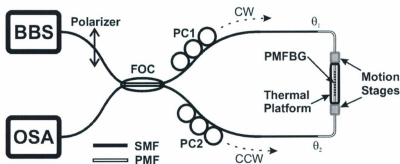


Figure 3-16: Schematic illustration of the experimental setup for simultaneous measurement of temperature and axial strain.

The operation principle of the simultaneous temperature and axial strain measurement is basically a fibre Sagnac interferometer with a broadband light source and detection of the interference spectrum response and the fibre Bragg grating resonance wavelength shift. Figure 3-17 show the transmission spectra of the PMFBG in a FSI with

the environmental temperature changing from 20 °C to 80 °C and the axial strain changing from 0 to 1000  $\mu\epsilon$ . Initially two FSI resonance wavelengths of 1596.92 nm ( $\circ$ ) and 1559.54 nm ( $\Delta$ ), corresponding to the  $k$  values of 401 and 411, were recorded at 0  $\mu\epsilon$  and 20 °C. When the temperature was increased to 80 °C, these two resonance wavelengths blueshift to the wavelengths of 1586.07 nm ( $\circ$ ) and 1549.39 nm ( $\Delta$ ) with corresponding wavelength shifts of 10.85 nm and 10.15 nm. When the axial strain was changed to 1000  $\mu\epsilon$ , these two resonance wavelengths blueshift to the wavelengths of 1576.41 nm ( $\circ$ ) and 1540.43 nm ( $\Delta$ ) with corresponding wavelength shifts of 20.51 nm and 19.11 nm. The two FSI resonance wavelengths continued to blueshift to the wavelengths of 1566.61 nm ( $\circ$ ) and 1531.26 nm ( $\Delta$ ), at 1000  $\mu\epsilon$  and 80 °C.

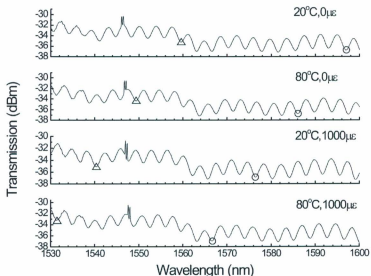


Figure 3-17: Transmission spectra of the PMFBG in the fibre Sagnac interferometer under different temperatures and axial strains.

Figure 3-18 shows the transmission spectra of the PMFBG in a FSI under different temperatures and axial strains. For the slow axis and fast axis Bragg wavelengths of the PMFBG, when the temperature was increased from 20 °C to 80 °C at 0  $\mu\epsilon$  they redshift from 1546.372 nm and 1545.990 nm to 1547.106 nm and 1546.730 nm, respectively. When the axial strain was changed from 0  $\mu\epsilon$  to 1000  $\mu\epsilon$  at constant 20 °C, the slow axis and fast axis Bragg resonance wavelengths of the PMFBG redshift from 1546.372 nm and 1545.990 nm to 1547.415 nm and 1547.044 nm, respectively.

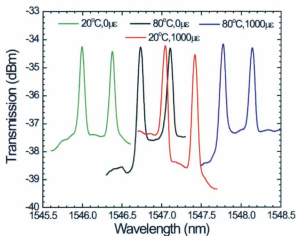


Figure 3-18: Transmission spectra of the PMFBG under different temperatures and axial strains.

When the environmental temperature was changed from 20 °C to 80 °C, the Bragg resonance wavelength of PMFBG and the FSI resonance peak wavelengths at  $k = 401$  and  $k = 411$  as a function of the increasing temperature is shown in Fig. 3-19(a). The two Bragg resonance wavelengths redshifts linearly with the temperature increased. The temperature sensitivities for the slow axis and fast axis are  $12.233 \times 10^{-3}$  nm/°C and

$12.333 \times 10^{-3} \text{ nm}^\circ\text{C}$ , respectively. The FSI resonance peak wavelengths at  $k = 401$  and  $k = 411$  are blueshift and have temperature sensitivities of  $180.833 \times 10^{-3} \text{ nm}^\circ\text{C}$  and  $169.166 \times 10^{-3} \text{ nm}^\circ\text{C}$ , respectively. When the applied axial strain was changed from 0 to  $1000 \mu\epsilon$ , the Bragg resonance wavelength of PMFBG and the FSI resonance peak wavelengths at  $k = 401$  and  $k = 411$  as a function of the increasing axial strain is shown in Fig. 3-19(b). The two Bragg resonance wavelengths redshifts linearly with the axial strain increased. The axial strain sensitivities for the slow axis and fast axis are  $1.043 \times 10^{-3} \text{ nm}/\mu\epsilon$  and  $1.054 \times 10^{-3} \text{ nm}/\mu\epsilon$ , respectively. The FSI resonance peak wavelengths at  $k = 401$  and  $k = 411$  are blueshift and have axial strain sensitivities of  $20.51 \times 10^{-3} \text{ nm}/\mu\epsilon$  and  $19.11 \times 10^{-3} \text{ nm}/\mu\epsilon$ , respectively.

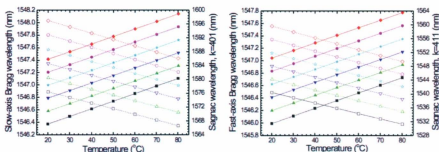


Figure 3-19: The slow-axis and fast-axis Bragg wavelengths (solid symbols) as well as fibre Sagnac interferometer resonance peak wavelengths of  $k = 401$  and  $k = 411$  (hollow symbols) as functions of temperature under different axial strain values.  $\blacksquare/\square$ ,  $0 \mu\epsilon$ ;  $\blacktriangle/\triangle$ ,  $200 \mu\epsilon$ ;  $\blacktriangledown/\triangledown$ ,  $400 \mu\epsilon$ ;  $\blackstar/\star$ ,  $600 \mu\epsilon$ ;  $\blacklozenge/\lozenge$ ,  $800 \mu\epsilon$ ;  $\blacklozenge/\lozenge$ ,  $1000 \mu\epsilon$ .

The fibre Sagnac interferometer resonance wavelength exhibits a larger variation than the Bragg resonance wavelengths under the same environmental change. The shifts in the

slow-axis Bragg wavelength and fibre Sagnac interferometer resonance wavelength at  $k =$

401 can be expressed as

$$\begin{bmatrix} \Delta\lambda_{\text{slow}} \\ \Delta\lambda_{k=401} \end{bmatrix} = \begin{bmatrix} 1.043 & 12.233 \\ -20.51 & -180.833 \end{bmatrix} \begin{bmatrix} \Delta\varepsilon \\ \Delta T \end{bmatrix} = M_{\sigma T(i,k)} \begin{bmatrix} \Delta\varepsilon \\ \Delta T \end{bmatrix}, \quad (3-16)$$

The shifts in the fast-axis Bragg wavelength and fibre Sagnac interferometer resonance wavelength at  $k = 411$  can be expressed as

$$\begin{bmatrix} \Delta\lambda_{\text{fast}} \\ \Delta\lambda_{k=411} \end{bmatrix} = \begin{bmatrix} 1.054 & 12.333 \\ -19.11 & -169.166 \end{bmatrix} \begin{bmatrix} \Delta\varepsilon \\ \Delta T \end{bmatrix} = M_{\sigma T(i,k)} \begin{bmatrix} \Delta\varepsilon \\ \Delta T \end{bmatrix}, \quad (3-17)$$

where  $i$  stands for the slow-axis ( $i = s$ ) or fast-axis ( $i = f$ ) of the polarization maintaining fibre, and  $k$  is an interferometer mode number of the FSI. The above two character matrices  $M_{\sigma T(i,k)}$  in Eqns. (3-16) and (3-17) both can be used to simultaneously determine the variations in axial strain and temperature from one of the two Bragg resonance wavelength shifts of the polarization maintaining fibre Bragg grating and any fibre Sagnac interference resonance peak wavelength.

It has also been found that the two Bragg resonance wavelengths of the polarization maintaining fibre Bragg grating exhibit distinct temperature and axial strain sensitivities in which the fast axis Bragg resonance wavelength exhibits higher sensitivities. Furthermore it is shown that different  $k$  values will induce different FSI resonance wavelength changes due to axial strain and environmental temperature changes where the fibre Sagnac interferometer resonance wavelength at lower order exhibits higher sensitivities. The shifts in the slow-axis and fast-axis Bragg wavelengths can be written as

$$\begin{bmatrix} \Delta\lambda_{\text{slow}} \\ \Delta\lambda_{\text{fast}} \end{bmatrix} = \begin{bmatrix} 1.043 & 12.233 \\ 1.054 & 12.333 \end{bmatrix} \begin{bmatrix} \Delta\varepsilon \\ \Delta T \end{bmatrix} = M_{\sigma T(i)} \begin{bmatrix} \Delta\varepsilon \\ \Delta T \end{bmatrix}, \quad (3-18)$$

The shifts in the fibre Sagnac interferometer resonance wavelengths at  $k = 401$  and  $k = 411$  can be written as

$$\begin{bmatrix} \Delta\lambda_{k=401} \\ \Delta\lambda_{k=411} \end{bmatrix} = \begin{bmatrix} -20.51 & -180.833 \\ -19.11 & -169.166 \end{bmatrix} \begin{bmatrix} \Delta\varepsilon \\ \Delta T \end{bmatrix} = M_{sr(k)} \begin{bmatrix} \Delta\varepsilon \\ \Delta T \end{bmatrix}, \quad (3-19)$$

Utilizing the character matrix  $M_{e,\pi(i)}$  of the polarization maintaining fibre Bragg grating or the character matrix  $M_{e,\pi(k)}$ , it is also possible to discriminate axial strain and temperature cross-sensitivity effect.

Since the slow-axis and fast-axis Bragg wavelengths of the polarization maintaining fibre Bragg grating and the fibre Sagnac interferometer resonance wavelengths at different mode orders have different sensitivities, a character matrix  $M$  of the combination of the four peak wavelengths may determine four different parameters from the wavelength shifts. When this approach is extended to a general case to distinguish multiple measurands, the character matrix  $M$  for quantifying multi parameters becomes:

$$\begin{bmatrix} \Delta P_1 \\ \Delta P_2 \\ \vdots \\ \Delta P_n \end{bmatrix} = M^{-1} \begin{bmatrix} \Delta\lambda_1 \\ \Delta\lambda_2 \\ \vdots \\ \Delta\lambda_n \end{bmatrix}, \quad (3-20)$$

in which  $P_n$  stand for multiple parameters to be measured, and  $\Delta\lambda_n$  correspond to the wavelength shifts.

## **Chapter 4**

# **Tapered Optical Fibre Mach-Zehnder Interferometer**

### **4.1 Introduction**

Tapered fibre is a fibre that has reduced diameter in the transverse dimension along the length of the fibre [1, 2]. Fabrication procedures of a fibre taper involve removing the protective plastic coating, heating the fibre to its softening temperature, and pulling the two ends of fibre apart to reduce the fibre diameter and form a waist region [3-6]. The enhanced mode-field diameter within the tapered region in the single-mode fibre allows multimode light in the fibre core and cladding to propagate by total internal reflection between the fibre cladding and the surrounding air [7-10]. Similar to the tapered fibre, some other cladding mode excitation elements include long period gratings, fibre

lateral-shifted junctions, and etc. Fibre Mach-Zehnder interferometer consisting of two cladding mode excitation elements can be classified into two categories: symmetrical fibre Mach-Zehnder interferometer (sFMZI) and asymmetrical fibre Mach-Zehnder interferometer (aFMZI). Reported sFMZIs include four single-mode fibre splitters with strictly defined beam splitting ratios [11], mechanically induced two identical long-period fibre gratings (LPGs) in a photonic crystal fibre (PCF) [12], a fibre-taper section between a LPG pair [13], spliced two pieces of a PCF with a small lateral offset or collapsed air-holes of a single PCF [14], two core-offset attenuators on a single-mode fibre [15], two tandem fibre tapers by fusion splicing [16], a single abrupt taper in a single-mode fibre with a fibre end of an air-glass interface or gold coating [17, 18], and two points on a single-mode fibre by CO<sub>2</sub> laser irradiations [19]. The reported aFMZIs include a fibre multimode interferometric structure combined with a LPG [20], a nonadiabatic taper cascaded with a LPG [21], interaction of a misaligned fusion-spliced point with a LPG on a single-mode fibre [22], or on a PCF [23].

Refractive index (RI) and temperature are among the most important parameters in applications of process control in manufacturing industries, protection of ecosystems, and prevention of global warming, especially in chemical or food industries for quality control and in biosensing for monitoring molecular bindings or biochemical reactions. The standard technique to measure refractive index is a refractometer, for which many well-known apparatus such as Pulfrich and Abbe refractometers have been used for many decades [24]. Surface plasmon resonance (SPR) has also been adopted for refractive index measurement through evanescent waves in waveguide configurations [25].

However, all these apparatus are essentially bulky prism systems. Earlier work on fibre-optic sensors for refractive index measurement reported metal-coated side-polished fibres, tapered fibres, or multimode fibres with relatively thin cladding layers to excite SPRs [25, 26]. Besides the approach with evanescent waves from nanometer fibre tips coated with gold particles [27], a majority of fibre sensors for refractive index measurement utilized fibre gratings, i.e., long-period gratings (LPGs) and fibre Bragg gratings (FBGs). Recent work that reported refractive index measurement with LPGs are either gold-coated [28], arc-induced phase-shifted [29], asymmetric [30], or inscribed in air- and water-filled photonic crystal fibres [31]. Reported refractive index measurement with FBGs includes a metal-coated grating in a special single-mode fibre of larger core (26  $\mu\text{m}$ ) and thinner cladding (30  $\mu\text{m}$ ) [32], a tilted FBG with gold coating in single-mode fibre [33], and cladding mode resonances of etched-eroded FBG [34]. A few papers reported simultaneous sensing of refractive index and temperature using LPGs, modified FBGs and hybrid LPG-FBG structures [35-37], with complicated design, instable system, or high cost, which restricts their practical applications. The preparation of FBG usually involves photolithographically-fabricated phase mask, UV laser and optical setup for grating inscription. Though LPGs have been revealed to possess a high sensitivity to the refractive index of the ambient medium, the typical full width at half maximum of the resonance peak of a LPG is about tens of nanometers, which limits the measurement accuracy and its multiplexing capability. Most recently, optical refractive index sensors or refractometers based on all-fibre interferometers [38, 39] or resonators [40] have received considerable attention for their high sensitivity, absolute detection with wavelength

codified information, broad measurement range, and compact size. These fibre interferometric techniques are cumbersome systems with high cost and simultaneous sensing of refractive index and temperature is missing. In section 4.2, simultaneous measurement of refractive index and temperature is accomplished by using a sFMZI realized on tapered single-mode optical fibre.

Simultaneous measurement of strain and temperature is also very important for a lot of applications, such as non-destructive evaluation of civil infrastructure, structure inspection of aircrafts, and environmental monitoring including earthquake and volcano surveillance. A wide variety of optical fibre-based sensing techniques have been proposed to meet such requirements owing to advantages such as immunity to electromagnetic interference, compact size, potential low cost, and the possibility of distributed measurement over a long distance [41]. The FMZIs reported so far usually involve highly demanding fibre grating fabrication techniques, critical requirements on interferometer specifications, or the use of high-cost PCFs, which restrict their practical applications. Section 4.3 illustrates an in-line one-fibre approach to realize simultaneous measurement of axial strain and temperature. Two aFMZIs with different device architectures consisting of a fibre taper and a lateral-shifted junction are fabricated in a single-mode fibre using the electrical arc method. Different gradients of the attenuation peak wavelengths on axial strain and temperature for the two types of aFMZI at two interference orders will be investigated to demonstrate the effectiveness of the approach.

In section 4.4, a triple tapered fibre Mach-Zehnder interferometer with three fibre tapers of different sizes is fabricated. The attenuation spectrum of the triple tapered fibre

Mach-Zehnder interferometer is actually a resultant attenuation spectrum due to a superposition of the three Mach-Zehnder interference patterns of different interference lengths. The attenuation spectra of the triple tapered fibre interferometer are measured at different temperatures and analyzed in the spatial frequency domain by taking the fast Fourier transformation (FFT) of the corresponding attenuation spectra.

## 4.2 Symmetrical Fibre Mach-Zehnder Interferometer

In this section, simultaneous measurement of refractive index and temperature based on a symmetrical fibre Mach-Zehnder interferometer is studied. Compared with the techniques reported on the interferometers with tapered fibres for sensing applications [42, 43], a double tapered fibre Mach-Zehnder interferometer will be fabricated on single-mode fibre by using simple fusion splicing. Analysis on the simultaneous measurement of refractive index and temperature will be carried out to verify the experimental results.

A schematic illustration of the experimental setup for simultaneous measurement of refractive index and temperature is shown in Fig. 4-1(a). Lights from one S-band broadband source (BBS, ASE-FL7200, Thorlabs) and one dual-band (C and L band) BBS (EBS-7210, MPB Communications) were launched through two tandem fibre tapers and measured by an optical spectrum analyzer (Ando 6315E). Electrical arc method has been adopted to fabricate abrupt tapers in a fibre and the technique used here is much more simple and convenient which does not rely on specific capabilities of any particular fibre fusion splicer as reported previously [43]. Figure 4-1(b) shows an abrupt taper fabricated

by tapering a standard telecommunication single-mode optical fibre (SMF-28) using a FITELE S182A fusion splicer. Two ends of the fibre placed on the pre-aligned holding plates were stretched and the middle region was heated by arc from the two electrodes inside the fusion splicer. With appropriate arc power, arc duration, and stretching distance, the diameter of the fibre was sharpened to a waist diameter  $D_0$  of  $65\ \mu\text{m}$  with the taper length  $L_0$  of  $525\ \mu\text{m}$ . A FMZI will be formed when a second taper of the same geometry is produced away from the first one with a spatial separation, which was  $54\ \text{mm}$  here.

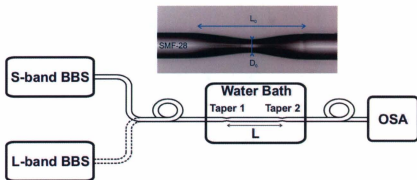


Figure 4-1: Schematic illustration of the experimental setup. Inset is a photo of a tapered fibre fabricated in this study with parameters of  $D_0 = 65\ \mu\text{m}$  and  $L_0 = 525\ \mu\text{m}$ .

In the unmodified single-mode optical fibre, only one fundamental linear polarization mode  $LP_{01}$  may propagate over a large distance as the fibre core mode. When the fibre taper structure is induced in the single-mode fibre, part of the light energy in the fibre core will be coupled into the cladding through the first taper while the second taper will couple most of the cladding mode energy back into the core after passing through a section of fibre between the two tapers, in which part of the energy is attenuated during the

cladding mode propagation. The phase difference  $\Phi$  between the core mode and the cladding mode can be approximated as  $\Phi = 2\pi\Delta n_{\text{eff}}L/\lambda$ , where  $\Delta n_{\text{eff}}$  is the difference of the effective refractive indices between the core and the cladding,  $L$  is the distance between the two tapers, and  $\lambda$  is the operating wavelength. When the phase difference satisfies the condition  $\Phi = (2m+1)\pi$ , where  $m$  is the order of the Mach-Zehnder interference, the attenuation peak wavelength  $\lambda_m$  can be found at

$$\lambda_m = \frac{2\Delta n_{\text{eff}}L}{2m+1}. \quad (4-1)$$

The spacing between the adjacent attenuation peak wavelengths,  $\Delta\lambda_m$ , is

$$\Delta\lambda_m = \lambda_{m-1} - \lambda_m = \frac{4\Delta n_{\text{eff}}L}{(2m-1)(2m+1)}. \quad (4-2)$$

When the refractive index of the medium surrounding the fibre taper increases, the effective refractive index of the cladding mode increases by an amount denoted as  $\delta n_{\text{eff,RI}}$  and that of the core mode hardly disturbed. Therefore the difference of the effective refractive indices between the core and the cladding modes due to the ambient refractive index,  $\Delta n_{\text{eff,RI}}$ , decreases by  $\delta n_{\text{eff,RI}}$ . The attenuation peak wavelength  $\lambda_{m,RI}$  will change to a shorter wavelength  $\lambda_{m,RI}'$  by  $\delta\lambda_{m,RI}$ , which is

$$\delta\lambda_{m,RI} = 2(\Delta n_{\text{eff,RI}} - \delta n_{\text{eff,RI}})L/(2m+1) - 2\Delta n_{\text{eff,RI}}L/(2m+1) = -2\delta n_{\text{eff,RI}}L/(2m+1) \quad (4-3)$$

In case the environmental temperature of the fibre tapers rises, both the effective refractive indices of the cladding mode and the core mode increase while that of the core mode changes more by  $\delta n_{\text{eff,T}}$  since the thermo-optic coefficient of the Ge-doped silica core is higher than that of the cladding consisting of fused silica. Consequently, the difference of the effective refractive index induced by the change in the environmental

temperature ( $\Delta n_{\text{eff},T}$ ) increases, as denoted by  $\delta n_{\text{eff},T}$ . The attenuation peak wavelength  $\lambda_{m,T}$

shifts to a longer wavelength  $\lambda_{m,T}$  by  $\delta \lambda_{m,T}$ , which is

$$\delta \lambda_{m,T} = 2(\Delta n_{\text{eff},T} + \delta n_{\text{eff},T})L/(2m+1) - 2\Delta n_{\text{eff},T}L/(2m+1) = 2\delta n_{\text{eff},T}L/(2m+1) \quad (4-4)$$

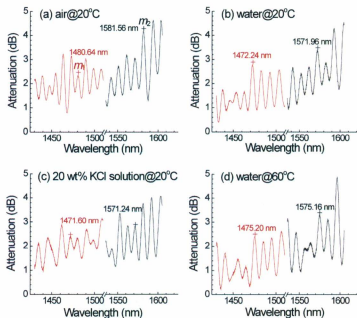


Figure 4-2: Attenuation spectra of the fibre Mach-Zehnder interferometer at different environmental conditions: (a) in air at 20 °C, (b) in water at 20 °C, (c) in 20 wt% KCl solution at 20 °C, and (d) in water at 60 °C.

In the experiment, the relationship between the inference peak wavelengths of the FMZI and the temperature was studied when the section containing the fibre taper pair was completely immersed in a water bath with a temperature resolution of 0.1 °C. The response of the FMZI to the surrounding refractive index was investigated using KCl

solution [44] while the temperature of the solution was maintained at  $20.0 \pm 0.1$  °C. At first the fibre tapers were placed in an environmental chamber at 20 °C with the attenuation spectra of the two tandem fibre tapers from their transmission spectra shown in Fig. 4-2(a). Two interference orders were arbitrarily selected, i.e., the interference order  $m_1$  (169) in the S-band with an attenuation peak wavelength  $\lambda_{m1}$  of 1480.64 nm and a spacing  $\Delta\lambda_{m1}$  of 8.80 nm and the interference order  $m_2$  (144) in the L-band with  $\lambda_{m2}$  of 1581.56 nm and  $\Delta\lambda_{m2}$  of 11.04 nm. The lower interference order  $m_2$  has a larger peak wavelength and spacing than those of the higher order  $m_1$ . When the fibre taper pair was transferred from ambient air to the water bath with the temperature maintained at 20 °C, it was found from Fig. 4-2(b) that the peak wavelengths of the orders  $m_1$  and  $m_2$  blue-shifted to 1472.24 and 1571.96 nm, respectively. Due to the decrease in  $\Delta n_{\text{eff,RI}}$  resulted from the increased surrounding refractive index from air (1.000) to water (1.333), the peak wavelengths of the orders  $m_1$  and  $m_2$  exhibit net shifts of 8.40 and 9.60 nm, respectively. Figure 4-2(c) shows the attenuation spectra of the fibre taper pair immersed in a 20 wt% KCl solution at 20 °C with a corresponding refractive index of 1.3606, which indicates that the two peak wavelengths of the orders  $m_1$  and  $m_2$  blue-shifted to 1471.60 and 1571.24 nm, respectively. When the temperature of the water bath was varied from 20 to 60 °C, two peak wavelengths of the orders  $m_1$  and  $m_2$  both red-shifted to 1475.20 and 1575.16 nm, respectively, as shown in Fig. 4-2(d). Redshifts of 2.96 and 3.20 nm in the peak wavelengths corresponding to the orders  $m_1$  and  $m_2$  have been identified, which take into consideration of the wavelength redshifts induced by the refractive index decrease of the water by 0.005 RIU (Refractive Index Unit) with the temperature increase of 40 °C.

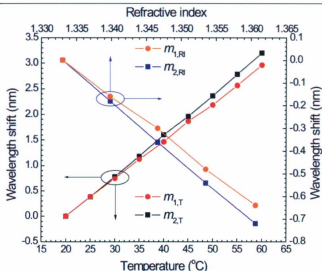


Figure 4-3: Dependences of the shifts of the attenuation peak wavelengths on refractive index and temperature for the interference orders  $m_1$  and  $m_2$ .

Figure 4-3 shows the dependences of the shifts in the peak wavelengths of the orders  $m_1$  and  $m_2$  on the changes in the refractive index and temperature. Compared with  $\lambda_{m1}$  in the S-band, the longer peak wavelength  $\lambda_{m2}$  in the L-band exhibits a larger shift under the same amount of change in the environmental parameter. Considering the shift due to the change in the refractive index of water with changing temperature, the sensitivities for  $m_1$  and  $m_2$  are -23.188 and -26.087 nm/RIU (blueshifts) for sensing refractive index, and 0.071 and 0.077 nm/°C (redshifts) for sensing temperature, respectively. It has been found that different interference orders have different FMZI peak wavelength gradients on temperature and refractive index. We define a character matrix  $M_{T,RI}$  to represent the sensing performance of the FMZI:

$$\begin{bmatrix} \Delta\lambda_1 \\ \Delta\lambda_2 \end{bmatrix} = M_{T,RI} \begin{bmatrix} \Delta T \\ \Delta n \end{bmatrix} = \begin{bmatrix} 0.071 & -23.188 \\ 0.077 & -26.087 \end{bmatrix} \begin{bmatrix} \Delta T \\ \Delta n \end{bmatrix}. \quad (4-5)$$

The character matrix  $M_{T,RI}$  can be used to simultaneously determine the variations in temperature and refractive index of the saline solution from the shifts of the attenuation peak wavelengths of the two arbitrarily selected interference orders  $m_1$  and  $m_2$ .

### 4.3 Asymmetrical Fibre Mach-Zehnder Interferometer

In this section, simultaneous measurement of axial strain and temperature based on an asymmetrical fibre Mach-Zehnder interferometer is investigated. Two aFMZIs with different device architectures consisting of a fibre taper and a lateral-shifted junction are fabricated in a single-mode fibre using the electrical arc method. Different gradients of attenuation peak wavelengths on axial strain and temperature for the two types of aFMZI at two interference orders will be investigated to demonstrate the effectiveness of the approach. Figure 4-4(a) shows a schematic illustration of an optical fibre device with a distance of  $l$  between a fibre taper (P) and a lateral-shifted junction (J). The abrupt fibre taper was shaped by tapering a standard telecommunication single-mode optical fibre (SMF-28e, Corning) using a fusion splicer (FITELE S182A). The fibre fixed on two aligned holding plates was stretched and the middle region was heated by arc from the two electrodes inside the fusion splicer. The fibre was sharpened to a waist diameter  $D_0$  of  $75 \mu\text{m}$  with a taper length  $l_0$  of  $470 \mu\text{m}$  as shown in the left inset of Fig. 4-4(b). To fabricate a lateral-shifted junction from two off-centered fibre cores, two pre-aligned

fibres with a designed lateral shift were fusion-spliced using the electrical arc method.

The right inset of Fig. 4-4(b) displays the optical micrograph of the lateral-shifted junction with a fibre core offset  $d_0$  of 5  $\mu\text{m}$ . Figure 4-4(b) shows that light emitted from an erbium broadband light source (EBS-7210, MPB Communications) is monitored by OSA (Ando 6315E) after passing through the fibre device. Light propagates through a fibre taper followed by a lateral-shifted junction is defined as an aFMZI of taper-junction type (P+J), and accordingly, an aFMZI of junction-taper type (J+P) is defined as light transmission through a lateral-shifted junction and a fibre taper in sequence.

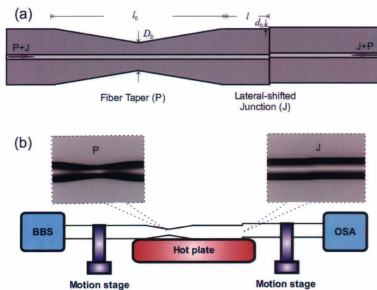


Figure 4-4: (a) Schematic illustration of the fibre device developed in this study, (b) experimental setup with the left and right insets showing the optical micrographs of the fibre taper (P) and the lateral-shifted junction (J) in the interferometer, respectively.

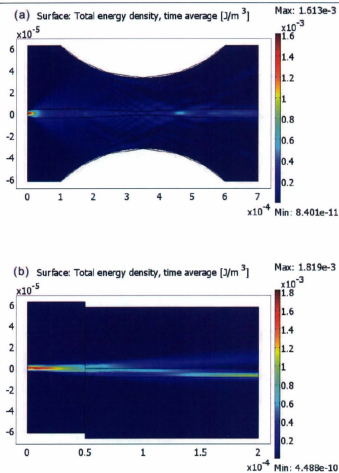


Figure 4-5: Simulation of light energy density distribution along (a) a fibre taper ( $D_0 = 70 \mu\text{m}$ ,  $l_0 = 500 \mu\text{m}$ ) and (b) a lateral-shifted junction ( $d_0 = 5 \mu\text{m}$ ) at  $\lambda = 1.55 \mu\text{m}$ .

A 2-D finite element analysis of both the fibre taper and the lateral-shifted junction has been used to verify the incident light energy propagation and the coupling effect. The procedure to use the commercial simulation software of Comsol Multiphysics is listed

below. Firstly the geometry structure of the fibre taper or the fibre lateral-shifted junction is drawn using the Draw Mode. Secondly the boundary condition is defined using Boundary Mode, such as scattering boundary condition and continuity condition. And then the refractive indices of fibre core and cladding are defined in the Subdomain Mode. The mesh is initialized with appropriate elements and degrees of freedom in the Mesh Mode. The electromagnetic parameters are defined such as free space wavelength and incident electric field. An in-plane TE waves is assumed to resolve the Maxwell equations and the results are presented in Fig. 4-5. For the fibre taper, excitation energy of  $LP_{01}$  in fibre core mode will be partly coupled to high-order  $LP_{0n}$  cladding modes at the beginning of the fibre taper region (Fig 4-5(a)). Similarly, part of the core mode energy also leaks to cladding modes at the junction position for the lateral-shifted junction (Fig 4-5(b)). An aFMZI will be formed when part of the light energy in the fibre core is coupled into the cladding by the first taper (or junction), and the second junction (or taper) couples the cladding mode energy back into the core after passing through a spatial separation between them.

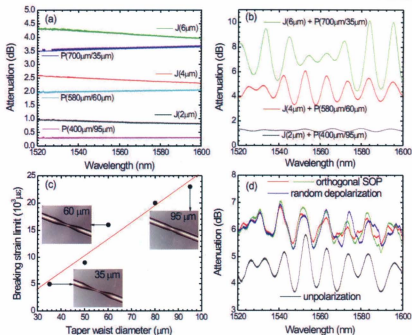


Figure 4-6: (a) Attenuation spectra of single fibre tapers (P) with different length/diameter ratios ( $l_0/D_0$ ) and single lateral-shifted junctions (J) with different parameters ( $d_0$ ), (b) attenuation spectra of J+P type aFMZIs with different parameters, (c) the dependences of breaking strain limit on the waist diameter of the fibre taper, and (d) attenuation spectra of the aFMZI of J(4  $\mu\text{m}$ )+P(580  $\mu\text{m}$ /60  $\mu\text{m}$ ) at different SOP.

In order to investigate the influence of structure parameters on the device performance, fibre tapers with different ratios of taper length to waist diameter from 700  $\mu\text{m}$ /35  $\mu\text{m}$ , 580  $\mu\text{m}$ /60  $\mu\text{m}$ , to 400  $\mu\text{m}$ /95  $\mu\text{m}$  and lateral-shifted junctions with different core offsets of 2, 4, and 6  $\mu\text{m}$  were fabricated on single-mode fibre with a core diameter of 8.2  $\mu\text{m}$ . Figure 4-6(a) shows the attenuation spectra of these different structures. Figure

4-6(a) indicates that the attenuation will increase when the ratio of taper length to waist diameter increases or the core offset expands. For the taper ( $700\ \mu\text{m}/35\ \mu\text{m}$ ) in the wavelength range of 1520 to 1600 nm, the minimal attenuation of 3.51 dB occurs at 1520 nm and the largest attenuation of 3.79 dB appears at 1600 nm because the mode field diameter (MFD) decreases with the decreasing wavelength and less energy is coupled from the core mode to the cladding modes at shorter wavelength region. In contrast, a rise in the attenuation spectrum of the lateral-shifted junction is observed. For the junction of  $d_0 = 6\ \mu\text{m}$ , the attenuation of 4.29 dB at a wavelength of 1520 nm decreases to 3.95 dB at 1600 nm with an attenuation difference of 0.34 dB. This is also due to the change in MFD while less energy is transferred between the two core modes and the loss is greater at a shorter wavelength. Figure 4-6(b) shows the attenuation spectra of J+P type aFMZIs with the combinations of these structure parameters. It is indicated that the aFMZI consisting of a longer and slimmer taper and a more misaligned junction has a higher extinction ratio (e.g. 6 dB for J( $2\ \mu\text{m}$ )+P( $700\ \mu\text{m}/35\ \mu\text{m}$ )) than the combinations of a shorter and thicker taper with a little lateral-shifted junction (e.g. 3 dB for J( $4\ \mu\text{m}$ )+P( $580\ \mu\text{m}/60\ \mu\text{m}$ ), 0.5 dB for J( $2\ \mu\text{m}$ )+P( $730\ \mu\text{m}/35\ \mu\text{m}$ )), nevertheless it suffers a larger attenuation (e.g. 7 dB for J( $2\ \mu\text{m}$ )+P( $700\ \mu\text{m}/35\ \mu\text{m}$ )) simultaneously. Figure 4-6(c) shows the dependence of the breaking strain limit on the waist diameter of the fibre taper, indicating that any decrease in the waist diameter of the fibre taper may reduce the mechanical strength of the fibre from a breaking strain limit of  $23 \times 10^3\ \mu\epsilon$  for the taper of  $d_0 = 95\ \mu\text{m}$  to  $5 \times 10^3\ \mu\epsilon$  for the taper of  $d_0 = 35\ \mu\text{m}$ . A taper with a waist diameter of  $75\ \mu\text{m}$  and a junction core offset of  $5\ \mu\text{m}$  was chosen for the sensing experiment because it achieves good interferometric

pattern of reasonable extinction ratio as well as adequate mechanical strength to withstand damage from fabrication, packaging and practical sensing applications. As it will be made clear in the next section, sensing with the aFMZIs in this study is achieved through the monitoring of the wavelength shift of the interferometric pattern, the extinction ratio of the device is not crucial for the sensing as long as an interferometric pattern is detectable. Figure 4-6(d) shows the attenuation spectra of the aFMZI of J(4  $\mu\text{m}$ )+P(580  $\mu\text{m}$ /60  $\mu\text{m}$ ) with different incident states of polarization (SOP) of orthogonal, random depolarized, and unpolarized polarization states modulated by a polarization controller (HP 11896A). It is indicated that the wavelength spacing and extinction ratio are closely related with the disturbance by polarization modulation. The polarization dependence of the aFMZI is mainly due to the refractive index difference between the core and cladding mode, which is polarization dependent and thus the phase difference is distinct in despite of a constant interferometer length.

The center peak wavelength is related to the mode coupling regions (P+J or J+P) through the multiplication of  $\Delta n_{\text{eff}}$  and  $L$ . Since the mechanism of the aFMZIs reported here is the Mach-Zehnder interferometry which is determined by the phase difference between the light beams propagating through the fibre core and cladding, thus the properties between the taper (P) and the junction (J), such as  $\Delta n_{\text{eff}}$  and  $L$ , are crucial, but not other details of the taper or the junction. The wavelength spacing between the adjacent attenuation peak wavelengths,  $\Delta\lambda_m$ , is  $\Delta\lambda_m = 4\Delta n_{\text{eff}}L/(2m+1)(2m-1) \approx \lambda_m^2/(\Delta n_{\text{eff}}L)$ , if  $m \gg 1$ . The relation between the wavelength spacing and the interferometer length is shown in Fig. 4-7, in which (a), (b), and (c) are the attenuation spectra of the J+P and P+J

type aFMZIs of J(4  $\mu\text{m}$ )+P(580  $\mu\text{m}/60 \mu\text{m}$ ) with different interferometer lengths of 2, 5, and 20 cm, respectively. Figure 4-7(d) indicates that the wavelength spacing is inversely proportional to the distance between the fibre taper and the lateral-shifted junction and the experimental results are consistent with the simulation. The differences in the effective refractive index of the P+J type aFMZI is calculated to be 0.004376 from the simulated results and that of the J+P type aFMZI as 0.004382 at a wavelength of 1530.00 nm. To study the energy distribution in the lower order cladding modes, the wavelength spectra of P+J type aFMZI in Figs. 4-7(a), (b), and (c) are Fourier transformed to obtain the spatial frequency spectra of the interference fringes [14].

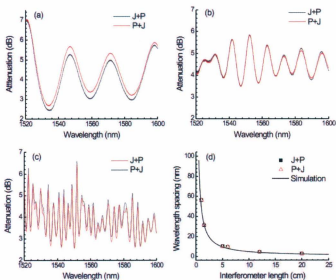


Figure 4-7: Attenuation spectra of J+P and P+J type aFMZIs with different interferometer lengths: (a) 2 cm, (b) 5 cm, (c) 20 cm, and (d) the dependence of wavelength spacing on the interferometer length for the two types of aFMZI.

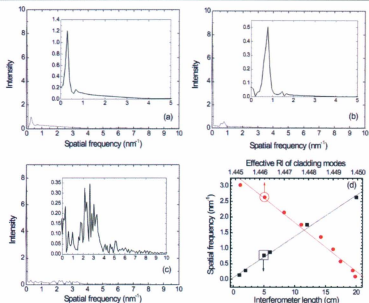


Figure 4-8: Spatial frequency spectra of J+P type aFMZIs with different interferometer lengths: (a) 2 cm, (b) 5 cm, (c) 20 cm, and (d) the dependences of spatial frequency on the interferometer length and cladding mode effective refractive index (RI) for the aFMZI of 20 cm in length.

In Figs. 4-8(a), (b), and (c), the dominant intensity peaks at zero spatial frequency relate to the core modes of the three J+P type aFMZIs with different lengths. The multiple minor intensity peaks in the insets of Fig. 4-8(a), (b), and (c) correspond to different orders of cladding modes of three aFMZIs. For the 20 cm aFMZI in the inset of Fig. 4-8(c), a series of intensity peaks are obvious in the spatial frequency spectrum and the sixth and the seventh have the highest peaks among them which indicate that these two orders of cladding modes have the largest energies after passing through the junction and taper region. Figure 4-8(d) shows that the spatial frequencies of the corresponding minor

peaks are proportional to the effective refractive indices of the lower order cladding modes for the same interferometer length  $L$  of 20 cm aFMZI in the inset of Fig. 4-8(c). Meanwhile, the figure also indicates that the spatial frequencies of the dominant peaks in the insets of Fig. 4-8 are proportional to the interferometer length which means that the mode coupling of different aFMZIs mainly occurs at the same orders of cladding modes of LP<sub>07</sub> or LP<sub>08</sub>.

For the measurement of the temperature ( $T$ ) and axial strain ( $\epsilon$ ) with the aFMZI, the optical fibre was axially stretched at different temperatures controlled by a Sigma system with a temperature accuracy of 0.1 °C. The aFMZI was fixed on two linear motion stages (ATS100, Aerotech, Inc.) using epoxy glue and the length of the fibre segment containing a 15 mm-long aFMZI of J(5 µm)+P(470 µm/75 µm) between the two fixed points was 330 mm. The axial strain was adjusted with the motion stage with a translation accuracy of 0.5 µm through general purpose interface bus system (GPIB) and LabVIEW programming control. In the initial temperature sensing measurement, the environmental temperature was first increased from 20 °C to 120 °C with no strain applied on two types of aFMZIs and after the first test, ambient temperature was cooled down to 20 °C and a second test was carried out to investigate the stability and reproducibility of the fibre sensor. The corresponding attenuation peak wavelength shifts in the attenuation spectra are shown in Fig. 4-9(a) and (b). In the first test, two interference orders  $m_1$  and  $m_2$  for P+J type aFMZI with the attenuation peak wavelengths  $\lambda_{m_1, P+J}$  of 1528.38 nm and  $\lambda_{m_2, P+J}$  of 1559.64 nm at 20 °C are calculated to be 49 and 48, respectively. Two interference orders  $m_1$  and  $m_2$  for J+P type aFMZIs show the attenuation peak wavelengths  $\lambda_{m_1, J+P}$  of

1528.62 nm and  $\lambda_{m2,J+P}$  of 1559.9 nm at 20 °C, respectively. For the same interference order, the differences in the interferometer length ( $l + l_0$  and  $l$ ) and the effective refractive index induce a shift in the attenuation peak wavelength. The shift of the attenuation peak wavelength,  $\delta\lambda_{m,T}$ , due to temperature increase can be expressed as

$$\delta\lambda_{m,T} = \frac{2(\Delta n_{\text{eff},T} + \delta n_{\text{eff},T})L}{2m+1} - \frac{2\Delta n_{\text{eff},T}L}{2m+1} = \frac{2\delta n_{\text{eff},T}L}{2m+1}, \quad (4-6)$$

where  $\delta n_{\text{eff},T}$  is the increased difference in the effective refractive index induced by the increase of the environmental temperature. When the environmental temperature increases, the attenuation peak wavelength exhibits a redshift. The enhancement in the difference of the effective refractive index,  $\delta n_{\text{eff},T}$ , is about  $1.6 \times 10^{-5}$  with a temperature increase of 100 °C at a wavelength of 1530.00 nm. For the P+J type aFMZI, the temperature sensitivities at the order  $m_1$  and  $m_2$  are 60.6 and 64.0 pm/°C (redshifts), respectively. For the J+P type aFMZI, the temperature sensitivities at the order  $m_1$  and  $m_2$  are 60.2 and 63.4 pm/°C (redshifts), respectively. In the second test during the decreasing temperature, the temperature sensitivities at the order  $m_1$  and  $m_2$  are 60.2 and 63.8 pm/°C for the P+J type aFMZI and 59.9 and 63.2 pm/°C for the J+P type, respectively. Figure 4-9(c) shows average dependences of the peak wavelength shifts of the two types of aFMZI for different interference orders on the temperature change. The sensing performance shows good stability and reproducibility with a standard deviation of 0.3% of the mean value of temperature sensitivities within the linear range from 20°C to 100°C. It is noted that the lower interference order  $m_2$  shows a larger shift in the peak wavelength than that of the higher order  $m_1$ .

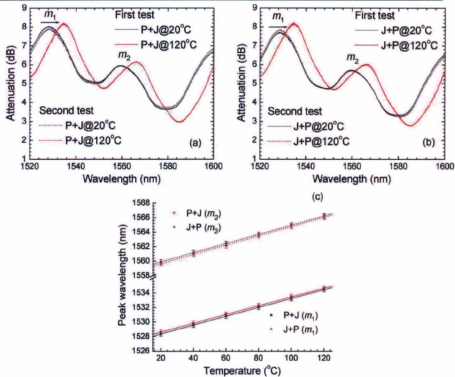


Figure 4-9: Attenuation spectra of aFMZIs at different environmental temperatures: (a) P+J type, (b) J+P type, and (c) the dependences of the shifts in the attenuation peak wavelengths of the two types of aFMZI on temperature at different interference orders without strain.

When an appropriate axial strain is applied on the two types of aFMZI kept at a constant temperature of 20 °C, the shifts in the attenuation spectra are shown in Fig. 4-10(a) and (b) as the axial strain is increased from 0 to 2000  $\mu\epsilon$ . In the first test during the increasing strain, two interference orders  $m_1$  and  $m_2$  for the P+J type aFMZI have the attenuation peak wavelengths  $\lambda_{m_1, P+J}$  of 1531.52 nm and  $\lambda_{m_2, P+J}$  of 1564.64 nm at 0  $\mu\epsilon$ ,

respectively, and the two interference orders  $m_1$  and  $m_2$  of the J+P type aFMZIs have the attenuation peak wavelengths  $\lambda_{m_1, J+P}$  of 1531.48 nm and  $\lambda_{m_2, J+P}$  of 1564.48 nm, respectively. The shift in the attenuation peak wavelength,  $\delta\lambda_{m,e}$ , due to the change in axial strain, can be expressed as

$$\delta\lambda_{m,e} = \frac{2(\Delta n_{\text{eff},e} - \delta n_{\text{eff},e})(L + \delta L)}{2m+1} - \frac{2\Delta n_{\text{eff},e}L}{2m+1} \approx \frac{2(\Delta n_{\text{eff},e}\delta L - L\delta n_{\text{eff},e})}{2m+1}, \quad (4-7)$$

where  $\delta L$  is the change in the interferometer length between P and J, and  $\delta n_{\text{eff},e}$  is the change in the effective refractive index due to the increase of the external axial strain. The increase in the fibre length due to axial strain and the accompanying decreases in the radii of the fibre core and cladding result in a decrease in the normalized frequency  $V$ . More power is transferred to the fibre cladding from the core by mode coupling and thus the difference in the effective refractive indices between the core and the cladding modes reduces. The increase in the aFMZI length,  $\Delta n_{\text{eff},e}\delta L$ , has a weaker impact on the peak wavelength shift than the influence of a decrease in the difference of the effective refractive indices,  $-L\delta n_{\text{eff},e}$ , so that the attenuation peak wavelength will blue-shift when the axial strain increases. The decrease in the difference of the effective refractive indices,  $\delta n_{\text{eff},e}$ , is calculated to be  $1.1 \times 10^{-5}$  with an increase in the axial strain of  $2000 \mu\epsilon$  at a wavelength of 1530.00 nm. For the P+J type aFMZI, the strain sensitivities at the order  $m_1$  and  $m_2$  are -1.48 and -2.72 pm/ $\mu\epsilon$  (blueshifts), respectively. For the J+P type aFMZI, the strain sensitivities at the order  $m_1$  and  $m_2$  are -1.51 and -2.76 pm/ $\mu\epsilon$  (blueshifts), respectively. In the second test during the increasing strain, the axial strain sensitivities at the order  $m_1$  and  $m_2$  are -1.46 and -2.7 pm/ $\mu\epsilon$  for the P+J type aFMZI and -1.5 and -2.74 pm/ $\mu\epsilon$  for the J+P type, respectively. Figure 4-10(c) shows the average dependences of

the shifts in the peak wavelengths of the two types of aFMZI at different interference orders on the change in the axial strain. Compared with the attenuation peak wavelength of the higher interference order, the peak wavelength of the lower interference order exhibits larger axial strain sensitivity. In addition, the aFMZIs studied here show good stability and high reproducibility in the sensing performance.

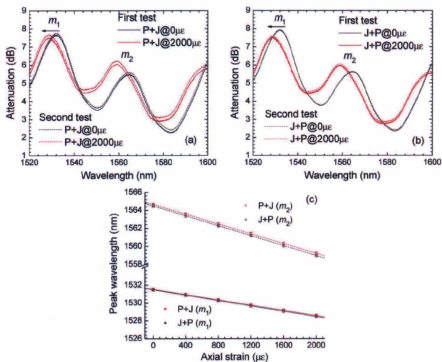


Figure 4-10: Attenuation spectra of the aFMZIs under different axial strains: (a) P+J type, (b) J+P type, and (c) the dependences of the shifts in the attenuation peak wavelengths of the two types of aFMZI on axial strain at different interference orders at 20°C.

The difference in the interferometer length  $L$  between these two types of aFMZI is

the taper length  $l_0$  because the mode coupling takes place at the beginning of the entry part of the fibre taper. The effect of the subtle discrimination of the phase difference in the interferometer due to the multiplication of the effective refractive index and the interferometer length for these two types of aFMZI gives rise to different temperature and axial strain sensitivities. The interferometer proposed in this study offers the possibility to configure it either as a direction independent or dependent sensor for different device architectures. In the case when the taper and the lateral-shifted junction locate spatially close, the sensitivities of the interferometer can be tuned to be direction dependent. However, if the length of the taper is much smaller than the distance between the taper and the lateral-shifted junction, the sensitivities of the interferometer on the environmental parameters are not dependent on the configuration of the interferometer and thus direction independent. In this case, the larger wavelength spacing resulted from the longer distance between the taper and the junction, as discussed in Fig. 4-7, may introduce inconvenience for the spectral measurement. With the specifications of the taper length and the interferometer length of the aFMZI adopted here, the sensitivity difference between the two types of aFMZIs is much smaller than that between different interference orders for the same type of aFMZI. It is obvious that different interference orders have different gradients of the peak wavelength on temperature and axial strain even for the same type of aFMZI. We define a character matrix  $M_{eT(P+J)}$  composed of the mean temperature and axial strain sensitivities of the two tests at the orders  $m_1$  and  $m_2$  to represent the sensing performance of the P+J type aFMZI:

$$\begin{bmatrix} \Delta\lambda_{n1} \\ \Delta\lambda_{n2} \end{bmatrix}_{P+J} = M_{\sigma T(P+J)} \begin{bmatrix} \Delta T \\ \Delta \varepsilon \end{bmatrix} = \begin{bmatrix} 60.4 & -1.47 \\ 63.9 & -2.71 \end{bmatrix} \begin{bmatrix} \Delta T \\ \Delta \varepsilon \end{bmatrix}, \quad (4-8)$$

which is equivalent to the following equation through a matrix transposition:

$$\begin{bmatrix} \Delta T \\ \Delta \varepsilon \end{bmatrix} = M_{\sigma T(P+J)}^{-1} \begin{bmatrix} \Delta\lambda_{n1} \\ \Delta\lambda_{n2} \end{bmatrix}. \quad (4-9)$$

A similar character matrix  $M_{\varepsilon T(J+P)}$  for J+P type of the aFMZIs may also be used for simultaneous sensing of the two parameters:

$$\begin{bmatrix} \Delta\lambda_{n1} \\ \Delta\lambda_{n2} \end{bmatrix}_{J+P} = M_{\varepsilon T(J+P)} \begin{bmatrix} \Delta T \\ \Delta \varepsilon \end{bmatrix} = \begin{bmatrix} 60.1 & -1.51 \\ 63.3 & -2.75 \end{bmatrix} \begin{bmatrix} \Delta T \\ \Delta \varepsilon \end{bmatrix}, \quad (4-10)$$

In this case, once the character matrix is obtained through calibration, simultaneous measurement of axial strain and temperature can be achieved by reading the shifts in the attenuation peak wavelengths of the two types of aFMZI. A comparison between the fibre Mach-Zehnder interferometer developed in this study and other reported fibre interferometers is listed in Table 4-1, which indicates advantages of the aFMZI developed in this study including easy fabrication by a fusion splicer and low cost using a standard single-mode telecommunication fibre, versatile in direction selection for the tunable sensing responses, and the possibility of multiparameter sensing. With regard to the practical applications of the aFMZI proposed in this study, as evident in Fig. 4-6(c), even though the mechanical strength of the tapered fibre decreases as compared with the standard single-mode fibre with coating, it is still possible to find a tapered fibre of suitable specifications to satisfy the requirement of axial strain measurement with an upper limit of  $23 \times 10^3 \mu\text{e}$ . As a matter of fact, tapered fibres have been widely adopted for sensing based on surface plasmon resonance [45], despite the degradation in the

mechanical strength. The fragility of a tapered fibre may be resulted from either the axial or radial strain. For packaging method, the tapered fibre can be laid into a micromachined channel fabricated on a solid substrate (for example, a piece of glass) so that the radial strain can be avoided. In this case, the tapered region won't touch the channel due to the reduced diameter while the bottom of the rest fibre with coating will touch the channel in which no strain is induced. When an axial strain is applied on the device, the tapered fibre will be lift up from the bottom of the microchannels without any contact.

In this section, an approach to realize simultaneous measurement of axial strain and temperature using an asymmetrical fibre Mach-Zehnder interferometer is demonstrated. The interferometer offers the possibility to tune its sensing performance either direction dependent or independent to satisfy requirements of specific applications. Furthermore, the asymmetrical structure of the interferometer with flexible device specifications as well as its arbitrarily selectable interference orders provides the feasibility to measure a large number of measurands with different sensitivities to environmental parameters, which make it possible to realize *in-situ* multiple parameter measurement.

Table 4-1 Comparison of the performance of the reported FMZIs.

Ref.	Fibre type	Interferometer structure	Fabrication technique	Measurands	Extinction ratio & Loss (device length)	Sensing performance
[12]	PCF	LPG pairs	Mechanical pressing with grooved plates onto a flat plate	—	4 dB & 4 dB	—
[13]	SMF	LPG-taper-LPG	LPG by excimer laser, and taper by stretching a fibre over a flame	RI	15 dB & 2 dB (12 mm)	49.4 nm/RIU
				RI	13 dB & 3 dB (16 mm)	173.8 nm/RIU
[14]	PCF	Core offset pairs	Cleaving and splicing using a fusion splicer	Strain	—	-2.16 pm/ $\mu\epsilon$ (1487 nm), -2.28 pm/ $\mu\epsilon$ (1560 nm)
		Collapsed air-holes	Electric arc of a fusion splicer	Strain		
[15]	SMF	Core offset pairs	Fusion splicing (Michelson)	RI	13 dB & 10 dB (60 mm)	-33.3 nm/RIU
[16]	SMF	Taper pairs	Fusion splicing	RI	6 dB & 14.0 dB (55 mm)	-17.1 nm/RIU
[17]	SMF	Taper pairs	Fusion splicing	Strain	24 dB & 3 dB	2000 nm/ $\epsilon$
[18]	SMF	Single taper with air-glass reflection end	Fusion splicing	Flow velocity	—	69.8 deg/bar (compressed air pressure)
[19]	SMF	Single taper with gold coating reflection end	Fusion splicing	RI	13 dB & 1 dB	29 nm/RIU
[20]	SMF	Two points	CO <sub>2</sub> laser irradiation	$T$	20 dB & 10 dB (5 mm)	0.0817 nm/ $^{\circ}$ C (5 mm)
[21]	SMF, MMF	MMF and LPG	Arc-induced LPG	Bending	13 dB & 8 dB	612.44 degrees.m
[22]	SMF	Taper and LPG	Taper by fusion splicing and arc-induced LPG	Rotation angle	1 dB & 2.5 dB	magnitude and sign of the rotation angle
[23]	SMF	Misaligned splicing point and LPG	Misaligned splicing point by fusion splicer and LPG by 244 nm laser	Strain & $T$	18 dB & 3 dB	59.1 pm/ $^{\circ}$ C -0.6 pm/ $\mu\epsilon$
This study	SMF	Taper and lateral-shifted junction	Fusion splicing	Strain & $T$	4 dB & 4 dB	$m_1$ and $m_2$ , -1.51 and -2.75 pm/ $\mu\epsilon$ , 60.4 and 63.9 pm/ $^{\circ}$ C

—, data not available; RI, refractive index; MMF, multimode fibre.

## 4.4 Triple Tapered Fibre Mach-Zehnder Interferometer

Fibre Mach-Zehnder interferometers consisting of multiple light-steering elements (fibre taper, fibre lateral-shifted junction) exhibits more complicated spectrum characteristics than those of the double-element fibre interferometers. In the attenuation spectrum of the triple tapered fibre interferometer, the interference resonance peak wavelengths of the in-line multiple fibre interferometers overlap and become indiscriminate. An alternative approach to realize sensing applications with a triple tapered fibre Mach-Zehnder interferometry of high sensitivity is desired. In this section a triple tapered fibre Mach-Zehnder interferometer is implemented by cascading three fibre tapers with different waist diameters. The attenuation spectra of the triple tapered fibre interferometer are measured at different temperatures and analyzed in the spatial frequency domain by taking the fast Fourier transformation (FFT) of the corresponding attenuation spectra.

Four triple tapered fibre Mach-Zehnder interferometers of different configurations were prepared using the electrical arc method. The first triple tapered fibre interferometer consists of three identical fibre tapers of Taper-1. A schematic illustration of the triple tapered fibre interferometer is shown in the inset of Fig. 4-11(b). The Taper-1 has a waist diameter  $D_0$  of 40  $\mu\text{m}$  and the interval between two adjacent fibre tapers measures  $L = 2.5$  cm. Part of the input light energy in the fibre core will be coupled into the cladding

through the first taper while the second taper will couple the first taper excited cladding mode energy back into the core and simultaneously recouple part of the core mode energy to the cladding mode energy. The third fibre taper will couple the first fibre taper and the second fibre taper excited cladding mode energies back to the core. The triple tapered fibre structure implies that there are three fibre Mach-Zehnder interferometers are incorporated in one three-tapered fibre, one with an interferometer length of  $2L$  between the first and second fibre taper and the other two with an interferometer length of  $L$ . Figure 4-11(a) shows the attenuation spectra of a fibre with only one single fibre taper, Taper-1, and the triple tapered fibre Mach-Zehnder interferometer of three Taper-1. In the attenuation spectrum of the fibre interferometer, there are several strong peaks in a period of 20 nm however each peak has different amplitude. Several weak peaks also appear between the strong peaks. The wavelength spacing between the adjacent attenuation peak wavelengths,  $\Delta\lambda$ , can be expressed as  $\Delta\lambda \approx \lambda^2/(\Delta n_{\text{eff}}L)$ . So the wavelength spacing is inversely proportional to the distance between the two fibre tapers. Thus the weak peaks are corresponding to the fibre interferometer length of  $2L$  and the strong peaks are due to both the fibre interferometer lengths of  $L$  and  $2L$ . The attenuation spectrum of the triple tapered FMZI is actually a resultant attenuation spectrum which has an irregular peak profile due to a superposition of the three Mach-Zehnder interference patterns of different interference lengths. The wavelength spectrum of the triple tapered fibre Mach-Zehnder interferometer in Fig. 4-11(a) is Fourier transformed to obtain the spatial frequency spectra of the interference fringes in Fig. 4-11(b) to study the multiple cladding modes interference with the core mode along an interference length of  $L$  or  $2L$ .

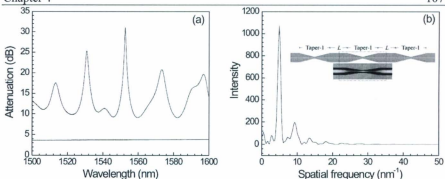


Figure 4-11: (a) Attenuation spectra of a single fibre taper and triple tapered fibre interferometer consisting of Taper-1. (b) Spatial frequency spectrum of the triple tapered fibre interferometer. Inset of (b) is a schematic illustration of the triple tapered fibre interferometer with an optical micrograph of Taper-1.

For the phase difference  $\Phi$  between two tapers with a distance of  $l$ , it can be expressed as  $\Phi = 2\pi\Delta n_{\text{eff}}l/\lambda$ , where  $\lambda$  is the operation wavelength and  $\Delta n_{\text{eff}}$  is the difference of the effective refractive indices between the core and the cladding modes. A first-order Taylor series expansion around  $\lambda = \lambda_0$  in the expression of the phase difference  $\Phi$  can be derived [14],

$$\phi \approx \phi_0 - \frac{2\pi\Delta n_{\text{eff}}l}{\lambda_0^2}(\lambda - \lambda_0) \quad (4-11)$$

The multiple intensity peaks in Fig. 4-11(b) correspond to the interference patterns of different optical path length ( $\Delta n_{\text{eff}}l$ ) in Fig. 4-11(a) with an expression of  $\cos(2\pi\zeta(\lambda - \lambda_0))$ , where  $\zeta$  is the spatial frequency. Compared with Eqn. (4-11),  $\zeta$  can be written as [14]

$$\zeta = \frac{\Delta n_{\text{eff}}l}{\lambda_0^2} \quad (4-12)$$

It is shown that the spatial frequency is approximately linearly proportional to the optical path length of the two fibre tapers. For the interferometers of the same interference length, the spatial frequency should be linearly proportional to the difference of the effective refractive indices between the core mode and different orders of cladding modes. For the interferometers of different interference lengths, the spatial frequency is mainly related to the large interference length difference not the trivial difference of the effective refractive indices. In Fig. 4-11(b) there are two main intensity peaks in the spatial frequency spectrum at the peak spatial frequencies of  $4.88$  and  $9.28 \text{ nm}^{-1}$ , respectively. These two peaks in the spatial frequency domain correspond to the interference lengths of  $2.5$  and  $5 \text{ cm}$ , respectively. The intensity at the first peak spatial frequency is much larger than the second one because mode coupling mainly occurs between the first and the second fibre tapers as well as the second and the third tapers with an interference length of  $L$ .

The second triple tapered fibre interferometer consists of three identical fibre tapers of Taper-2. A schematic illustration of the triple tapered fibre interferometer is shown in the inset of Fig. 4-12(b). The Taper-1 has a waist diameter  $D_0$  of  $90 \text{ }\mu\text{m}$  and the interval between two adjacent fibre tapers measures  $L = 2.5 \text{ cm}$ . Figure 4-12(a) shows the attenuation spectra of a fibre with only one single fibre taper, Taper-2, and the triple tapered fibre Mach-Zehnder interferometer of three Taper-2. The wavelength spectrum of the triple tapered FMZI in Fig. 4-12(a) is Fourier transformed to obtain the spatial frequency spectra of the interference fringes in Fig. 4-12(b).

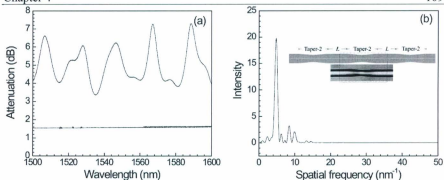


Figure 4-12: (a) Attenuation spectra of a single fibre taper and triple tapered fibre interferometer consisting of Taper-2. (b) Spatial frequency spectrum of the triple tapered fibre interferometer. Inset of (b) is a schematic illustration of the triple tapered fibre interferometer with an optical micrograph of Taper-2.

The fundamental mode propagating in the fibre core is coupled to high-order cladding modes at the taper region and the fibre taper angle with an expression of  $\arctan((D - D_0)/l_0)$  characterizes the fibre mode coupling efficiency and determines the change in the attenuation spectrum of the fibre taper [46]. Thus a thin fibre taper of Taper-1 with a small waist diameter has a greater mode coupling capability than a thick fibre taper of Taper-2. Compared with the attenuation spectra in Fig. 4-11(a), attenuations of the single and three fibre tapers decrease when fibre taper waist diameter increases. It is also indicated that a weak interference (smaller extinction ratio) from a triple tapered fibre interferometer consists of the thick fibre tapers will suffer a less attenuation simultaneously. The reason accounting for the weak interference is due to the fact that little energy is coupled to the cladding modes of forward propagation at the first fibre taper while most of the energy continues to stay in the core mode and hence less energy in

the cladding mode will return to the core mode at the second fibre taper to form the interference. In Fig. 4-12(b) there are three main intensity peaks in the spatial frequency spectrum at the peak spatial frequencies of  $4.82 \text{ nm}^{-1}$ ,  $8.42 \text{ nm}^{-1}$ , and  $9.95 \text{ nm}^{-1}$ , respectively. The first peak in the spatial frequency domain corresponds to the interference lengths of 2.5 cm. The second and the third peaks in the spatial frequency domain correspond to the interference lengths of 5 cm with lower and higher effective refractive index differences, respectively.

In the third triple tapered fibre interferometer, a fibre taper of Taper-1 are fabricated between two fibre tapers of Taper-2. A schematic illustration of the triple tapered fibre interferometer is shown in the inset of Fig. 4-13. The spacing between two adjacent fibre tapers is  $L = 2.5 \text{ cm}$ . The inset of Fig. 4-13 shows the attenuation spectra of the third triple tapered fibre Mach-Zehnder interferometer which has a wavelength spacing  $\Delta\lambda$  of 20 nm. It is indicated that the mode coupling only occurs between the middle thin fibre taper and the thick fibre tapers on the two sides due to the strong mode coupling within the middle fibre taper region. The spatial frequency spectra of the interference fringes in Fig. 4-13 is obtained by fast Fourier transformation of the wavelength spectrum of the triple tapered fibre Mach-Zehnder interferometer in the inset of Fig. 4-13. Only one dominant intensity peak at the peak spatial frequency of  $4.64 \text{ nm}^{-1}$  is found in the spatial frequency domain which corresponds to the interference lengths of 2.5 cm.

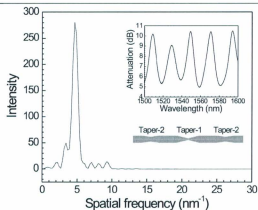


Figure 4-13: Spatial frequency spectrum of the triple fibre taper interferometer (Taper-2 + Taper-1 + Taper-2). Inset of (a) is the corresponding attenuation spectrum.

In the fourth triple tapered fibre interferometer, a fibre taper of Taper-2 are fabricated between two fibre tapers of Taper-1. A schematic illustration of the triple tapered fibre interferometer is shown in the inset of Fig. 4-14. The spacing between two adjacent fibre tapers is  $L = 2.5$  cm. The inset of Fig. 4-14 shows the attenuation spectra of the fourth triple tapered fibre Mach-Zehnder interferometer which has a wavelength spacing  $\Delta\lambda$  of 10 nm. The spatial frequency spectra of the interference fringes in Fig. 4-14 is obtained by fast Fourier transformation of the wavelength spectrum of the triple tapered fibre Mach-Zehnder interferometer in the inset of Fig. 4-14. Three intensity peaks at the peak spatial frequency of 4.46, 7.70, and 10.31  $\text{nm}^{-1}$  are observed in the spatial frequency domain. The first intensity peak corresponds to the interference lengths of 2.5 cm and the other two peaks in the spatial frequency domain correspond to the interference lengths of 5 cm with different effective refractive index differences. It is indicated that the mode

coupling between two thin fibre tapers dominates the fibre interference due to the weak mode coupling within the middle fibre taper region.

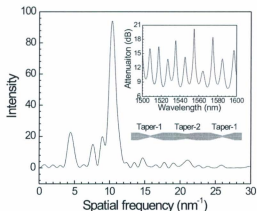


Figure 4-14: Spatial frequency spectrum of the triple fibre taper interferometer (Taper-1 + Taper-2 + Taper-1). Inset of (b) is the corresponding attenuation spectrum.

The fourth triple tapered fibre Mach-Zehnder interferometer with a structure of (Taper-1 + Taper-2 + Taper-1) was fixed at different temperatures controlled by a Sigma system with a temperature accuracy of 0.1 °C. In the temperature sensing measurement, the environmental temperature was increased from 20 °C to 100 °C. The corresponding attenuation peak wavelength shifts in the attenuation spectra is shown in Fig. 4-15. When the environmental temperature increases, the attenuation peak wavelengths at different orders exhibit different temperature sensitivities ranging from 50 to 58 pm/°C (redshifts), respectively.

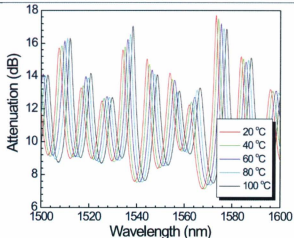


Figure 4-15: Attenuation spectrum of the triple fibre taper interferometer (Taper-1 + Taper-2 + Taper-1) at different temperature.

The corresponding spatial frequency spectra of the triple tapered fibre Mach-Zehnder interferometer at different temperatures are obtained by Fourier transformation of the attenuation spectrum shown in Fig. 4-16. Insets are the magnified regions at three intensity peaks, A at  $4.46$ , B at  $7.70$ , and C at  $10.31 \text{ nm}^{-1}$ , respectively. A corresponds to the interference lengths of  $2.5 \text{ cm}$ . B and C in the spatial frequency domain correspond to the interference lengths of  $5 \text{ cm}$  with lower and higher effective refractive index differences, respectively. The enlarged curves at A, B, and C indicate the redshifted spatial frequency spectra of the triple tapered fibre Mach-Zehnder interferometer with the increasing temperatures.

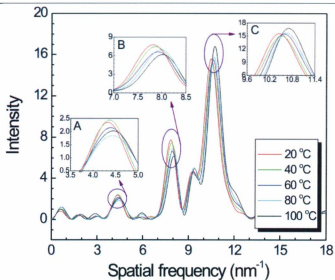


Figure 4-16: Spatial frequency spectrum at different temperatures. Insets are the magnified regions at three intensity peaks (A, B, and C).

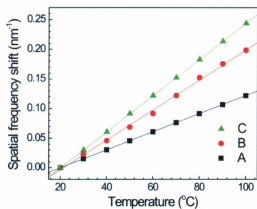


Figure 4-17: Dependence of the spatial frequency shift on temperature.

Figure 4-17 shows the dependences of the shifts in the spatial frequency of different intensity peak positions on the changes in the temperature. The temperature sensitivities for A, B, and C are 0.12, 0.20, and 0.24 nm<sup>-1</sup>/°C (redshifts), respectively. From Eqn. (4-10), the spatial frequency shift is related to the change in the optical path length. Thus a changing temperature will result in a difference of the effective refractive indices between the core and the cladding modes by thermal expansion and the thermo-optic effect and change the interferometer length by thermal expansion effect. The spatial frequency shift,  $\Delta \xi$ , induced by a temperature change  $\Delta T$  can be written as

$$\Delta \xi = \frac{1}{\lambda_0^2} \left( \frac{d\Delta n_{eff}}{dT} l + \frac{dl}{dT} \Delta n_{eff} \right) \Delta T \quad (4-13)$$

Comparing A with B and C, the great interferometer length difference between  $L$  and  $2L$  explains the difference in the temperature sensitivity. The difference in the effective refractive indices between the core and the cladding modes due to different cladding mode orders of B and C induces different temperature sensitivities. It is noted that a larger optical path length shows a larger shift in the peak spatial frequency than that of a smaller optical path length.

## **Chapter 5**

# **Microstructured Optical Fibre Fabricated by Femtosecond Laser**

### **5.1 Introduction**

The development of femtosecond lasers in the 1990s has initiated a new era of high-precision material processing and it has been gaining increasing popularity due to its unique 3D micromachining capabilities [1, 2]. Compared with conventional long pulsed lasers, a femtosecond laser has a pulse width about tens of femtoseconds. These pulses have extremely short pulse widths and ultra high peak intensity that allows highly efficient multiphoton nonlinear processing where several near-infrared photons are absorbed simultaneously. The mechanisms of femtosecond laser microfabrication can be categorized into two processes of energy absorption and energy dissipation [3-12]. In the

energy absorption process, a combination of multiphoton absorption and avalanche photoionization results in highly localized absorption of the femtosecond laser. Multiphoton absorption is a nonlinear process in which several photons are absorbed by a material simultaneously to excite an electron. Two conditions of the multiphoton ionization as a primary absorption process are that the material must have a band gap that is greater than the energy of a single photon and the laser must have a very high intensity. The intrinsic free conduction electrons and any electrons excited by multiphoton absorption serve as seed electrons for a second avalanche photoionization excitation process. Avalanche photoionization causes a rapid increase in the concentration of conduction electrons which linearly absorb photons. Once an electron has twice the band gap energy of the glass it is possible for the electron to collide with a second bound electron, exciting the second electron to the conduction band. Both electrons are then free to absorb more energy and continue the avalanche photoionization cycle. If enough energy is absorbed, the energy density will reach a critical threshold after which plasma forms within the exposed region. In the energy dissipation process, the energy dissipates through a combination of thermal diffusion and shock wave generation, and the end result is a localized material modification. Femtosecond laser with its unique advantages of minimal heat-affected areas possess the possibility to structurally modify regions of micrometer size inside almost any kind of optical fibre by nonlinear process.

Femtosecond lasers have been recently used to fabricate optical fibre interferometers. Reported work includes a fibre inline Fabry-Perot or Mach-Zehnder device with a microhole or microcavity fabricated by removing part of the fibre core and cladding by

femtosecond laser micromachining [13-18]. All these reported FMZIs usually involve highly demanding fabrication techniques, or the adoption of a fragile structure, which restrict their practical applications. In section 5.2, a femtosecond laser irradiated micro-spot is fabricated in a standard telecommunication single-mode fibre and a FMZI consisting of a femtosecond laser modified spot on a fibre taper is formed. Different gradients of the attenuation peak wavelengths of the interferometer on axial strain, temperature, and refractive index will be studied to demonstrate the effectiveness of the approach. The dependences of the sensitivities of different environmental parameters on the specifications of the interferometer are revealed. In section 5.3, a simplest and most compact FMZI on a single-mode optical fibre with femtosecond laser irradiations at 800 nm is experimentally achieved. The double femtosecond-laser-irradiated spots on the fibre core couple light from fundamental core mode to high-order cladding modes or vice versa to form an interferometer. The spots with changes in the refractive index induced by the femtosecond laser act as Mie scattering centres with adjustable sizes and determine the performance of the FMZI, such as attenuation loss, interference amplitude and scattering index factor, in which a spot of large radius results in a strong interference of high attenuation loss. As an application of this FMZI, measurement of axial strain and temperature will be investigated.

## 5.2 Femtosecond Laser Modified Spot

In this section, near-infrared femtosecond laser induced spots in a single-mode fibre as a

beam-steering element of fibre Mach-Zehnder interferometer will be studied. Figure 5-1 shows a schematic diagram of the femtosecond laser microfabrication system. An ultrafast Ti:sapphire regenerative amplifier (Libra-S, Coherent) operating at a wavelength of 800 nm with a repetition rate of 1 kHz and a pulse width of 67 fs was used. The laser beam with a beam diameter of 4 mm was irradiated on an optical fibre mounted on two linear translation stages. The XYZ stages (ATS100, Aerotech Inc.) were controlled by a motion controller (UNIDEX511, Aerotech Inc.) through a general purpose interface bus system (GPIB) interface system and LabVIEW™ programming control. Laser pulse energy of 15  $\mu\text{J}$  with laser irradiation time of 10 s was adopted in the microfabrication. A CCD camera in conjunction with a beam splitter (BS) was used to monitor the fibre alignment and the in-situ laser micromachining process.

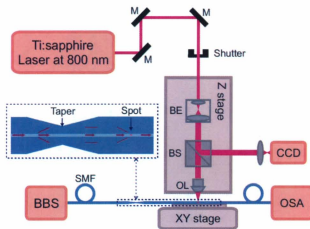


Figure 5-1: Schematic illustration of the femtosecond laser microfabrication system. M, mirror; BE, beam expander (magnification, 2 $\times$ ); BS, beam splitter; OL, objective lens (magnification 50 $\times$ , NA 0.80). Inset is a scheme of the fibre interferometer.

Electrical arc method was adopted to fabricate an abrupt taper on a standard single-mode optical fibre (SMF-28e, Corning Inc.) using a FITELE S182A fusion splicer. The left inset of Fig. 5-2 shows the tapered fibre with a waist diameter  $D_0$  of  $60\ \mu\text{m}$  and a taper length  $l_0$  of  $600\ \mu\text{m}$ . After the taper fabrication, the femtosecond laser beam was focused on the centre of the fibre core, which was  $30\ \text{mm}$  away from the centre of the fibre taper. The cylindrical fibre cladding, which acts as a cylindrical lens, converges the Gaussian beam in a direction perpendicular to the fibre axis without convergence effect along the fibre axis. Thus the focused Gaussian beam of a  $20\ \mu\text{m}$  in diameter was focused to be a spindle-shaped spot of  $20\ \mu\text{m} \times 4\ \mu\text{m}$ , which is shown as the dark area in the centre of the fibre in the right inset of Fig. 5-2. The attenuation spectrum of the femtosecond laser trimmed fibre taper was measured by an optical spectrum analyzer (Ando 6315E) with an erbium broadband light source (EBS-7210, MPB Communications, Inc.).

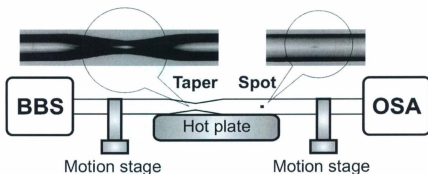


Figure 5-2: Schematic illustration of the experimental setup for sensing test. Insets are optical micrographs of a fibre taper and a femtosecond laser trimmed spot.

Figure 5-3 shows the attenuation spectra of a fibre with a single femtosecond laser irradiated spot only, a single fibre taper only, and a femtosecond laser trimmed fibre taper. According to Marcuse's equation,  $w/a \approx 0.65 + 1.619/V^{3/2} + 2.879/V^6$  [19], the mode field radius  $w$  of a single-mode fibre with a fibre core radius  $a$  has a larger value for a longer wavelength due to the decreased normalized frequency  $V$  with the increasing wavelength. The fundamental mode propagating in the fibre core is coupled to high-order cladding modes when the fibre narrows. Thus more energy will be coupled to the fibre cladding at longer wavelengths and a larger attenuation is resulted, i.e., 2.97 dB at 1500 nm and 3.15 dB at 1600 nm (Fig. 5-3), respectively. The infrared femtosecond laser with an intensity of  $10^{15}$  W/cm<sup>2</sup> focused inside the fibre core induces a refractive index change due to a type II-IR process of material ionization and resolidification [20]. The femtosecond laser trimmed spot in the optical fibre can be regarded as a Mie scattering centre where the fundamental core mode will be scattered into higher order cladding modes. All wavelengths of light are scattered in both the backward and forward scattering directions while a wavelength dependence exists [21]. Consequently, the attenuation loss at a longer wavelength is lower than that at the shorter wavelength (1.717 dB at 1500 nm and 1.658 dB at 1600 nm), as shown in Fig. 5-3. The inset of Fig. 5-1 shows a scheme of the fibre interferometer consisting of the taper and the femtosecond laser microfabricated spot. In a femtosecond laser trimmed fibre taper, part of the light energy in the fibre core will be coupled into the cladding after passing through the fibre taper and the femtosecond laser trimmed spot will couple most of the cladding mode energy back from the cladding into the core after passing through the fibre segment between them, in which part of the

energy is attenuated during the cladding mode propagation. The mechanism of light propagation in this femtosecond laser trimmed fibre taper is exactly a FMZI, for which the attenuation peak wavelength  $\lambda_m$  can be expressed as  $\lambda_m = 2\Delta n_{\text{eff}}L/(2m+1)$ , where  $\Delta n_{\text{eff}}$  is the difference of the effective refractive indices between the core and the cladding modes,  $L$  is the length of the interferometer or the distance between the two microstructures, and  $m$  is the order of interference. Figure 5-3 shows the interference spectrum of the attenuation for this femtosecond laser trimmed fibre taper with an interferometer length of 30 mm. The FMZI has an extinction ratio of 1.2 dB and an attenuation of 5.4 dB with a wavelength spacing of 16.7 nm at 1543.6 nm.

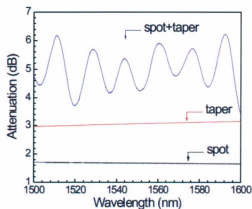


Figure 5-3: Attenuation spectra of a fibre with a single femtosecond laser trimmed spot, a single fibre taper, and a FMZI consisting of a fibre taper and a femtosecond laser trimmed spot spaced 30 mm apart.

A schematic illustration of the experimental setup used for the measurement of axial strain and temperature is shown in Fig. 5-2. For the measurement of the axial strain ( $\epsilon$ )

and temperature ( $T$ ) with the fibre interferometer developed in this study, the optical fibre was axially stretched at different temperatures controlled by a hot plate with a temperature accuracy of  $0.1\text{ }^{\circ}\text{C}$ . The fibre was fixed on two translation stages (ATS100, Aerotech) using epoxy glue and the length of the fibre segment containing the 30 mm-long fibre interferometer between the two fixed points was 500 mm. The axial strain was adjusted by the translation stages with a motion accuracy of  $0.5\text{ }\mu\text{m}$ . The environmental temperature was firstly changed without strain applied on the fibre interferometer and the corresponding attenuation spectrum shift is shown in Fig. 5-4(a).

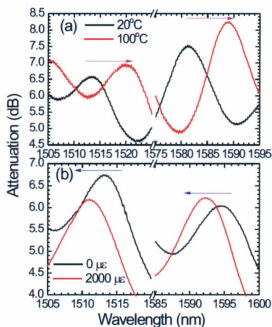


Figure 5-4: Shifts in the attenuation spectra of the FMZI at (a) temperature of  $20\text{ }^{\circ}\text{C}$  and  $100\text{ }^{\circ}\text{C}$ , (b) axial strain of 0 and  $2000\text{ }\mu\epsilon$ .

An attenuation peak wavelength of 1513.4 nm at an interference order  $m_1$  of 95 shifts to 1519.9 nm and a peak wavelength of 1581.2 nm at an order  $m_2$  of 90 shifts to 1589.1 nm when the temperature increases from 20 °C to 100 °C. The shift of the attenuation peak wavelength,  $\delta\lambda_{m,T}$ , due to the temperature increase can be expressed as

$$\delta\lambda_{m,T} = \frac{2(\Delta n_{\text{eff},T} + \delta n_{\text{eff},T})L}{2m+1} - \frac{2\Delta n_{\text{eff},T}L}{2m+1} = \frac{2\delta n_{\text{eff},T}L}{2m+1} \quad (5-1)$$

where  $\delta n_{\text{eff},T}$  is the increased difference in the effective refractive indices induced by the increase of the environmental temperature. It is obvious that the attenuation peak wavelength will exhibit a redshift as the environmental temperature increases. When an appropriate axial strain from 0 to 2000  $\mu\epsilon$  was applied on the FMZI kept at a constant temperature of 20 °C, the attenuation peak wavelength of 1513.0 nm at the order  $m_1$  shifts to 1511.0 nm and the peak wavelength of 1595.7 nm at the order  $m_2$  shifts to 1593.3 nm, which is shown in Fig. 5-4(b). The shift in the attenuation peak wavelength  $\delta\lambda_{m,\epsilon}$ , due to the change in axial strain, can be expressed as:

$$\delta\lambda_{m,\epsilon} = \frac{2(\Delta n_{\text{eff},\epsilon} - \delta n_{\text{eff},\epsilon})(L + \delta L)}{2m+1} - \frac{2\Delta n_{\text{eff},\epsilon}L}{2m+1} \approx \frac{2(\Delta n_{\text{eff},\epsilon}\delta L - L\delta n_{\text{eff},\epsilon})}{2m+1} \quad (5-2)$$

where  $\delta L$  is the change in the interferometer length between the taper and the spot, and  $\delta n_{\text{eff},\epsilon}$  is the change in the effective refractive index due to the increase of the external axial strain. The increase in the fibre length due to axial strain and the accompanying decreases in the radii of the fibre core and cladding result in a decrease in the normalized frequency  $V$  and consequently a decrease in the difference of the effective refractive indices between the core and the cladding modes. The increase in the interferometer length has a weaker impact on the peak wavelength shift than the influence of a decrease

in the difference of the effective refractive indices so that the attenuation peak wavelength

will blue-shift when the axial strain increases.

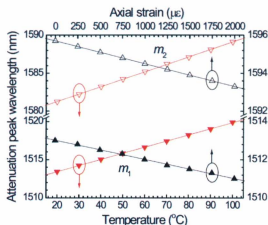


Figure 5-5: Dependences of the shifts in the attenuation peak wavelengths of the FMZI at two interference orders of  $m_1$  and  $m_2$  on temperature and axial strain.

Figure 5-5 shows the dependences of the shifts in the peak wavelengths of the orders  $m_1$  and  $m_2$  on the changes in the axial strain and temperature. The temperature sensitivities at the order  $m_1$  and  $m_2$  are 81.3 and 98.8 pm/°C (redshift) while the corresponding strain sensitivities are -1.0 and -1.2 pm/με (blueshift), respectively. The experimental results show that the peak wavelength of a larger interference order exhibits a larger shift under the same amount of change in the environmental parameter. According to Eqs. (5-1) and (5-2), it can be found that different interference orders exhibit different gradients of the attenuation peak wavelength on axial strain and temperature. Therefore, a character matrix  $M_{eT}$  is defined to represent the sensing performance of the femtosecond laser trimmed fibre taper:

$$\begin{bmatrix} \Delta\lambda_{m1} \\ \Delta\lambda_{m2} \end{bmatrix} = M_{\varepsilon,T} \begin{bmatrix} \Delta T \\ \Delta\varepsilon \end{bmatrix} = \begin{bmatrix} 81.3 & -1.0 \\ 98.8 & -1.2 \end{bmatrix} \begin{bmatrix} \Delta T \\ \Delta\varepsilon \end{bmatrix}, \quad (5-3)$$

which is equivalent to the following equation through a matrix transposition:

$$\begin{bmatrix} \Delta T \\ \Delta\varepsilon \end{bmatrix} = M_{\varepsilon,T}^{-1} \begin{bmatrix} \Delta\lambda_{m1} \\ \Delta\lambda_{m2} \end{bmatrix}, \quad (5-4)$$

The character matrix  $M_{\varepsilon,T}$  can be used to simultaneously determine the variations in the axial strain and temperature from the shifts of the attenuation peak wavelengths of any two arbitrarily selected interference orders.

Precise refractive index measurement is extremely important in many applications such as chemical or food industries, environmental monitoring, and biosensing. Therefore in order to obtain an accurate value of the refractive index, temperature effect should not be neglected because it is well known that the refractive index of solution has a strong dependence on temperature. In the next part, an optical fibre sensor consisting of a fibre taper made by a fusion splicer and a femtosecond laser irradiated spot is fabricated to measure external refractive index while achieving temperature compensation. An abrupt taper with a waist diameter of 65  $\mu\text{m}$  and a taper length of 625  $\mu\text{m}$  was first fabricated by tapering a single-mode fibre SMF-28e using a FITELE S182A fusion splicer as shown in the right figure of Fig. 5-6. The incident Gaussian beam of 20  $\mu\text{m}$  in diameter was focused to a spindle-shaped spot of 20  $\mu\text{m} \times 4 \mu\text{m}$  (left figure of Fig. 5-6) due to the beam convergence in the radial direction and nonconvergence in the axial direction by the cylindrical fibre cladding. The distance between the fibre taper and the femtosecond laser irradiated spot was 10 mm.

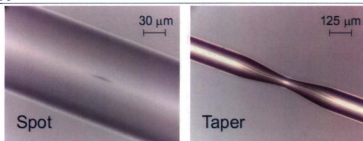


Figure 5-6: Top views of a femtosecond laser microfabricated spot (left) and a fibre taper made by a fusion splicer (right).

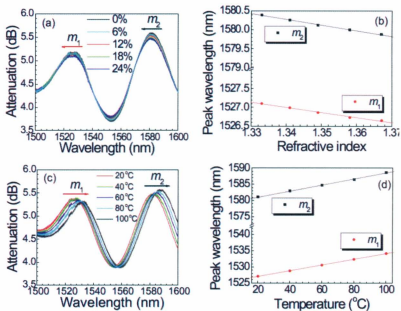


Figure 5-7: Attenuation spectra of the FMZI at different (a) KCl solution concentrations and (c) temperatures. Dependences of the shifts in the attenuation peak wavelengths of the FMZI on (b) environmental refractive index and (d) temperature of different interference orders.

Figures 5-7(a) and (c) show the attenuation spectra of the FMZI, in which an extinction ratio of ~2 dB and a wavelength spacing of 55 nm can be found between the two interference orders  $m_1$  of 28 and  $m_2$  of 27 at attenuation peak wavelengths of 1526 and 1581 nm, respectively. The relationship between the attenuation peak wavelength of the FMZI and the environmental refractive index ( $RI$ ) was investigated using KCl solution while the temperature of the solution was maintained at  $20.0 \pm 0.1$  °C. The shift in the attenuation peak wavelength  $\delta\lambda_{m,RI}$  of the FMZI due to the change in the environmental refractive index can be expressed as

$$\delta\lambda_{m,RI} = \frac{2(\Delta n_{\text{eff},RI} - \delta n_{\text{eff},RI})L}{2m+1} - \frac{2\Delta n_{\text{eff},RI}L}{2m+1} = \frac{-2\delta n_{\text{eff},RI}L}{2m+1}, \quad (5-5)$$

Thus the attenuation peak wavelength  $\lambda_{m,RI}$  will shift to a shorter wavelength  $\lambda_{m,RI}'$  by an amount of  $\delta\lambda_{m,RI}$ . Figure 5-7(a) shows the attenuation spectra of the FMZI at different concentrations of KCl solution. Figure 5-7(b) shows the dependences of the shifts in the peak wavelengths of the orders  $m_1$  and  $m_2$  on the changes in the refractive index. The refractive index sensitivities for  $m_1$  and  $m_2$  are  $-13.235$  and  $-15.294$  nm/RIU (blueshift), respectively. In order to obtain an accurate refractive index by taking into consideration of the temperature effect, dependences of the changes in the attenuation peak wavelengths of the two interference orders on temperature were also investigated to resolve the inherent cross-sensitivity effects of the FMZI between refractive index and temperature. For the temperature ( $T$ ) sensitivity measurement, the FMZI was placed in a water bath with a temperature accuracy of  $0.1$  °C. The shift of the attenuation peak wavelength,  $\delta\lambda_{m,T}$ , due to the temperature increase can be expressed as  $\delta\lambda_{m,T} = 2\delta n_{\text{eff},T}L/(2m+1)$ . The attenuation

peak wavelength exhibits a redshift when the environmental temperature increases.

Figure 5-7(c) shows the attenuation spectra of the FMZI at different temperatures. Figure 5-7(d) shows the dependences of the shifts in the peak wavelengths of the orders  $m_1$  and  $m_2$  on temperature. The temperature sensitivities for  $m_1$  and  $m_2$  are 0.089 and 0.094 nm/ $^{\circ}$ C (redshift), respectively.

Since different interference orders have different gradients of the peak wavelength on refractive index and temperature, a character matrix  $M_{RI,T}$  is defined to represent the sensing performance of the FMZI,

$$\begin{bmatrix} \Delta\lambda_{m1} \\ \Delta\lambda_{m2} \end{bmatrix} = M_{RI,T} \begin{bmatrix} \Delta RI \\ \Delta T \end{bmatrix} = \begin{bmatrix} -13.235 & 0.089 \\ -15.294 & 0.094 \end{bmatrix} \begin{bmatrix} \Delta RI \\ \Delta T \end{bmatrix} \quad (5-6)$$

In this case once the character matrix is obtained through calibration, measurement of refractive index with temperature compensation can be achieved.

The distance between the femtosecond laser inscribed spot and the fusion spliced fibre taper of the fibre Mach-Zehnder interferometer plays an important role to determine its transmission spectrum. In order to investigate the effects of the structure specifications of the interferometer on the sensing performance, several FMZI of different interference length will be fabricated. Their temperature, axial strain, and refractive index sensitivities will be analyzed in the following part. An abrupt tapered fibre was sharpened to a waist diameter  $D_0$  of 55  $\mu$ m with a taper length  $l_0$  of 625  $\mu$ m. A femtosecond laser beam induced 4  $\mu$ m  $\times$  20  $\mu$ m elliptical spot was then focused on the centre of the fibre core, which was 10 mm away from the fibre taper. The two curves in Fig. 5-8(a) correspond to the attenuation spectra of a fibre with an ultrafast laser irradiated single spot only and a

fibre with an electrical arc fabricated single taper only, respectively.

Figure 5-8(b) shows the interference spectrum of the attenuation for a 10-mm-long fibre interferometer at different environmental parameters. The temperature ( $T$ ) effect was evaluated by changing the environmental temperature from 20 °C to 100 °C, controlled by a Sigma system with an accuracy of 0.1 °C. The axial strain ( $\epsilon$ ) response of the fibre interferometer was tested by fixing the fibre on two linear translation stages (ATS100, Aerotech) with a motion accuracy of 0.5  $\mu\text{m}$  using epoxy glue and then axially stretched with a strain from 0 to 2000  $\mu\epsilon$  at a constant temperature of 20 °C. The refractive index ( $RI$ ) sensing measurement was conducted using KCl solution of different concentrations when the temperatures of the solutions are maintained at 20.0 °C and no strain is applied on the fibre. The experimental results in Fig. 5-8(b) indicate that the attenuation peak wavelength exhibits a redshift as the environmental temperature increases and a blueshift as the axial strain or the KCl concentration increases. The sensitivities of temperature, axial strain, and refractive index for the 10-mm-long fibre interferometer at a wavelength of 1580 nm are 0.095 nm/°C,  $-1.15$  pm/ $\mu\epsilon$ ,  $-14.706$  nm/RIU, respectively. The shifts in the attenuation peak wavelengths depend on both the changes of the differences in the effective refractive indices between the core and higher order cladding modes and the waveguide dispersion of different cladding modes [22]. However, the experimental results indicated that the mode coupling mainly occurred between only one of the cladding modes and the core mode through the fibre taper and the spot, thus dispersion effect in this case is not pronounced. When the environmental temperature rises, the effective refractive index of the core mode increases more than that of the cladding mode since the

thermo-optic coefficient of the Ge-doped silica core,  $8.6 \times 10^{-6} \text{ } ^\circ\text{C}^{-1}$ , is higher than that of the cladding consisting of fused silica,  $7.8 \times 10^{-6} \text{ } ^\circ\text{C}^{-1}$  [22, 23]. Thus the attenuation peak wavelength will move to a longer wavelength with the increasing temperature. As the environmental refractive index increases, the effective refractive index difference will decrease because the effective refractive index of the cladding mode increases and that of the core mode is unaltered. Therefore the attenuation peak wavelength will shift to a shorter wavelength with the increasing external refractive index. The elongation in the fibre length and reduction in the radius of the fibre core result in a decrease in the normalized frequency and consequently a decrease in the difference of the effective refractive indices between the core and the cladding modes. The increase in the interferometer length has a weaker impact than the influence of a decrease in the difference of the effective refractive indices so that the attenuation peak wavelength will blueshift when the axial strain increases.

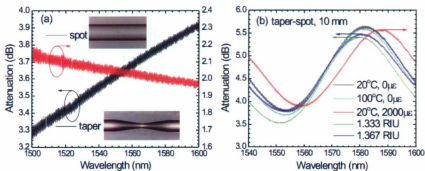


Figure 5-8: (a) Attenuation spectra of a fibre with a taper only and of a fibre with an ultrafast laser microfabricated spot only. Insets are the optical micrographs of a taper and a spot, respectively. (b)

Attenuation spectra of a 10-mm-long fibre interferometer consisting of the taper and the spot at different environmental conditions (temperature, axial strain, and environmental refractive index).

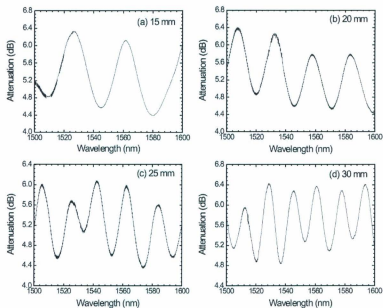


Figure 5-9: Attenuation spectra of fibre interferometers consisting of a taper and a femtosecond laser microfabricated spot with a spatial separation of (a) 15 mm, (b) 20 mm, (c) 25 mm, and (d) 30 mm, respectively.

It is also noted that selection of the attenuation peak wavelength for monitoring determines the gradients of the shifts of the attenuation peak wavelength on sensing parameters. Four interferometers consisting of a fibre taper and an ultrafast laser microfabricated spot of the same size as the spot in the aforementioned 10-mm-long fibre interferometer were fabricated with different interferometer lengths ranging from 15 to 30 mm. The attenuation spectra of these fibre interferometers are shown in Fig. 5-9. Figure 5-9 indicates that the wavelength spacing is inversely proportional to the distance

between the fibre taper and the ultrafast laser microfabricated spot, for instance, wavelength spacings of 35.5, 25.4, 20.5, and 16.7 nm can be found for fibre interferometers of 15, 20, 25, and 30 mm in length, respectively.

The sensing characteristics of these fibre interferometers with the dependences of the shifts in the attenuation peak wavelengths on temperature, axial strain, and refractive index are shown in Fig. 5-10(a), (b), and (c), respectively. Figure 5-10(d) shows the temperature, axial strain, and refractive index sensitivities measured at certain attenuation peak wavelengths.

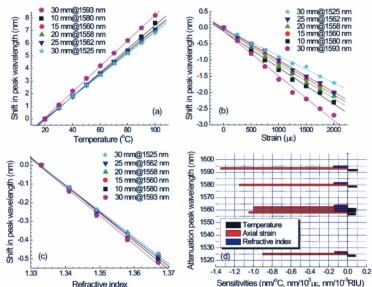


Figure 5-10: Dependences of the shifts in the attenuation peak wavelengths of different fibre interferometers on (a) temperature, (b) axial strain, and (c) refractive index, respectively. (d) Temperature, axial strain, and refractive index sensitivities measured at certain attenuation peak wavelengths.

For the same type of fibre interferometer of 30 mm in length, if the operation wavelength is selected at 1593 nm, the corresponding sensitivities are 0.103 nm/°C, -1.35 pm/με, and -15.294 nm/RIU, respectively. If the operation wavelength is selected at 1525 nm, the sensitivities become 0.085 nm/°C, -0.09 pm/με, and -13.824 nm/RIU, respectively. For the 15-, 20-, and 25-mm-long fibre interferometers at the selected operation wavelengths close to 1560 nm, the average sensitivities are 0.087 nm/°C, -1.02 pm/με, and -14.217 nm/RIU. The experimental results show that a longer attenuation peak wavelength exhibits a larger shift under the same amount of change in the environmental parameter than that at a shorter wavelength.

### 5.3 Femtosecond Laser Inscribed Fibre Interferometer

In this section, a micro-fibre Mach-Zehnder interferometer is achieved through two beam-steering spots fabricated by near-infrared femtosecond laser irradiation at 800 nm. Compared with other fibre interferometer fabrication techniques, only two micro spots inside a single-mode fibre are necessary to form a specification-tunable FMZI. The sizes of the spots, which determine the performance of the fibre interferometer, can be easily adjusted by using different objective lenses in the femtosecond laser microfabrication system. Dependences of the attenuation loss, interference amplitude and scattering index factor  $\eta$  on the spot size as well as the refractive index change will be analyzed.

The femtosecond pulses was irradiated on a standard single-mode telecommunication fibre (SMF-28e, Corning Inc.) mounted on a XY translation stage through three steering

mirrors (M) as well as a beam expander (BE, magnification  $2\times$ ) and a focusing objective lens (OL) mounted on a Z translation stage. Laser pulse energy of  $20\ \mu\text{J}$  and irradiation duration of  $6\ \text{s}$  were adopted in the femtosecond laser microfabrication. The attenuation spectrum of the FMZI was measured by the optical spectrum analyzer with a white light source (Ando AQ4303B). The protective plastic coating on the fibre over a segment of  $3\ \text{cm}$  in length was stripped off before the laser irradiation.

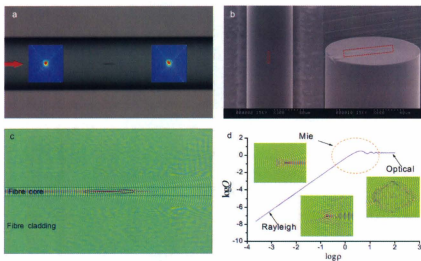


Figure 5-11: (a) An optical micrograph of a femtosecond-laser-irradiated single-mode optical fibre (top-view). Left and right insets are the near-field profiles of the single-mode fibre without and with a femtosecond-laser-irradiated spot. (b) SEM images of the femtosecond-laser-irradiated single-mode optical fibre without polymeric coating (left, top-view; and right, cross-section). (c) Two-dimensional finite element simulation on the distribution of light energy density along the femtosecond-laser-irradiated spot. (d) Dependence of the scattering efficiency factor  $Q$  on the scattering sphere quality factor  $\rho$ . Inset are simulated scattered fields by scattering spheres with different radii.

Figure 5-11(a) shows an optical micrograph of a single spot on the fibre core fabricated by femtosecond laser irradiation using a 50 $\times$  objective lens (NA 0.80). Two insets in Fig. 5-11(a) depict the observed near-field profiles of the outputs from the fibre without and with the spot, which exhibit a single mode to multimode conversion process. It is interesting to note that the femtosecond laser irradiation induces an increase in the refractive index inside the fibre without morphological changes on the fibre surface, which is evident from the observation with a scanning electron microscope (Hitachi S-570) shown in Fig. 5-11(b). The femtosecond laser modification region has the comparable size with the input light wavelength so that it could be approximately considered as a Mie scattering center which can induce fibre mode coupling. In order to verify the incident light propagation and the coupling effect, a two-dimensional finite element analysis has been adopted to simulate a laser-irradiated-spot on a single-mode fibre with the results presented in Fig. 5-11(c), indicating that the energy of LP<sub>01</sub> in fibre core mode will be partly coupled to high-order LP<sub>0n</sub> cladding modes after passing through the spot.

Assuming the refractive index of the core in a standard single-mode optical fibre is  $n_0$ , the irradiation of a focused femtosecond laser onto the fused-silica fibre core with a 3 mol% germanium-doping induces structural changes accompanied by an increased refractive index  $\Delta n$  inside the fibre [24]. The femtosecond-laser-irradiated spot can be regarded as a scattering sphere of refractive index  $(n_0 + \Delta n)$  and radius  $r$ . The relative refractive index  $m$  is defined as  $m = (n_0 + \Delta n)/n_0$  and the relative sphere size  $x$  is given by  $x = 2\pi r n_0/\lambda$ . The extinction coefficient,  $\gamma$ , is expressed as  $\gamma = \pi r^2 Q$ , where  $Q$  is the

scattering efficiency factor with an expression of  $Q = 2 - 4\sin\rho/\rho + 4(1 - \cos\rho)/\rho^2$ , where  $\rho = 2x(m - 1)$  is the scattering sphere quality factor [21]. Figure 5-11(d) shows the simulation of the scattering efficiency factor  $Q$  as a function of  $\rho$ . The evolution of the curve  $\log Q$  versus  $\log \rho$  includes three segments. If  $\rho$  is very small,  $Q$  falls into Rayleigh scattering region. A curve fitting shows a linear relation of  $\log Q = c_0 + \eta \log \rho$  or  $Q = c_0 \rho^\eta$  with the value of the scattering index factor  $\eta$  approximated to be 2. In the next Mie scattering zone,  $\rho$  values range between 1 and 10, and  $Q$  continues to follow a  $\rho^\eta$  dependence, where the dependence of the scattering index factor  $\eta$  on the scattering sphere quality factor  $\rho$  or the slope of the curve are between 2 and -2. The value of  $Q$  oscillates and approaches a limitation of 2 in the Mie scattering zone, followed by entering the geometrical optical zone as the value of  $\rho$  increases from 10. The insets in Fig. 5-11(d) are simulated scattered fields by scattering spheres with different radii in the regions of Rayleigh scattering, Mie scattering, and geometrical optical zone, accordingly.

In the Mie scattering zone, the scattering efficiency factor,  $Q$ , can be expressed as

$$Q = c_0 \rho^\eta = c_0 [2x(m-1)]^\eta = c_2 (r \Delta n \lambda^{-1})^\eta. \quad (5-7)$$

From Eqn. (5-7), the extinction coefficient  $\gamma$  will take a form of  $\gamma = c_0 (\Delta n)^2 r^{2+\eta} \lambda^{-\eta}$ .

The propagation intensity  $I_0$  will decrease along a distance  $L$  to  $I_1$  by a fraction of  $e^{-\gamma L}$ . The attenuation coefficient due to the scattering centre can be expressed as

$$\alpha = -10 \log \left( \frac{I_1}{I_0} \right) = -10 \log (e^{-\gamma L}) = 10 \gamma L \log e = c_4 (\Delta n)^\eta r^{2+\eta} \lambda^{-\eta}. \quad (5-8)$$

Figure 5-12 shows the attenuation spectra of six FMZIs fabricated with different specifications, i.e., varying magnification of the objective lens and irradiation time.

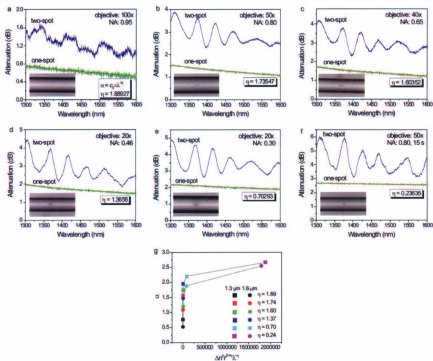


Figure 5-12: Attenuation spectra of FMZIs fabricated with femtosecond laser pulse energy of 20  $\mu\text{J}$  and irradiation duration of 6 s under different objective lenses: (a) 100 $\times$  (NA 0.95), (b) 50 $\times$  (NA 0.80), (c) 40 $\times$  (NA 0.65), (d) 20 $\times$  (NA 0.46), and (e) 20 $\times$  (NA 0.30). (f) shows the attenuation spectra of the FMZI fabricated with a 50 $\times$  objective lens (NA 0.80) and laser irradiation duration of 15 s. The insets are optical micrographs of the femtosecond laser irradiated spots (top-view). (g) shows the relations between the attenuation coefficient  $\alpha$  and refractive index change  $\Delta n$ , radius  $r$ , wavelength  $\lambda$ , at different values of the scattering index factor  $\eta$ .

After the femtosecond laser is irradiated on the coating-removed fibre core, through an objective lens of 100 $\times$  (NA 0.95), the attenuation spectrum of the fibre with a single spot is shown in Fig. 5-12(a). The attenuation of 0.76 dB at a wavelength of 1300 nm

decreases to 0.52 dB at 1600 nm with an attenuation difference of 0.24 dB, which agrees with Eqn. (5-8) that a smaller attenuation  $\alpha$  can be found at a longer wavelength. Curve fitting of the single-spot attenuation spectrum in Fig. 5-12(a) indicates that  $\eta = 1.89$ . When a second spot of the same geometry is fabricated with a spatial separation of 10 mm from the first one, a FMZI is formed. Part of the light energy in the fibre core will be coupled into the cladding through the first spot due to the Mie scattering while the second spot will couple part of the cladding mode energy back into the core after passing through the fibre segment between the two spots, through which part of the energy is attenuated during the cladding mode propagation. Plateaus at the attenuation peaks with small interference amplitude have been observed for the fibre interferometer with the 100 $\times$  objective lens. The reason accounting for the weak interference is due to the fact that little energy is coupled to the cladding modes of forward propagation at the first scattering spot while most of the energy continues to stay in the core mode and hence less energy in the cladding mode will return to the core mode at the second spot to form the interference.

When the femtosecond laser is irradiated on the coating-stripped fibre core through a 50 $\times$  (NA 0.80) objective lens, a first spot is made with an attenuation spectrum of the fibre shown in Fig. 5-12(b). The attenuation of 1.54 dB at a wavelength of 1300 nm decreases to 1.08 dB at 1600 nm with an attenuation difference of 0.46 dB. Curve fitting of the attenuation spectrum of the fibre with the single-spot in Fig. 5-12(b) indicates that  $\eta = 1.74$ . When a second femtosecond-laser-irradiated spot is made on the fibre core with a spatial separation of 10 mm from the first spot, the wavelength spacing,  $\Delta\lambda_m$ , is 51.3 nm between the two attenuation peak wavelengths of the interferometer at 1371.1 and 1422.4

nm and the interference amplitude is 1.07 dB between the attenuation peak wavelengths at 1397.8 and 1422.4 nm. At the attenuation peak wavelengths, the phase difference  $\Phi$  between the core mode and the cladding mode satisfies the condition of  $\Phi = 2\pi\Delta n_{\text{eff}}L/\lambda$ , where  $\Delta n_{\text{eff}}$  is the effective refractive index difference between the core and the cladding modes and  $L$  is the distance between the two spots. From the equation of the wavelength spacing between the adjacent attenuation peak wavelengths  $\Delta\lambda_m = \lambda_{m-1} - \lambda_m = \lambda^2/\Delta n_{\text{eff}}L$ ,  $\Delta n_{\text{eff}}$  is calculated to be 0.004, which is consistent with the refractive index difference of the core and cladding of the SMF-28e fibre, specified as 0.005 by the manufacturer [25].

Figure 5-12(c), (d), and (e) show three attenuation spectra of the FMZIs fabricated using objective lenses of 40 $\times$  (NA 0.65), 20 $\times$  (NA 0.46), and 20 $\times$  (NA 0.30), respectively, while Fig. 5-12(f) shows the attenuation spectra of an interferometer made with a 50 $\times$  (NA 0.80) objective lens for a longer laser irradiation time of 15 seconds. The insets of Fig. 5-12 show optical micrographs of the spots on the fibre core fabricated by femtosecond laser irradiation with these different fabrication parameters. Spots with radii of 1.5, 2.0, 3.0, 7.0, and 8.5  $\mu\text{m}$  were fabricated with objective lenses of decreasing magnifications and NA values from 100 $\times$  (NA 0.95), 50 $\times$  (NA 0.80), 40 $\times$  (NA 0.65), 20 $\times$  (NA 0.46) to 20 $\times$  (NA 0.30). For these femtosecond laser irradiated spots in the fibre core, the induced increase in the refractive index  $\Delta n$  was estimated to range from  $3.3 \times 10^{-4}$  to  $1.0 \times 10^{-5}$ , according to Ref. [24]. For a spot with a radius of 3.5  $\mu\text{m}$  fabricated with an objective lens of 50 $\times$  (NA 0.80) and laser irradiation time of 15 seconds, the induced increase in the refractive index  $\Delta n$  is calculated to be  $1.5 \times 10^{-4}$ . The properties of different FMZIs fabricated with different specifications are listed in Table 5-1 for comparison.

Table 5-1 indicates that a strong interference (larger extinction ratio) from a double-spot FMZI fabricated with an objective lens of a smaller NA will suffer a larger attenuation simultaneously. Figure 5-12(g) indicates that the increased radius of the laser-irradiated-spot  $r$  and the increased change in the refractive index with the increasing magnification or NA of the objective lens as well as the laser irradiation time will increase the attenuation and decrease the factor  $\eta$ . Compared with the Mie scattering zone in Fig. 5-11(d), the wavelength dependences of the attenuation coefficient and factor  $\eta$  in Fig. 5-12(g) show a good agreement, indicating that a smaller scattering sphere quality factor  $\rho$  corresponds to a larger positive scattering index factor  $\eta$ .

Table 5-1 Comparison of the performance of different FMZIs fabricated in this study.

Objective lens Magnification (numerical aperture)	Attenuation (dB)		Extinction ratio (dB)	$\eta$	$r$ ( $\mu\text{m}$ )	$\Delta n$
	@1.3 $\mu\text{m}$	@1.6 $\mu\text{m}$				
100 $\times$ (NA 0.95)	0.76	0.52	0.32	1.89	1.5	$3.3 \times 10^{-4}$
50 $\times$ (NA 0.80)	1.54	1.08	1.07	1.74	2.0	$1.9 \times 10^{-4}$
40 $\times$ (NA 0.65)	1.75	1.20	1.26	1.60	3.0	$8.3 \times 10^{-5}$
20 $\times$ (NA 0.46)	1.95	1.47	1.29	1.37	7.0	$1.5 \times 10^{-5}$
20 $\times$ (NA 0.30)	2.20	1.88	1.99	0.70	8.5	$1.0 \times 10^{-5}$
50 $\times$ (NA 0.80) (15 seconds)	2.66	2.54	2.79	0.24	3.5	$1.5 \times 10^{-4}$

Mode coupling in single-mode fibre maybe caused by many fibre irregularities, such as bending, refractive index change, and core/cladding interface deformation. Since the femtosecond laser written spots are not necessarily spherical and that this is incorporated in an optical fibre, and the small refractive index difference exists between the original and modified regions, usage of Mie scattering theory here has its limitations. Therefore,

further investigation of explaining mode transitions by considering the coupled-mode theory which has been widely adopted in analysis of fibre Bragg gratings is desirable.

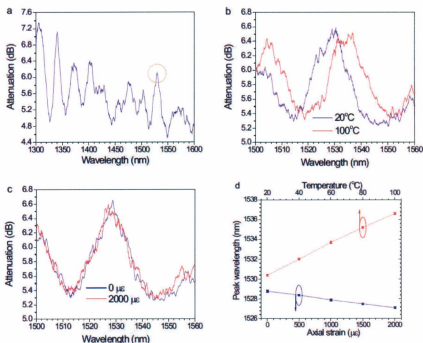


Figure 5-13: (a) Attenuation spectrum of a FMZI fabricated with femtosecond laser pulse energy of 20  $\mu\text{J}$  and irradiation duration of 20 seconds under a 50 $\times$  objective lens (NA 0.80). (b) Attenuation spectra of the FMZI without axial strain at 20 °C and 100 °C, respectively. (c) Attenuation spectra of the FMZI at 20 °C with axial strains of 0 and 2000  $\mu\text{s}$ , respectively. (d) Dependences of the attenuation peak wavelength of the FMZI on temperature and axial strain.

In order to verify the practicability of the femtosecond laser fused ultracompact micro-FMZI in sensing applications, a 20-mm-long FMZI fabricated with the objective lens of 50 $\times$  (NA 0.80) and a laser irradiation duration of 20 seconds was made for the

measurement of axial strain ( $\epsilon$ ) and temperature ( $T$ ) with its attenuation spectrum shown in Fig. 5-13(a). The FMZI was axially stretched at different temperatures controlled by a Sigma system with a temperature accuracy of 0.1 °C. The FMZI was fixed on two linear translation stages (ATS100, Aerotech, Inc) using epoxy glue and the length of the fibre segment containing a 20-mm-long FMZI between the two fixed points was 345 mm. The axial strain was adjusted with the translation stage with an accuracy of 0.5  $\mu\text{m}$  through GPIB system and LABVIEW™ programming control.

In the first test, the environmental temperature was increased from 20 °C to 100 °C with no strain applied on the FMZI and the corresponding shift of the attenuation spectra as shown in Fig. 5-13(b) exhibits a redshift in the peak wavelength from 1530.4 to 1536.6 nm. The shift in the attenuation peak wavelength,  $\delta\lambda_{m,T}$ , due to an increase in temperature can be expressed as Eqn. 5-1. It is apparent from the equation that the attenuation peak wavelength will redshift when the environmental temperature increases.

In the second test, an appropriate axial strain was applied on the FMZI while the temperature was kept constant at 20 °C. Figure 5-13(c) shows a blueshift in the attenuation spectrum from the attenuation peak wavelength of 1528.8 to 1527.1 nm when the axial strain is increased from 0 to 2000  $\mu\epsilon$ . The shift in the attenuation peak wavelength,  $\delta\lambda_{m,\epsilon}$ , due to a change in the axial strain, can be expressed as Eqn. 5-2. The fibre elongation due to axial strain results in a decrease in the difference of the effective refractive indices between the core and the cladding modes because of a decrease in the normalized frequency. The increase in the interferometer length has a weaker impact on the shift of the peak wavelength than the influence of a decrease in the difference of the

effective refractive indices so that the attenuation peak wavelength blueshifts when the axial strain increases. The dependences of the attenuation peak wavelength of the FMZI on temperature and axial strain, shown in Fig. 5-13(d), indicate that the temperature and axial strain sensitivities are  $77.5 \text{ pm}^\circ\text{C}$  (redshift) and  $0.85 \text{ pm}/\mu\epsilon$  (blueshift), respectively.

## **Chapter 6**

# **All Fibre Devices Fabricated with Femtosecond Laser**

### **6.1 Introduction**

Conventional optical fibres are originally designed to be used in telecommunication applications. These days, light can be further controlled through active or passive optical fibre devices, such as fibre amplifiers, fibre gratings and fibre filters. Many techniques have been proposed to fabricate all fibre devices which are compatible with the current optical fibre networks. In this chapter, femtosecond laser microfabrication technique will be explored for the possibility of creating all-fibre devices for different applications.

A long period grating (LPG) consists of axially periodic refractive-index variation in the core of a single-mode optical fibre that couples light in the core to fibre cladding

modes at discrete wavelengths [1, 2]. It is well known that long period gratings have unique applications in optical communication, fibre lasers and fibre sensor system. Since the long period grating was first proposed in 1996 [1], much attention has been paid to the fabrication methods. Ultraviolet exposure through an amplitude mask [3], CO<sub>2</sub> laser [4], electric arc [5, 6], mechanical pressure [7-9], and infrared femtosecond laser [10-17] have been used in fabricating LPGs respectively. The idea of LPG fabrication by focused infrared femtosecond laser pulses was first proposed in 1999 [18] and it was demonstrated that LPGs fabricated with this method have higher temperature resistance and better aging stability as compared with those fabricated by ultraviolet light irradiation. The mechanism of refractive index change induced by infrared femtosecond lasers is very different from that by ultraviolet lasers and some other methods. Infrared femtosecond laser can induce refractive index change in various transparent materials due to the changes in the composition and elemental structure after irradiation by femtosecond laser [10, 18]. In section 6.2 fabrication of a long period grating by point-by-point femtosecond laser irradiations is demonstrated. Different long period grating structures will be investigated by changing the femtosecond laser fabrication parameters. Temperature sensing application based on a long period fibre grating will also be realized.

Optical fibre attenuators are widely used to control optical power in optical fibre telecommunication systems and are highly desirable. Fibre core mode attenuators (CMAs) located along optical fibres are desired to attenuate light transmission of the fibre core mode and allow low loss transmission for the cladding modes. Reported fabrication techniques of optical fibre core mode attenuators includes the fibre core damaged by the

intense local heating from UV laser [19, 25], a fusion-spliced hollow optical fibre region [20, 22], a self-aligned absorber formed on the end of the fibre core [23, 24, 26, 27], hydrogen loaded Ge-B codoped fibre by local heat exposure from electric arc discharge [21, 28, 29], and femtosecond laser irradiation [30, 31]. All these core mode attenuator fabrication techniques need complicated systems, high cost, and a degraded mechanical strength due to the multi-fibre connections or fibre shape modifications. A multi-step process to combine a pair of LPGs and a CMA also restricts applications of fibre bandpass filters. An approach to fabricate a single-mode optical fibre core mode attenuator by femtosecond laser irradiations is discussed in section 6.3. The core mode attenuator can be simply designed with different spot size, spot interval and numbers by tuning femtosecond laser illumination parameters. The interval coating structure effectively results in a reduction of the mode coupling and thus enhances the transmission uniformity with a small attenuation fluctuation.

Recently dynamically tunable wavelength channel selective components have become the key elements in wavelength-division-multiplexed fibre telecommunication systems. Even though commonly used as band-rejection filters for their lossy peaks at the resonance wavelengths in the transmission spectrum [1-3], applications of LPGs in a single mode fibre have so far realized as bandpass filters by core mode attenuators in the middle of two LPGs [19-24]. There are several other methods to fabricate the optical fibre bandpass filter, for example, side polished into a single mode fibre core in evanescent contact with a high-index multimode overlay waveguide [32], inserting two quarter-wave shifts in a short Bragg grating [33], concatenation of arrays of tailored broadband chirped

fibre Bragg gratings [34], imposing a strain gradient to tune a single FBG's transmission bandwidth [35], and splicing a segment of step-index multimode fibre between two standard single mode fibres [36]. In section 6.4 an approach to fabricate an all-fibre bandpass filter by point-by-point femtosecond laser irradiations is studied. Design and fabrication of the filter are described along with discussion on characteristics of output passband spectrum. Compared with the previous fabrication methods, this approach is simple, reproducible and flexible.

In section 6.5, an optical fibre mode converter consisting of femtosecond laser inscribed lines and coating regions was successfully demonstrated for a mode conversion from core mode to cladding mode and radiation mode. When the fibre mode converter is configured with double femtosecond laser inscribed lines without a middle coating region and with an output coating region, an interferometer is formed. The proposed fibre interferometric configuration provides possibilities for filtering applications in communications and sensing applications.

## 6.2 Long Period Fibre Grating

In this section, long period fibre gratings inside a standard single-mode fibre are fabricated with infrared femtosecond laser pulses. Fibre gratings consisting of a periodic perturbation of the refractive index of the core of the optical fibre fall into two categories based upon the period of the grating, one is fibre Bragg gratings with a sub-micron period and the other is long period grating with a period in the range from 100  $\mu\text{m}$  to 1 mm. The

long period grating induces coupling between the propagating core mode and co-propagating cladding modes. The high attenuation of the cladding modes results in the transmission spectrum of the fibre containing a series of attenuation bands centered at discrete wavelengths, each attenuation band corresponding to the coupling to a different cladding mode. Phase matching between the mode propagating in the core of the fibre and a forward-propagating cladding mode is achieved at the wavelength  $\lambda^{(m)}$  [37]

$$\lambda^{(m)} = \Lambda(n_{core} - n_{cladding}^{(m)}), \quad (6-1)$$

where  $\lambda^{(m)}$  is the peak resonance wavelength of mode  $m$ ,  $\Lambda$  is the grating period,  $n_{core}$  and  $n_{cladding}^{(m)}$  are the effective indices of the fundamental core mode and the high order cladding modes, respectively.

The schematic diagram for fabricating LPGs using infrared femtosecond laser pulses is shown in Fig. 6-1. A regenerative Ti:Sapphire femtosecond laser amplifier (Libra-S, Coherent) is used to generate laser pulses with a single pulse energy up to 1 mJ, a central wavelength of 800 nm and a repetition rate of 1 kHz. A half-wave plate and a linear polarizer were inserted in the optical path so that rotating the half-wave plate can attenuate the output power of the laser amplifier. After being reflected by steering mirrors, the laser pulses are focused by an objective lens into the core of a single mode fibre (SMF-28e). The single mode fibre is mounted on a high precision three-axis translation stage (ATS100, Aerotech Inc.) and a precision motorized rotation Stage (495CC, Newport), and its position is precisely adjusted to give the fibre core in a good overlap with the laser focal region. With the help of a CCD camera in conjunction with a beam splitter (BS) the fibre position was precisely adjusted by monitoring the back-reflected

light from the fibre surface when the fibre is irradiated with focused femtosecond laser pulses. Finally, the focal position of the laser beam was right at the center of the fibre core and the femtosecond laser beam movement direction was along the optical fibre longitudinal axis direction.

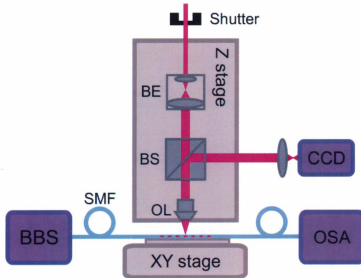


Figure 6-1: Schematic illustration of the femtosecond laser microfabrication system.

The first long period grating has a set of femtosecond laser irradiated spots with a period of  $500\ \mu\text{m}$  (Fig. 6-2). The total length of this grating is 10 mm. The single pulse energy and the pulse duration are  $1\ \mu\text{J}$  and 67 fs, respectively. A  $40\times$  microscope objective lens ( $\text{NA}=0.65$ ) after a beam expander (BE, magnification  $2\times$ ) is used to focus the femtosecond laser beam into the central axis of the fibre. The radiation time of the femtosecond laser pulses at a position was set to 60 seconds by an electronic shutter

(VCM-D1, UNIBLITZ) and the laser beam was blocked when the optical fibre was moved to the next position. The inset of Fig. 6-2 shows an optical micrograph of a single femtosecond laser irradiated spot. During the fabrication process, the transmission spectrum of the long period grating was observed by using an optical spectrum analyzer (Ando 6315E) and white light source (Ando AQ4303B).

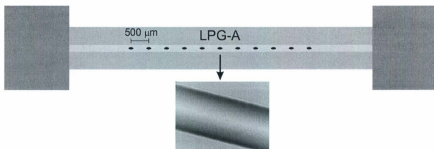


Figure 6-2: Schematic illustration of a long period fibre grating LPG-A with the optical micrograph of a single femtosecond laser irradiated spot.

The transmission spectrum for the long period grating LPG-A is shown in Fig. 6-3. The resonance wavelengths corresponding to different cladding mode orders of the LPG-A were at 1305.7, 1357.9, 1417.3, and 1521.7 nm, respectively. A maximum conversion from the fundamental core mode to cladding modes was obtained at the resonance wavelength of 1305.7 nm as shown by the 10 dB dip in the transmission spectrum. The full-width at half-maximum for this mode coupling at 1305.7 nm (-10 dB in transmission spectrum) was 20 nm.

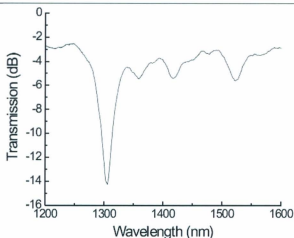


Figure 6-3: Transmission spectrum of the long period grating LPG-A.

Another long period grating was fabricated by a femtosecond laser point-by-point method in a single mode fibre. In this femtosecond point-by-point long period grating, each grating plane was fabricated with one femtosecond laser pulse that was focused into the core of an optical fibre shown in Fig. 6-4. By moving the focal point along the longitudinal axis of the optical fibre with a translation speed, the grating planes were inscribed one by one at the laser pulse repetition rate. Because each femtosecond laser pulse is one grating period, special attention was paid to the laser beam alignment to the optical fibre. The femtosecond laser amplifier (Libra-S, Coherent) was used to generate laser pulses with single pulse energy up to 1  $\mu\text{J}$  and a repetition rate of 1 kHz. The translation stages (ATS100, Aerotech Inc.) were controlled by a controller (UNIDEX511, Aerotech Inc.) through a general purpose interface bus system (GPIB) interface system and LabVIEW<sup>TM</sup> programming control.

A long period grating, LPG-B was fabricated with a translation speed of 1.6 mm/s and therefore the resulting period of the grating is 1.6  $\mu\text{m}$ . Since the size of each femtosecond laser pulse induced spot ( $\sim 10 \mu\text{m}$ ) is larger than the grating period, the feature in the fibre core is a femtosecond laser inscribed line with periodic refractive index change. The inscription time was 10 s, so the total length of the grating was 1.6 cm. The optical micrograph of several femtosecond laser irradiated grating planes is shown in the inset of Fig. 6-4.

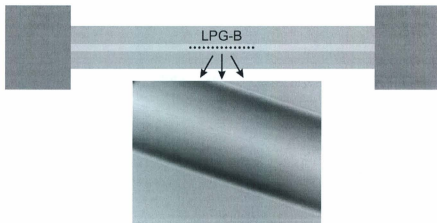


Figure 6-4: Schematic illustration of a long period fibre grating LPG-B with the optical micrograph of several femtosecond laser irradiated grating planes.

The transmission spectrum of the LPG-B measured with the optical spectrum analyzer and white light source is shown in Fig. 6-5(a). It is noted that several transmission dips appear with depths from 4 to 10 dB over a wide spectrum range. These transmission dips correspond to fundamental core mode coupling to different cladding modes. In order to further investigate the properties of the resonance grating peaks, a

specific transmission dip was selected to measure its transmission and reflection spectra by using the OSA and an erbium broadband light source (EBS-7210, MPB Communications). Figure 6-5(b) shows that the transmission dip is -17 dB at the resonance wavelength of 1564.9 nm. This grating has a narrow FWHM bandwidth of 0.4 nm which is comparable with that of an ordinary fibre Bragg grating. However the measured reflection spectrum with no reflection peaks shows that LPG-B is not a typical fibre Bragg grating which may reflect specific wavelengths of light.

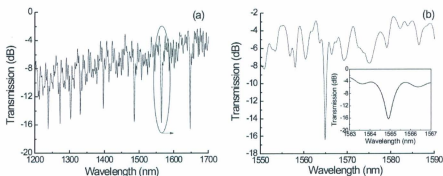


Figure 6-5: (a) Transmission spectrum of the LPG-B. (b) Transmission spectrum of a specific transmission dip of the LPG-B. Inset shows the enlarged curve of the transmission dip.

A long period grating sample, LPG-C, was fabricated to conduct measurements on the temperature sensitivity of the long period grating. A 50 $\times$  microscope objective lens (NA = 0.8) is used to focus the femtosecond laser beam into the core of the single mode fibre. The single femtosecond laser pulse energy and the pulse duration are 0.8  $\mu$ J and 67 fs, respectively. An axial translation speed of 100  $\mu$ m/s for the optical fibre is used for fabricating the grating with a total length of 2 cm. The radiation was periodically blocked

at positions between the adjacent grating planes with an electronic shutter. The long period grating LPG-C has a period of  $400\ \mu\text{m}$  and the length of a grating plane is  $200\ \mu\text{m}$  with a duty cycle of 0.5 shown in Fig. 6-6. The inset of Fig. 6-6 shows an optical micrograph of a single femtosecond laser irradiated grating plane.

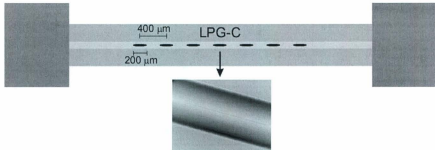


Figure 6-6: Schematic illustration of a long period fibre grating LPG-C with the optical micrograph of a femtosecond laser irradiated grating plane.

The temperature of a laboratory oven (Cole-Parmer Instrument) with the LPG-C inside was changed from  $20$  to  $200\ ^\circ\text{C}$  with  $60\ ^\circ\text{C}$  intervals and the resonance wavelengths of the LPG transmission were recorded. The transmission spectrum of the LPG-C was measured by using an optical spectrum analyzer and white light source (WLS, Ando AQ4303B). The transmission spectra of the LPG-C at different temperature are shown in Fig. 6-7(a), where  $m = 1, 2, 3,$  and  $4$ , represent cladding mode orders of LPGs corresponding to different resonant wavelengths. The resonance wavelengths corresponding to different cladding mode orders of the LPG-C were  $1180.4, 1247, 1326.8, 1506.8\ \text{nm}$  at  $20\ ^\circ\text{C}$  and move to larger wavelengths of  $1190.6, 1258.4, 1339.4, 1521.2\ \text{nm}$

at 200 °C, respectively. Fig. 6-7(b) shows the temperature dependency of the resonance wavelengths of the long period grating LPG-C. For increasing temperatures, the resonant wavelengths redshift to longer wavelengths due to the thermo-optic coefficients of the Ge-doped silica core and the fused silica cladding. The derivative of Eqn. (6-1) with respect to temperature  $T$  can be expressed as

$$d\lambda^{(m)}/dT = d\Lambda/dT \cdot (n_{core} - n_{cladding}^{(m)}) + \Lambda \cdot (dn_{core}/dT - dn_{cladding}^{(m)}/dT). \quad (6-2)$$

In Eqn. (6-2), the temperature dependence of grating period  $d\Lambda/dT$  related with thermal expansion coefficients,  $\alpha = (1/\Lambda)d\Lambda/dT$  (approximately  $0.55 \times 10^{-6} \text{ } ^\circ\text{C}^{-1}$  for silica), is negligible when compared with the temperature dependence of the refractive index of the material,  $d(n_{core} - n_{cladding}^{(m)})/dT$ , (approximately  $8.6 \times 10^{-6} \text{ } ^\circ\text{C}^{-1}$  for germanium doped silica) [38, 39]. Thus the temperature dependence of the long period grating resonance wavelengths can be written as:

$$d\lambda^{(m)}/dT \approx \Lambda \cdot (dn_{core}/dT - dn_{cladding}^{(m)}/dT). \quad (6-3)$$

In the case of Ge-doped core fibre,  $dn_{core}/dT$  is larger than  $dn_{cladding}^{(m)}/dT$ , resulting in a positive value of  $d\lambda^{(m)}/dT$  and a consequent redshift of the LPG resonance wavelengths.

The linear shift of each transmission peak shows a positive slope 0.057, 0.063, 0.07, 0.08 nm/°C for cladding mode orders of  $m = 1, 2, 3,$  and  $4,$  respectively. For lower order cladding modes,  $dn_{cladding}^{(m)}/dT$  is larger than that of the higher order cladding modes. So the difference between  $dn_{core}/dT$  and  $dn_{cladding}^{(m)}/dT$  is smaller for lower order cladding modes compared with that of the higher order cladding modes. Thus the temperature dependence of the long period grating resonance wavelengths increases with the order of the cladding mode from Eqn. (6-3).

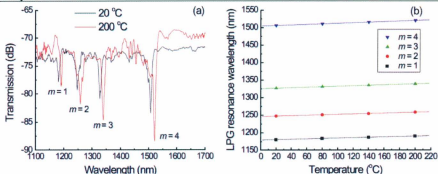


Figure 6-7: (a) Transmission spectra of the LPG-C at 20 °C and 200 °C. (b) Dependence of the wavelength shifts of the resonance peaks of the LPG-C on temperature.

### 6.3 Fibre Core Mode Attenuator

In this section a method for fabrication of a highly efficient optical fibre core mode attenuator by using a femtosecond laser micromachining technique will be investigated. The method utilizes a series of femtosecond laser induced spots in the core of a single mode fibre in between a set of fibre coating areas. The light scattering and absorption efficiently suppress the optical fibre core mode power resulting in a core mode attenuator.

An ultrafast Ti:sapphire regenerative amplifier (Libra-S, Coherent) was used for the fabrication of a single-mode fibre core mode attenuator (SMF-CMA) in this study with the following parameters: wavelength at 800 nm, repetition rate of 1 kHz, and pulse width of 67 fs. A single-mode optical fibre (SMF-28e, Corning) was mounted on the translation stage of the laser micromachining workstation. The plastic coating on the fibre over a

segment of 1 cm in length was stripped off before laser irradiation. Figure 6-8 shows a scheme of the femtosecond laser Gaussian beam focused inside the single-mode optical fibre. The X, Y, Z coordinate axes are associated with radial direction, focus position, longitudinal axis of the optical fibre, respectively. The XY, YZ, XZ coordinate planes show cross-section, side-view, top-view of the optical fibre, respectively.

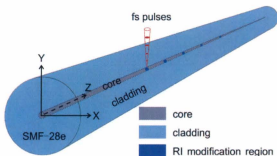


Figure 6-8: Schematic illustration of femtosecond laser pulses induced refractive index modification region on the single-mode optical fibre core along the fibre axis.

A single-spot single-mode core mode attenuator was fabricated with a  $50\times$  objective lens when the femtosecond laser beam (pulse energy of  $7.5 \mu\text{J}$  and irradiation time of 60 s) was focused on the center of the optical fibre core which is the position "b" or "e" in Fig. 6-9(a). The near-field images of the transmitted modes in the SMF-CMA were observed by a wavelength tunable laser (8168F, Agilent), a  $50\times$  lens, and an infrared camera (C2741, Hamamatsu) when the output power of the wavelength tunable laser was set to 0.1 mW and the input light wavelength was tuned to 1550 nm. The 2-D near-field mode profile of the pristine single-mode fibre (top inset in Fig. 6-9(b)) shows that the light energy is mainly in the fundamental core mode. At the position of the focus of the

femtosecond laser beam, a permanent structure change forms due to the high laser intensity induced nonlinear absorption of the femtosecond laser energy by the optical fibre [10]. Thus the single-spot SMF-CMA could be considered as a Mie scattering center of a refractive index (RI) modification region. The near field image observed after the SMF-CMA (bottom inset in Fig. 6-9(a)) indicates that the single-spot SMF-CMA could couple the fundamental core mode to guided cladding mode by Mie scattering. The transmission spectrum of the SMF-CMA was measured by the OSA with an erbium broadband light source (EBS-7210, MPB Communications). The attenuation spectrum of the SMF-CMA is the transmission spectrum difference between a pristine single-mode fibre as a reference fibre and the SMF-CMA. The attenuation spectrum of the single-spot SMF-CMA is shown in Fig. 6-9(b). All wavelengths of light are scattered in both the backward and forward scattering directions while wavelength dependence exists. Consequently, the attenuation at a longer wavelength is lower than that at the shorter wavelength, i.e. 1.72 dB at 1530 nm and 1.56 dB at 1600 nm, as shown in Fig. 6-9(b).

Figure 6-9(c) and (d) show the attenuation change profiles when the femtosecond laser beam was focalized at different radial distances (X axis) and focus positions (Y axis) measured at wavelengths of 1540 nm and 1590 nm, respectively. From Fig. 6-9(c) and (d), the attenuation reaches the maximum at positions "b" and "e" of the fibre core center shown in Fig. 6-9(a), and reaches zero at positions "a" and "c" or "d" and "f" outside the fibre core. The attenuation change profiles in two directions can be fitted to a Gaussian function where the maximum attenuation values of 1540 nm are larger than those of 1590 nm. Insets of Fig. 6-9(b) and 6-9(c) show the top-viewed and side-viewed optical

micrographs of SMF-CMA, respectively. According to Fig. 6-9(c) and (d), the femtosecond laser induced RI modified region is an ellipse with a semi-major axis of 6  $\mu\text{m}$  and a semi-minor axis of 3  $\mu\text{m}$  in Y-X coordinate plane. Figure 6-9(a) illustrates a cross section of this femtosecond laser induced RI modified region which not only covers most of the fibre core but extends to the optical fibre cladding area.

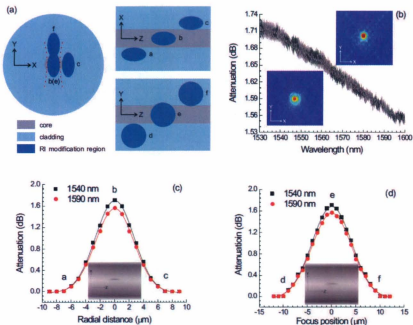


Figure 6-9: (a) Schematic illustration of femtosecond laser Gaussian beam focused at different positions inside the single-mode optical fibre. (b) Attenuation spectrum of a single-spot SMF-CMA, insets are near-field images of a pristine single-mode fibre (top) and the SMF-CMA (bottom). (c) Attenuation change with different radial distances at 1540 nm and 1590 nm, respectively. (d) Attenuation change with different focus positions at 1540 nm and 1590 nm, respectively. Insets of (c) and (d) are top-viewed and side-viewed optical micrographs of the single-spot SMF-CMA, respectively.

To visualize the light energy distribution inside the optical fibre, finite-element simulations using the commercial software COMSOL MULTIPHYSICS are conducted for the femtosecond laser crafted single-mode optical fibre attenuator and the results are presented in Fig. 6-10. For the pristine single-mode fibre at  $\lambda = 1.55 \mu\text{m}$ , energy is confined in the fibre core and thus is a fundamental core mode (Fig 6-10(a)). If the femtosecond laser beam is focused outside the fibre core, output mode profile is still a fundamental core mode (Fig 6-10(b)). When the femtosecond laser beam is focused on the center of the fibre core, the refractive index modification region couples part of the core mode energy to cladding mode energy (Fig 6-10(c), (d), and (e)). Similarly when the femtosecond laser beam is focused at an offset position from the center of the fibre core, the refractive index modification region also couples part of the core mode energy to cladding mode energy (Fig 6-10(f) - (j)). Actually the high intensity focused femtosecond laser pulses may cause voids or cracks at the focal volume inside the optical fibre. An evenly distributed femtosecond laser induced refractive index modification region is presumed for the simulation process although more energy would be coupled from core mode to cladding mode or even irradiation mode taking into account of the morphological structure changes. An optical fibre coating layer of a UV-curable acrylate compound surrounds the cladding layer beyond the 1 cm SMF-CMA region. The refractive index of the coating layer is about 1.5, which is larger than that of the cladding layer [40]. The light energy in the cladding excited by the single-spot SMF-CMA will attenuate in the output coating region due to the refraction loss at the unsmoothed cladding-coating

interface and significant absorption band in the telecommunication window of the coating [41]. Therefore the attenuation mechanism of the single-spot single-mode optical fibre core mode attenuator could be explained by the mode coupling which is the fundamental core mode in the fibre core coupled to guided cladding modes in the fibre cladding and then attenuated to irradiation mode in the fibre coating due to the evanescent wave absorption of the polymer coating of the single-mode fibre.

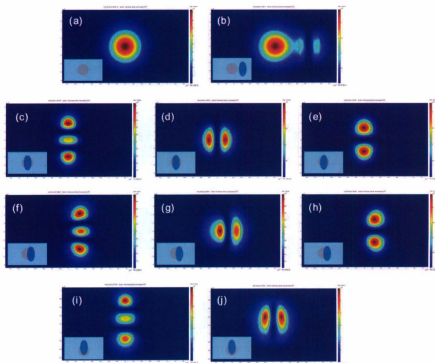


Figure 6-10: Simulation of energy density distribution inside the single-mode fibre with different configurations.

Figure 6-11(a) and (b) show the attenuation spectra of a single-spot SMF-CMA at different laser irradiation durations (with same laser pulse energy of  $7.5 \mu\text{J}$ ) and at different laser pulse energies (with constant laser irradiation duration of  $10 \text{ s}$ ), respectively. The increase in the laser irradiation duration or laser pulse energy induces an accumulated energy dose increase of the femtosecond laser irradiation and consequently the refractive index and dimension of the femtosecond laser modification region increase. According to the Mie scattering theory, the single-spot SMF-CMA induced attenuation depends on both the size and the refractive index contrast of the Mie scattering center of the refractive index modification region. Thus the attenuation spectrum of the SMF-CMA exhibits a strong dependence on the laser irradiation durations and the laser pulse energy. In Fig. 6-11(a), the attenuation is increased from  $0 \text{ dB}$  to  $2.54 \text{ dB}$  when the irradiation duration is changed from  $0.001 \text{ s}$  to  $120 \text{ s}$  at  $1530 \text{ nm}$ . Similarly in Fig. 6-11(b), the attenuation is also increased from  $0 \text{ dB}$  to  $2.57 \text{ dB}$  when the pulse energy is increased from  $3 \mu\text{J}$  to  $22.5 \mu\text{J}$  at  $1530 \text{ nm}$ .

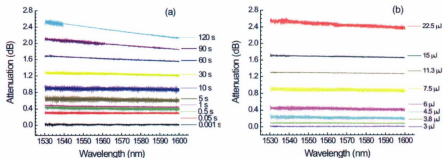


Figure 6-11: (a) Attenuation spectra of a single-spot SMF-CMA with different laser irradiation durations. (b) Attenuation spectra of a single-spot SMF-CMA with different laser pulse energies.

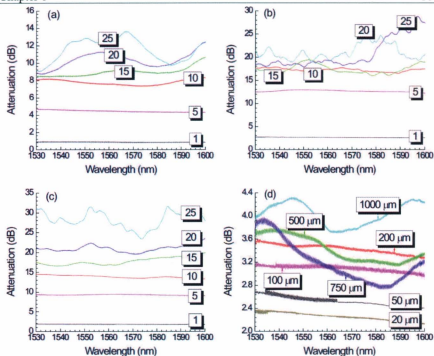


Figure 6-12: Attenuation spectra of multiple-spot SMF-CMAs of a spot interval of  $200\ \mu\text{m}$  with different spot numbers (a) pulse energy of  $7.5\ \mu\text{J}$ , irradiation time of  $10\ \text{s}$ , (b) pulse energy of  $22.5\ \mu\text{J}$ , irradiation time of  $10\ \text{s}$ , (c) pulse energy of  $7.5\ \mu\text{J}$ , irradiation time of  $90\ \text{s}$ . (d) Attenuation spectrum of a five-spot SMF-CMA with different spot intervals (pulse energy of  $7.5\ \mu\text{J}$ , irradiation time of  $10\ \text{s}$ ).

Figure 6-12 show the attenuation spectra of multiple-spot core mode attenuators with specific spot intervals and spot numbers fabricated by different laser irradiation time and laser pulse energies. Comparing Fig. 6-12(a) with Fig. 6-12(b), the attenuation ( $17\ \text{dB}$ ) with larger laser pulse energy ( $22.5\ \mu\text{J}$ ) is larger than the attenuation ( $8\ \text{dB}$ ) with smaller laser pulse energy ( $7.5\ \mu\text{J}$ ) for ten femtosecond laser irradiated spots at  $1530\ \text{nm}$ . For Fig.

6-12(a) and Fig. 6-12(c), the attenuation (15 dB) with longer laser irradiation time (90 s)

is larger than the attenuation (8 dB) with shorter laser irradiation time (10 s) for ten femtosecond laser irradiated spots at 1530 nm. As the number of the femtosecond laser modified spots increases, interference attenuation spectrum with several attenuation peaks is observed and a larger average attenuation is induced. This is because the cladding modes excited by multiple femtosecond laser irradiated spots could interfere with the fundamental core mode like long period grating. The attenuation spectra of the five-spot SMF-CMAs in Fig. 6-12(d) exhibit a dependence on the spot intervals. When the interval increases from 20  $\mu\text{m}$  to 200  $\mu\text{m}$ , the corresponding attenuation will increase. When the spot interval reaches and exceeds 500  $\mu\text{m}$ , interference peaks of the attenuation spectrum will appear. It indicates that even though the output coating segment could suppress the most of the cladding mode energy after the SMF-CMA region, but it will not completely eliminate mode coupling between the core mode and cladding mode.

Figure 6-13 shows attenuation spectra of three single-spot core mode attenuators fabricated using objective lens of 20 $\times$  (NA 0.46), 50 $\times$  (NA 0.8), and 100 $\times$  (NA 0.95), respectively, with the same laser pulse energy of 15  $\mu\text{J}$  and laser irradiation time of 60 s. Optical micrographs of the SMF-CMAs in Fig. 6-9(c) and Fig. 6-13 indicate that the femtosecond laser beam focused by an objective lens of high NA will irradiate on a small spot with the refractive index modification, consequently the relative small femtosecond laser induced refractive index modification region will cause less attenuation loss.

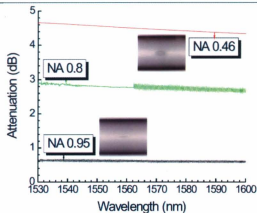


Figure 6-13: Attenuation spectra of a single-spot SMF-CMA fabricated using different objective lenses. Insets are top-viewed optical micrographs of the SMF-CMA using 100 $\times$  (bottom) and 20 $\times$  (top) objective lenses, respectively.

Two five-spot core mode attenuators of different configurations were made by a 20 $\times$  objective lens (NA 0.46) and femtosecond laser illumination of 15  $\mu$ J pulse energy and 60 s exposure time. Fig. 6-14(a) shows the schematic illustration of the optical fibre device structures. The first SMF-CMA consists of five refractive-index-modified regions with a spot interval of 1 mm along a coating removed segment of 1 cm in length, and a coating segment of 0.5 mm in length after each femtosecond laser irradiated spot was preserved in the coating removal process for the second one. The attenuation spectra of these SMF-CMAs are shown in Fig. 6-14(b). Compared with a weak interference spectral curve of the SMF-CMA without the middle coating segments, a smooth spectral response is observed for the SMF-CMA with the middle coating segments. It is indicated that mode coupling between these femtosecond laser irradiated spots is suppressed because of the

energy absorption effect of the optical fibre coating. The transmission spectra of the femtosecond laser crafted SMF-CMA with the middle coating segment and the unmodified pristine SMF are shown in Figure 6-14(c). The fundamental core mode energy was strongly attenuated by the five-spot SMF-CMA and a monotonic rise in transmittance is observed from 1530 to 1600 nm as indicated in Fig. 6-14(c). Maximum attenuation occurring at a shorter wavelength of 1530 nm is 25 dB and minimum attenuation at a longer wavelength of 1600 nm is 14 dB.

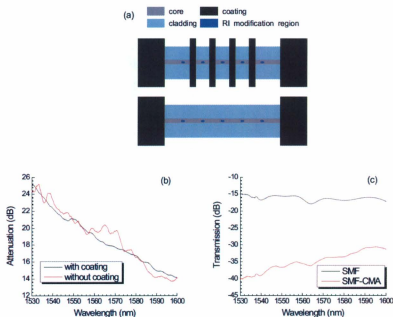


Figure 6-14: (a) Schematic illustration of femtosecond laser crafted SMF-CMAs with and without a middle coating segments. (b) Attenuation spectra of the five-spot SMF-CMAs with and without a middle coating segments. (c) Transmission spectra of the five-spot SMF-CMA and pristine SMF with the middle coating segment.

## 6.4 Fibre Bandpass Filter

In this section we demonstrate an all-fibre bandpass filter with a core mode attenuator between two long period fibre gratings made by point-by-point femtosecond laser irradiations. The proposed all-fibre bandpass filter consists of a core mode attenuator between a LPG pair is schematically illustrated in Fig. 6-15. The first long period grating, LPG-1, couples light from the core mode to the phase-matching cladding modes. The resonance wavelength  $\lambda_i$  satisfies the phase-matching condition  $\lambda_i = (n_{core} - n_{clad}^i)\Lambda$ , where  $n_{core}$  and  $n_{clad}^i$  are the effective refractive indices of the core mode and the  $i$ th-order cladding mode in LPG-1, respectively. The core modes that are not resonant with LPG-1 are extinguished by the core mode attenuator and the cladding modes from the LPG-1 bypass the CMA. The second identical long period grating LPG-2 couples back the cladding modes into the core mode at the resonance wavelength. After passing the concatenated LPG-1 - CMA - LPG-2 structure, this fibre-optic device exhibits passband characteristics at the resonance wavelength of the two LPGs.

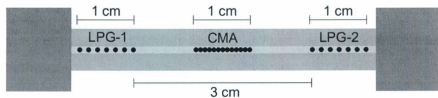


Figure 6-15: Schematic illustration of an all-fibre bandpass filter.

The maximum femtosecond laser pulse energy was 1mJ which was attenuated to 1  $\mu$ J with a zero-order half wave plate and polarizer. The 800 nm radiation was focused by a

$50\times$  objective lens with numerical aperture 0.80 into the optical fibre. A segment of protective plastic coating on the fibre (SMF28e, Corning Inc.) was stripped off before laser irradiations. The period of the LPGs is  $400\ \mu\text{m}$  and the length of the grating plane is  $100\ \mu\text{m}$  shown in the inset of Fig. 6-16. For each grating plane, the focus of the laser beam was translated along the axis of the optical fibre core at a speed of  $100\ \mu\text{m/s}$ . The radiation was periodically blocked at positions between the adjacent grating planes with an electronic shutter. The length of the long period grating is 1 cm with 25 grating planes. The transmission spectrum of the all-fibre bandpass filter was measured by the OSA and white light source (Ando AQ4303B). Figure 6-16 shows the transmission spectrum of LPG-1 with a main peak at 1435 nm. A second identical long period grating, LPG-2, was fabricated at a distance of 3 cm from the LPG-1.

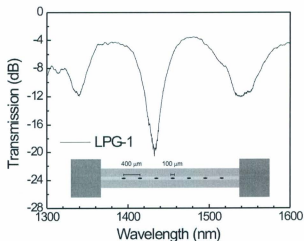


Figure 6-16: Transmission spectrum of LPG-1. Inset is a scheme of the long period fibre grating.

The core mode attenuator in the middle between the two long period gratings was made by femtosecond laser beam exposure on the fibre core to form a series of spots. The local damage of the fibre core at these spots will induce scattering loss and the fibre core mode energy is blocked. The pulse energy of the 800 nm radiation incident on the fibre core was 1  $\mu$ J. The optical fibre was moved perpendicular to the femtosecond laser beam by a motion stage with a speed of 1 mm/min. The length of the core mode attenuator is 1 cm. Figure 6-17 shows the core mode transmission spectra with and without the core mode attenuator. The core mode was strongly attenuated and the extinction ratio of the core mode with and without the core mode attenuator was over 20 dB.

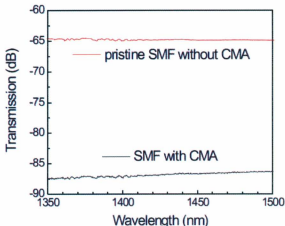


Figure 6-17: Transmission spectra of single mode fibre with and without core mode attenuator.

Figure 6-18 shows the transmission spectrum of the LPG-2 and the fibre bandpass filter consisting of the LPG pair and the CMA. The LPG-2 has a 15 nm full-width at half-maximum (FWHM) at the resonance wavelength of 1430 nm. For the fibre bandpass

filter, non-resonance wavelengths are suppressed by more than 20 dB over the spectral range outside the LPG resonance peak wavelength. Thus we found a passband at a center wavelength of 1430 nm over the spectral range from 1390 nm to 1460 nm.

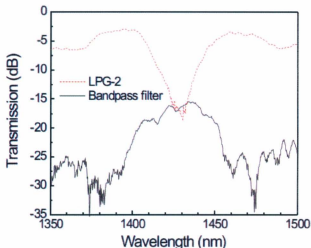


Figure 6-18: Transmission spectra of LPG-2 and fibre bandpass filter.

The all-fibre bandpass filter can be simply designed with different spot size, interval, and number by changing femtosecond laser illumination parameters. The proposed device has advantages such as inherent wavelength selectivity, low cost fabrication, simple design of in-line fibre structure, and free of insertion loss induced by fusion splicing. The potential applications of the all-fibre bandpass filter include wavelength-division-multiplexing filters, wavelength selectors for fibre lasers, and fibre-optic sensors.

## 6.5 Fibre Mode Converter

In this section, an effective method to excite guided cladding modes and radiation modes from the fundamental core mode of a single-mode fibre is proposed. The experiments demonstrate a mode conversion process by modifying the single mode fibre with femtosecond laser inscribed lines and coating regions. A fibre interferometer based on this configuration is proposed.

The femtosecond Ti:sapphire regenerative amplifier (Libra-S, Coherent) operating at a wavelength of 800 nm with a repetition rate of 1 kHz and a pulse width of 67 fs was used to fabricate the fibre mode converter. A focusing objective lens with a magnification of 50 $\times$  and numerical aperture of 0.80 was used. Femtosecond laser pulses with a pulse energy of 2  $\mu$ J were focused on the fibre core of a single-mode optical fibre (SMF-28e) where a section of the coating was stripped off. The focused laser beam was translated along the fibre axis at a speed of 100  $\mu$ m/60 s to make a 0.1 mm straight line. Fig. 6-19 shows the schematic illustration of the femtosecond laser inscribed optical fibre device. The optical micrograph of the femtosecond laser inscribed line (fs-laser line) is shown in the inset of Fig. 6-19. A second fs-laser line of the same geometry was fabricated 40 mm away from the first one with a 35 mm coating section in the middle. The refractive index of the coating layer is larger than that of the cladding layer and the coating thickness is about 62.5  $\mu$ m. A, B, C, D, and E represent five fibre-tip end positions where the output side edge of the optical fibre mode converters were located. A is before the first fs-laser line, B is after the first fs-laser line and before the middle coating region, C is after the

middle coating region and before the second fs-laser line, D is after the second fs-laser line and before the output coating region, and E is within the output coating region.

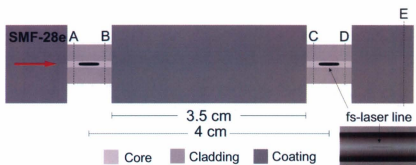


Figure 6-19: Schematic illustration of the optical fibre mode converter. Inset is the optical micrograph of the femtosecond laser inscribed line.

Transmission spectra of different femtosecond laser fabricated optical fibre mode converters were measured with an erbium broadband light source (EBS-7210, MPB Communications) and the optical spectrum analyzer shown in Fig. 6-20. The insertion loss difference of optical fibre connectors at positions from A to E is less than 0.2 dB. The near-field mode profiles of the transmitted modes in the optical fibre mode converters were observed by a wavelength tunable laser (8168F, Agilent), a 100 $\times$  lens, an infrared camera (C2741, Hamamatsu) and its controller connected to a computer shown in Fig. 6-20(a). Figure 6-20(a) shows the transmission spectrum of the optical fibre mode converter with an end position of A. A three-dimensional near-field pattern of the pristine single-mode fibre indicates that the light energy is mainly in the fundamental mode when the output power of the tunable laser is set to 0.1 mW and the input light wavelength is tuned to 1550 nm.

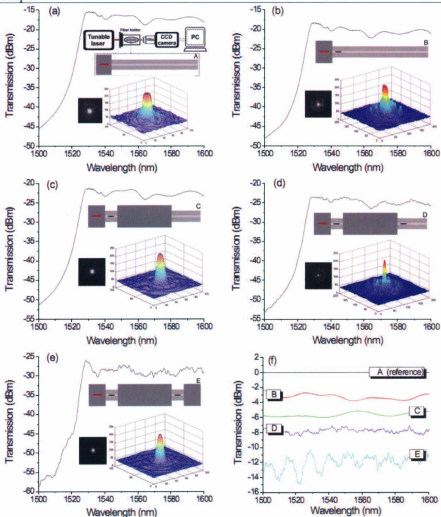


Figure 6-20: (a) - (e) Transmission spectra of femtosecond laser fabricated optical fibre mode converters. Insets are near-field mode profile measurement setup, optical fibre device structures, as well as corresponding near-field images and three-dimensional near-field patterns. (f) Relative transmission spectra of femtosecond laser fabricated optical fibre mode converters.

When the optical fibre mode converter was cut at the position of B, the near-field image is recorded and shown in Fig. 6-20(b). The femtosecond laser inscribed line as a Mie scattering center couples part of the energy in the fundamental mode to the cladding mode. The energy transition from core mode to cladding mode makes light intensity at the center of fibre core weak relative to that in Fig. 6-20(a). Light energy coupled into the optical fibre cladding region is mainly distributed within the core/cladding interface and fades out to the outer cladding region. The near-field image taken at the output end of the optical fibre mode converter, position C, is shown in Fig. 6-20(c). The near-field pattern is a reduced fundamental core mode compared with Fig. 6-20(a) because the light energy in the cladding from the first fs-laser line is attenuated in the middle coating region due to the refraction loss between the cladding/coating interface. The optical fibre coupler includes two fs-laser lines when the fibre was cut at the position of D shown in Fig. 6-20(d). The near-field profile in Fig. 6-20(d) shows that the weakened fundamental mode is once again coupled into cladding mode by the second fs-laser line. In Fig. 6-20(e), observed at the position of E within the output coating region, the near-field profile at the output end is fundamental core mode. Compared with Figs. 6-20(b) and 6-20(d), light energy is mainly in the fundamental mode inside the fibre core and no clear cladding mode is observed. The light intensity of core mode in Fig. 6-20(e) is further attenuated compared with Figs. 6-20(a) and 6-20(c).

The transmission spectrum of Fig. 6-20(a) is the emission spectrum of the  $\text{Er}^{3+}$  broadband light through the pristine single-mode fibre. With all those transmission spectra of different fibre device structures in Fig. 6-20, relative transmission spectra (Fig.

6-20(a) as the reference spectrum) are shown in Fig. 6-20(f). It is shown that the transmittances from A to E in Fig. 6-20(f) is gradually decreased with the emergence of multiple femtosecond laser inscribed lines and coating regions, because of energy absorption of the coating layers and scattering of the fs-laser lines. In the case of only one fs-laser line existing (B and C), a weak interference fringe appears for B, because the fs-laser line and the fibre-tip end (4% reflectance mirror) form a Michelson interference cavity where guided cladding mode and reflected backward cladding mode interfere. The interference fringe is not distinct due to the output coating region in C. In the case of two fs-laser lines existing (D and E), an interference fringe appears for E, because the two fs-laser lines form a Mach-Zehnder interference cavity where the second fs-laser line may couple the significantly attenuated cladding mode energy (most energy is lost in the middle coating region) back to fundamental core mode. Furthermore the output coating region of E avoids the vanishing of the interference fringe by attenuating the cladding mode excited by the second fs-laser line, unlike D.

In order to verify the incident light propagation through a femtosecond laser inscribed line and the energy absorption effect of the coating region, a 2-D finite element analysis has been adopted with the results presented in the top of Fig. 6-21. It is indicated that the energy of fundamental core mode,  $LP_{01}$ , in the single-mode fibre will be partly converted to high-order guided cladding modes,  $LP_{0n}$ , after passing through the fs-laser line and all the high-order  $LP_{0n}$  cladding modes will be coupled to radiation mode within the fibre coating with a high refractive index ( $\sim 1.5$ ). The mode conversion process in the femtosecond laser modified optical fibre mode converter without a middle coating region

is illustrated in the middle of Fig. 6-21. The bottom of Fig. 6-21 illustrate the 2-D output near-field mode patterns recorded at positions F and G when input wavelength is tuned to 1518, 1551, 1579, and 1588 nm, respectively. Position F is after the second fs-laser line and before the output coating region and position G is within the output coating. It is clear that the near-field pattern will be wavelength-dependent cladding modes of different orders without an output coating region and be wavelength-dependent fundamental core mode of different intensities with an output coating region.

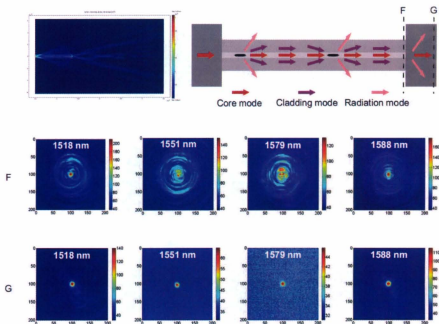


Figure 6-21: Top left, simulation of light energy density distribution through a fs-laser line and a coating region at  $\lambda = 1.55 \mu\text{m}$ . Top right, illustration of the mode conversion process at different fibre device structures. Bottom, two-dimensional near-field patterns for different structures measured at different wavelengths.

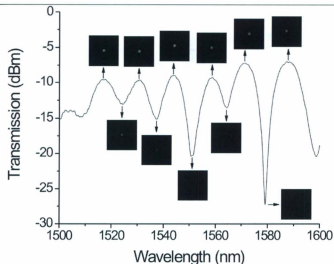


Figure 6-22: Transmission spectrum of the optical fibre mode converter consisting of two femtosecond laser inscribed line without a middle coating region. Insets are near-field images at different wavelengths.

Figure 6-22 shows a transmission spectrum of two femtosecond laser inscribed line without a middle coating region and with an output coating region. A set of attenuation bands are observed within the transmission spectrum to generate an interference pattern. When two femtosecond laser inscribed lines are spatially separated, a Mach-Zehnder interferometer is formed due to the phase difference between the fundamental core mode and the higher order cladding modes. The resonance wavelength  $\lambda_m$  of the interferometer can be expressed as  $\lambda_m = 2\Delta n_{\text{eff}}L/(2m+1)$ , where  $\Delta n_{\text{eff}}$  is the difference of the effective refractive indices between the core and the cladding modes,  $L$  is the length of the interferometer, and  $m$  is the interference order. In the insets of Fig. 6-22, the near-field

images taken at different wavelengths indicate an output fundamental mode in the fibre core of different intensities. At the resonance wavelength of 1579 nm with a peak transmission attenuation of 20 dB, 99% of the fundamental mode energy at the resonance wavelength is coupled to the cladding mode and is further coupled to radiation mode by the output coating region. However at the resonance wavelength 1588 nm, a strong light output is observed. Similar phenomena are also observed when the wavelength was changed from these two resonance wavelength, 1579 nm and 1588 nm, toward the resonance wavelength with a wavelength spacing step of  $\Delta\lambda_m = \lambda^2 / \Delta n_{\text{eff}} L$ .

In this section, an optical fibre mode converter consisting of femtosecond laser inscribed lines and coating regions was successfully demonstrated for mode coupling between core mode, cladding mode, and radiation mode. If the fibre mode converter is configured with double femtosecond laser inscribed lines without a middle coating region and with an output coating region, an interferometer is formed. The proposed fibre interferometric configuration provides possibilities for filtering applications in communications and sensing applications.

## Chapter 7

### Conclusions

In this dissertation, fabrication, properties, and applications of microstructured optical fibre devices have been studied. Microstructured optical fibres have been investigated as useful fibre optic devices for a range of sensing applications and spectral control.

The application of polyimide-coated fibre Bragg grating as a substance sensor and the identification of the dependences of the sensitivity and time response on the coating thickness as well as factors influencing these properties are presented. As an example of polyimide-coated sensor for detecting soluble substances, the use of the grating for salinity measurement shows that a judicious selection of coating thickness is needed in order to achieve suitable sensitivity and time response for specific application. The experimental results indicate that the salinity sensitivities of the polyimide-coated FBGs increase with increasing coating thicknesses, while the response time is another signature for discriminating different parameters. Intelligent sensing of multiple environmental parameters with a single-fibre sensor system is achieved through the use of multiplexed

fibre Bragg gratings with coatings of different polymers and specifications. Using three FBGs of either acrylate or polyimide coating and polyimide coatings of different thicknesses, *in situ* discrimination of saccharinity, salinity, and temperature from the changes in the optical responses of the Bragg wavelengths of the gratings has been realized. Optical low-coherence reflectometry for deflection measurement with fibre Bragg grating cantilever sensor reveals the internal structure of the sensing fibre in correlation with its optical properties, which is the first report on a spatial-resolved technique to realize dynamic deflection measurement. The change in the fibre length during a convex or concave deflection of the cantilever sensor detected by OLCR achieves simultaneous determination of the magnitude and direction of the deflection by the use of a standard single-mode telecommunication fibre inscribed with single grating. Through the FBG transmission spectrum measurement, temperature compensation is realized.

An approach to achieve simultaneous wavelength locking and spectral filtering is accomplished by the use of fibre Bragg grating embedded polarisation maintaining fibre Sagnac loop mirror through temperature tuning. The opposite temperature sensitivities of the FBG Bragg resonance wavelengths and the interferometric peaks of the fibre Sagnac loop mirror, as well as their pronounced difference in the bandwidth, provide an opportunity to realize simultaneous wavelength locking and spectral filtering. Wavelength control by the use of fibre Bragg grating imprinted polarization maintaining fibre Sagnac loop mirror is realized through polarization and strain tuning. The Bragg wavelengths of the FBG in the PMF along slow or fast axis show a redshift with the increase of strain.

However, the interferometric peak wavelength of the Sagnac loop mirror exhibits a blueshift with the increase in strain. The opposite strain sensitivities provide an ideal compensation mechanism to realize wavelength control for specific applications. The nature of the narrow bandwidth of the FBG resonance peak and relatively broad bandwidth of the interferometric peaks of the Sagnac loop mirror as well as their tuning capability, offer an excellent combination to achieve switching from PMFBG filter to SLM comb. A fibre Sagnac interferometer with an integrated polarization maintaining fibre Bragg grating achieves simultaneous temperature and axial strain measurement, which may possess a possibility to simultaneously measure multiple measurands by monitoring the changes in the fast axis and slow axis polarization maintaining fibre Bragg resonance wavelengths and multiple interference peak wavelengths of the fibre Sagnac interferometer.

Two kinds of fibre Mach-Zehnder interferometers have been fabricated, one is symmetrical fibre Mach-Zehnder interferometer with double fibre tapers and the other is asymmetrical fibre Mach-Zehnder interferometer with a fibre taper and a fibre lateral-shifted junction. An approach to realize simultaneous measurement of refractive index, axial strain, and temperature with a fibre Mach-Zehnder interferometry of high sensitivity is proposed and demonstrated. The asymmetrical fibre Mach-Zehnder interferometer offers the possibility to tune its sensing performance either direction dependent or independent to satisfy requirements of specific applications. Furthermore, the asymmetrical structure of the interferometer with flexible device specifications as well as its arbitrarily selectable interference orders provides a possibility to measure a

large number of measurands with different sensitivities to environmental parameters. The influence of structure parameters on the spatial frequency spectra of the fibre Mach-Zehnder interferometers is investigated. Simultaneous measurement of refractive index and temperature based on a triple tapered fibre Mach-Zehnder interferometer of high sensitivity is accomplished.

Fibre Mach-Zehnder interferometers consisting of an ultrafast laser microfabricated spot and either a fibre taper or a fibre lateral-shifted junction have been successfully adopted for sensing of different environmental parameters. The sensitivities of temperature, axial strain, and refractive index of the interferometers with different specifications have been experimentally measured and analyzed, which show that the sensitivities of the fibre interferometer are strongly dependent on the selection of the operation attenuation peak wavelength as well as the interferometer length. The proposed fibre interferometric configuration presents a compact one-fibre solution for the sensing measurement with the merits of simplicity in the sensing principle, high sensitivities, high mechanical strength, and ease of fabrication. A fibre Mach-Zehnder interferometer is also fabricated with two spots on the core of a single mode fibre by femtosecond laser irradiations. The spots are considered as Mie scattering central spheres whose sizes are adjustable by the adoption of objective lens of different numerical apertures. The spots coupled the light from the core mode to the cladding mode or vice versa to form Mach-Zehnder interference and the sizes of the spots determined the attenuation loss, interference amplitude and other parameters. The experimental results indicate that an objective lens of small numerical aperture induces a strong Mach-Zehnder interference

with a high attenuation loss.

A femtosecond laser approach has been used to create several kinds of all fibre devices for different applications. Firstly, several long period fibre gratings are fabricated by point-by-point femtosecond laser irradiations. Different long period grating structures have been investigated by changing the femtosecond laser fabrication parameters. Temperature sensing application based on a long period fibre grating has also been realized. Secondly, optical fibre core mode attenuators can be designed with different spot size, spot interval and numbers by tuning femtosecond laser illumination parameters. The interval coating structure effectively results in a reduction of the mode coupling and thus enhances the transmission uniformity with a small attenuation fluctuation. An all fibre bandpass filter consisting of two identical long period gratings and a core mode attenuator is fabricated by point-by-point femtosecond laser irradiation. An optical fibre mode converter consisting of femtosecond laser inscribed lines and coating regions is made to couple modes between core mode, cladding mode, and radiation mode. When the fibre mode converter is designed to have double femtosecond laser inscribed lines without a middle coating region and with an output coating region, an interferometer is formed which provides possibilities for filtering applications in communications and sensing applications.

Parts of the research results have been published in one invited book chapter (#1), fourteen journal papers (#2-#15), and sixteen conference presentations (#16-#31) listed below. Papers starting with asterisks are papers on research results obtained in both Ph. D. and M. Sc. programs. The editorial office of the prestigious journal *Electronics Letters*

published a feature article in the front of the issue of November 25, 2010 entitled Sensing changes: a compact fibre refractive index sensor (*Electronics Letters* Vol. 46, No. 24, p.1597 2010), introducing our achievement on the development of the first femtosecond laser fabricated refractive index sensor with temperature compensation. Another work was featured in the "In Brief" section (Volume 47, Issue 19) in *Electronics Letters* with comments of "A light cold: a simple and passive method for the measurement of liquid level and temperature using one fiber and one feedthrough solution has been proposed by researchers in Canada. Their technique has important applications in cryogenic fuel management in micro-gravity environments."

1. (Invited book chapter) \*Q. Chen and P. Lu, *Fibre Bragg gratings and their applications as temperature and humidity sensors*, in *Atomic, Molecular and Optical Physics: New Research*, (Ed. L. T. Chen, Nova Science Publishers, Inc., Hauppauge, NY, USA, 2008 4th Quarter, ISBN: 978-1-60456-907-0.)
2. (Feature in brief) T. Chen, R. Chen, P. Lu, Q. Chen, and K. P. Chen, Tapered fiber Mach-Zehnder interferometer for simultaneous measurement of liquid level and temperature, *Electron. Lett.* **47**(19), 1093-1095 (2011).
3. P. Lu and Q. Chen, Femtosecond laser microfabricated fiber Mach-Zehnder interferometer for sensing applications, *Opt. Lett.* **36**, 268 (2011).
4. L. Men, P. Lu, and Q. Chen, Femtosecond laser trimmed fiber taper for simultaneous measurement of axial strain and temperature, *IEEE Photon. Technol. Lett.* **23**, 320 (2011).

5. (Feature article) P. Lu and Q. Chen, Femtosecond laser microstructured fibre refractive index sensor with temperature compensation, *Electron. Lett.* **46**, 1616-1617 (2010).
6. P. Lu and Q. Chen, Asymmetrical fiber Mach-Zehnder interferometer for simultaneous measurement of axial strain and temperature, *IEEE Photon. J.* **2**, 942 (2010).
7. P. Lu, L. Men, and Q. Chen, Wavelength control with grating imprinted fiber Sagnac loop mirror by polarization and strain tuning, *J. Appl. Phys.* **106**, 013111 (2009).
8. P. Lu and Q. Chen, Optical low-coherence reflectometry for deflection measurement with fiber Bragg grating cantilever sensor, *Meas. Sci. Technol.* **20**, 075303 (2009).
9. L. Men, P. Lu, and Q. Chen, Spectral filtering using fibre Bragg grating embedded Sagnac loop mirror, *Electron. Lett.* **45**, 402 (2009).
10. P. Lu, L. Men, K. Sooley, and Q. Chen, Tapered fiber Mach-Zehnder interferometer for simultaneous measurement of refractive index and temperature, *Appl. Phys. Lett.* **94**, 131110 (2009).
11. \*P. Lu, L. Men, and Q. Chen, Polymer-coated fiber Bragg grating sensors for simultaneous monitoring of soluble analytes and temperature, *IEEE Sen. J.* **9**, 340 (2009).
12. P. Lu, L. Men, and Q. Chen, Tuning the sensing responses of polymer-coated fiber Bragg gratings, *J. Appl. Phys.* **104**, 116110 (2008).
13. \*P. Lu and Q. Chen, Fiber Bragg grating sensor for simultaneous measurement of flow rate and direction, *Meas. Sci. Technol.* **19**, 125302 (2008).

14. L. Men, P. Lu, and Q. Chen, Intelligent multiparameter sensing with fiber Bragg gratings, *Appl. Phys. Lett.* **93**, 071110 (2008).
15. \*P. Lu, L. Men, and Q. Chen, Resolving cross sensitivity of fiber Bragg gratings with different polymeric coatings, *Appl. Phys. Lett.* **92**, 171112 (2008).
16. (Invited) Q. Chen and P. Lu, Femtosecond laser microstructured optical fiber sensors, Asia Communications and Photonics Conference, Shanghai, China (2011).
17. P. Lu and Q. Chen, Optical fiber Mach-Zehnder interferometer sensor fabricated by femtosecond laser and electrical arc, Canadian Association of Physicists Congress, St. John's, Canada (2011).
18. Q. Chen and P. Lu, Microstructured fiber Mach-Zehnder interferometers for simultaneous measurement of axial strain and temperature, 21st International Conference on Optical Fiber Sensors, Ottawa, Canada (2011).
19. P. Lu and Q. Chen, Fiber Bragg grating cantilever sensor system for fluid flow monitoring with temperature compensation, 21st International Conference on Optical Fiber Sensors, Ottawa, Canada (2011).
20. P. Lu and Q. Chen, Refractive index measurement with a femtosecond laser microfabricated optical fiber, Photonics North 2011, Ottawa, Canada (2011).
21. P. Lu, L. Men, and Q. Chen, Multiplexed fiber Bragg gratings as a substance sensor, 2010 Symposium on Photonics and Optoelectronic, Chengdu, China (2010).
22. P. Lu, L. Men, K. Sooley, and Q. Chen, Microstructured optical fiber for simultaneous measurement of refractive index and temperature, Photonic Microdevices/Microstructures for Sensing II, Orlando, USA (2010).

23. L. Men, P. Lu, and Q. Chen, Fiber-optic sensor system for simultaneous measurement of different environmental parameters, Advanced Environmental, Chemical, and Biological Sensing Technologies VII, Orlando, USA (2010).
24. P. Lu and Q. Chen, Simultaneous measurement of salinity and temperature with a fibre optic sensor, the Eighteenth Annual Newfoundland Electrical and Computer Engineering Conference, St. John's, Canada (2010).
25. Y. Ding, P. Lu, and Q. Chen, Bulk-heterojunction polymer solar cells with improved efficiency, the Eighteenth Annual Newfoundland Electrical and Computer Engineering Conference, St. John's, Canada (2010).
26. L. Men, P. Lu, and Q. Chen, Fiber Bragg grating sensor for simultaneous measurement of multiple parameters, Conference on Lasers and Electro-Optics/International Quantum Electronics, Baltimore, USA (2009).
27. (Invited) Q. Chen, P. Lu, and L. Men, Fibre Bragg grating for optical biosensors, Canadian Association of Physicists Congress, Quebec City, Canada (2008).
28. P. Lu and Q. Chen, Fiber Bragg grating bending measurement using a high-resolution reflectometer, Canadian Association of Physicists Congress, Quebec City, Canada (2008).
29. P. Lu, L. Men, and Q. Chen, Fiber Bragg grating deflection sensor, Photonics North 2008, Montreal, Canada (2008).
30. Y. Ding, P. Lu and Q. Chen, Optimizing material properties of bulk-heterojunction polymer films for photovoltaic applications. Photonics North 2008, Montreal, Canada (2008).

- 
31. L. Men, P. Lu, and Q. Chen, High-resolution reflectometer for monitoring of biological samples, Photonics North 2008, Montreal, Canada (2008).

# Bibliography

## Chapter 1

- [1] G. Meltz, W. W. Morey, and W. H. Glenn, *Opt. Lett.* **14**, 823 (1989).
- [2] L. Reekie, R. Mears, S. Poole, and D. Payne, *J. Lightwave Technol.* **4**, 956 (1986).
- [3] V. Mizrahi, D.J. DiGiovanni, R.M. Atkins, S.G. Grubb, Yong-Kwan Park, and J.-M.P. Delavaux, *J. Lightwave Technol.* **11**, 2021 (1993).
- [4] E. M. Dianov, A. A. Abramov, M. M. Bubnov, A. V. Shipulin, A. M. Prokhorov, S. L. Semjonov, A. G. Schebunjaev, G. G. Devjatykh, A. N. Guryanov and V. F. Khopin, *Opt. Fiber Technol.* **1**, 236 (1995).
- [5] K. O. Hill, D.C. Johnson, F. Bilodeau, and S. Faucher, *Electron. Lett.* **23**, 464 (1987).
- [6] F. Bilodeau, K. O. Hill, B. Malo, D. C. Johnson, and J. Albert, *IEEE Photon. Technol. Lett.* **6**, 80 (1994).
- [7] D. C. Johnson, K. O. Hill, F. Bilodeau, and S. Faucher, *Electron. Lett.* **23**, 668 (1987).
- [8] T. J. Cullen, H. N. Rourke, C. P. Chew, S. R. Baker, T. Bricheno, K. C. Byron and A. Fielding, *Electron. Lett.* **30**, 2160 (1994).
- [9] F. Bilodeau, D.C. Johnson, S. Thenault, B. Malo, J. Albert, and K. O. Hill, *IEEE Photon.*

*Technol. Lett.* **7**, 388 (1995).

[10] L. Dong, P. Hua, T. A. Birks, L. Reekie, and P. St. J. Russell, *IEEE Photon. Technol. Lett.* **8**, 1656 (1996).

[11] H. G. Winful, *Appl. Phys. Lett.* **46**, 527 (1985).

[12] P. M. Cavaleiro, F. M. Araujo, L. A. Ferreira, J. L. Santos, and F. Farahi, *IEEE Photon. Technol. Lett.* **11**, 1635 (1999).

[13] C.-Y. Lin, L. A. Wang, and G.-W. Chem, *J. Lightwave Technol.* **19**, 1159 (2001).

[14] C.-L. Zhao, X. Yang, M. S. Demokan, and W. Jin, *J. Lightwave Technol.* **24**, 879 (2006).

[15] M. G. Xu, L. Reekie, Y. T. Chow and J. P. Dakin, *Electron. Lett.* **29**, 389 (1993).

[16] Y. Zhao, Q.-Y. Meng, and K. Chen, *Sensors Actuators A* **126**, 112 (2006).

[17] R. Falciai, A. G. Mignani, and A. Vannini, *Sensors Actuators B* **74**, 74 (2001).

[18] K. O. Hill, Y. Fujii, D. C. Johnson, and B. S. Kawasaki, *Appl. Phys. Lett.* **32**, 647 (1978).

[19] R. M. Atkins, and V. Mizrahi, *Electron. Lett.* **28**, 1743 (1992).

[20] D. P. Hand, and P. St. J. Russell, *Opt. Lett.* **15**, 102 (1990).

[21] J. P. Bernandin, and N. M. Lawandy, *Opt. Commun.* **79**, 194 (1990).

[22] M. Douay, W. X. Xie, T. Taunay, P. Bernage, P. Niay, P. Cordier, B. Poumellec, L. Dong, J. F. Bayon, H. Poignant, and E. Delevaque, *J. Lightwave Technol.* **15**, 1329 (1997).

[23] P. Y. Fonjallaz, H. G. Limberge, R. P. Salathe, F. Cochet, and B. Leuenberger, *Opt. Lett.* **20**, 1346 (1995).

[24] N. H. Ky, H. G. Limberge, R. P. Salathe, F. Cochet, and L. Dong, *Appl. Phys. Lett.* **74**, 516 (1999).

[25] H. G. Limberge, P. Y. Fonjallaz, R. P. Salathe, and F. Cochet, *Appl. Phys. Lett.* **68**, 3069 (1996).

[26] B. S. Kawasaki, K. O. Hill, D. C. Johnson, and Y. Fujii, *Opt. Lett.* **3**, 66 (1978).

- [27] K. O. Hill, B. Malo, F. Bilodeau, D. C. Johnson, and J. Albert, *Appl. Phys. Lett.* **62**, 1035 (1993).
- [28] D. Z. Anderson, V. Mizrahi, T. Erdogan, and A. E. White, *Proceedings of the Conference on Optical Fibre Communication, OFC'93, Technical Digest*, p.68 (1993).
- [29] B. Malo, K. O. Hill, F. Bilodeau, D. C. Johnson, and J. Albert, *Electron. Lett.* **29**, 1668 (1993).
- [30] A. D. Kersey, M. A. Davis, H. J. Patrick, M. LeBlanc, K. P. Koo, C. G. Askins, M. A. Putnam, and E. J. Friebele, *J. Lightwave Technol.* **15**, 1442 (1997).
- [31] B. Ball and W. W. More, *Opt. Lett.* **17**, 420 (1992).
- [32] A. Othonnos, A. T. Alavie, S. M. Serge, S. E. Karr, and R. M. Measures, *Opt. Eng.* **32**, 2841 (1993).
- [33] A. T. Alavie, S. E. Karr, A. Othonos, and R. M. Measures, *IEEE Photon. Technol. Lett.* **5**, 1112 (1993).
- [34] K. O. Hill, F. Bilodeau, and S. Faucher, B. Malo, and D. C. Johnson, *Electron. Lett.* **27**, 1548 (1991).
- [35] G. Laffont and P. Ferdinand, *Meas. Sci. and Tech.* **12**, 765 (2001).
- [36] J. A. R. Williams, I. Bennion, K. Sugden, and N. J. Doran, *Electron. Lett.* **30**, 985 (1994).
- [37] R. Kashyap, S. V. Chernikov, P. F. Mckee, and J. R. Taylor, *Electron. Lett.* **30**, 1078 (1994).
- [38] R. W. Fallon, L. Zhang, A. Gloag, and I. Bennion, *Electron. Lett.* **33**, 705 (1997).
- [39] M. A. Putnam, G. M. Williams, and E. J. Friebele, *Electron. Lett.* **31**, 309 (1995).
- [40] M. Leblanc, S. Y. Huang, M. Ohn, R. M. Measures, A. Guemes, and A. Othonos, *Opt. Lett.* **21**, 1405 (1996).
- [41] S. Huang, M. Leblanc, M. M. Ohn, and R. M. Measures, *Appl. Opt.* **34**, 5003 (1995).
- [42] A. M. Vengsarkar, P. J. Lemaire, J. B. Judkins, V. Bharia, T. Erdogan, and J. E. Sipe, *J.*

*Lightwave Technol.* **14**, 58 (1996).

[43] D. D. Davis, T. K. Gaylord, E. N. Glytsis, S. G. Kosinski, S. C. Mettler and A. M. Vengsarkar, *Electron. Lett.* **34**, 302 (1998).

[44] I. K. Hwang, S. H. Yun, and B. Y. Kim, *Opt. Lett.* **24**, 1263 (1999).

[45] C. Y. Lin and L. A. Wang, *IEEE Photon. Technol. Lett.* **13**, 332 (2001).

[46] F. Hindle, E. Fertein, C. Przygodzki, F. Durr, L. Paccou, R. Bocquet, P. Niay, H. G. Limberger, and M. Douay, *IEEE Photon. Technol. Lett.* **16**, 1861 (2004).

[47] A. M. Vengsarkar and V. Bharia, *Opt. Lett.* **21**, 692 (1996).

[48] S. W. James and R. P. Tatam, *Meas. Sci. and Tech.* **14**, R49 (2003).

[49] X. J. Gu, *Opt. Lett.* **23**, 509 (1998).

[50] S. Savin, M. J. F. Digonnet, G. S. Kino, and H. J. Shaw, *Opt. Lett.* **25**, 710 (2000).

[51] P. F. Wysocki, J. B. Judkins, R. P. Espindola, M. Andrejco, A. M. Vengsarkar, *IEEE Photon. Technol. Lett.* **9**, 1343 (1997).

[52] C. E. Lee, and H. F. Taylor, *Electron. Lett.* **24**, 193 (1988).

[53] P. Betts, and J. A. Davis, *Opt. Eng.* **43**, 1258 (2004).

[54] V. Bhatia, K. A. Murphy, R. O. Claus, M. E. Jones, J. L. Grace, T. A. Tran and J. A. Greene, *Smart Mater. Struct.* **4**, 240 (1995).

[55] Y. Z. Zhu, and A. B. Wang, *IEEE Photon. Technol. Lett.* **17**, 447 (2005).

[56] J. Sirkis, T. A. Berkoff, R. T. Jones, H. Singh, A. D. Kersey, E. J. Friebele, M. A. Putnam, *J. Lightwave Technol.* **13**, 1256 (1995).

[57] T. Bae, R. A. Atkins, H. F. Taylor, and W. N. Gibler, *Appl. Opt.* **42**, 1003 (2003).

[58] B. G. Grossmann and L. T. Huang, *Smart Mater. Struct.* **7**, 159 (1998).

[59] W. Peng, G. R. Pickrell, Z. Huang, J. Xu, D. W. Kim, B. Qi, and A. Wang, *Appl. Opt.* **43**, 1752 (2004).

- [60] B. Yu, D. W. Kim, J. Deng, H. Xiao, and A. Wang, *Appl. Opt.* **42**, 3241 (2003).
- [61] A. Wang, H. Xiao, J. Wang, Z. Wang, W. Zhao, and R. G. May, *J. Lightwave Technol.* **19**, 1495 (2001).
- [62] K. Murphy, M. F. Gunther, A. M. Vengsakar, and R. O. Claus, *Opt. Lett.* **16**, 273 (1991).
- [63] C. Belleville and G. Duplain, *Opt. Lett.* **18**, 78 (1993).
- [64] H. Xiao, J. D. Deng, G. Pickrell, R. G. May and A. Wang, *J. Lightwave Technol.* **21**, 2276 (2003).
- [65] G. Z. Xiao, A. Adnet, Z. Zhang, F. G. Sun, C. P. Grover, *Sensors Actuators A* **118**, 177 (2005).
- [66] J. Stone and L. W. Stulz, *Electron. Lett.* **23**, 781 (1987).
- [67] N. Park, J. W. Dawson, K. J. Vahala, and C. Miller, *Appl. Phys. Lett.* **59**, 2369 (1991)
- [68] A. D. Kersey, T. A. Berkoff, and W. W. Morey, *Opt. Lett.* **18**, 1370 (1993)
- [69] Ph. Giaccari, H. G. Limberger, and R. P. Salathé, *Opt. Lett.* **28**, 598 (2003),
- [70] P. Hamel, Y. Jaouen, R. Gabet, and S. Ramachandran, *Opt. Lett.* **32**, 1029 (2007).
- [71] X. Chapeleau, D. Leduc, C. Lupi, R. Le. Ny, M. Douay, P. Niay, and C. Boisrobert *Appl. Phys. Lett.* **82**, 4227 (2003).
- [72] D. Huang, J. Wang, C. P. Lin, C. A. Puliafito, J. G. Fujimoto, *Lasers in Surgery and Medicine* **11**, 419 (1991).
- [73] J. M. Schmitt, *IEEE J. Sel. Top. Quantum Electron.* **5**, 1205 (1999).
- [74] J. G. Fujimoto, *Nature Biotechnology* **21**, 1361 (2003).
- [75] J. G. Fujimoto and W. Drexler, eds. *Optical Coherence Tomography, Technology and Applications* (Springer-Verlag Berlin Heidelberg New York, 2008)
- [76] L. Zhao, X. G. Tu, Y. H. Zuo, S. W. Chen, and Q. M. Wang, *Appl. Phys. Lett.* **89**, 141104 (2006).

- [77] P. Chen, X. G. Tu, S. P. Li, J. C. Li, W. Lin, H. Y. Chen, D. Y. Liu, J. Y. Kang, Y. H. Zuo, L. Zhao, S. W. Chen, Y. D. Yu, J. Z. Yu, and Q. M. Wang, *Appl. Phys. Lett.* **91**, 031103 (2007).
- [78] W. Z. Song, A. Q. Liu, S. Swaminathan, C. S. Lim, P. H. Yap, and T. C. Ayi, *Appl. Phys. Lett.* **91**, 223902 (2007).
- [79] J. H. Lim, H. S. Jang, K. S. Lee, J. C. Kim, and B. H. Lee, *Opt. Lett.* **29**, 346 (2004).
- [80] J. F. Ding, A. P. Zhang, L. Y. Shao, J. H. Yan, and S. He, *IEEE Photon. Technol. Lett.* **17**, 1247 (2005).
- [81] H. Y. Choi, M. J. Kim, and B. H. Lee, *Opt. Exp.* **15**, 5711 (2007).
- [82] Z. Tian, S. S.-H. Yam, and H.-P. Loock, *IEEE Photon. Technol. Lett.* **20**, 1387 (2008).
- [83] Z. Tian and S. S. H. Yam, *IEEE Photon. Technol. Lett.* **21**, 161 (2009).
- [84] W. Tao, X. Lan, and H. Xiao, *IEEE Photon. Technol. Lett.* **21**, 669 (2009).
- [85] O. Frazao, J. Viegas, P. Caldas, J. L. Santos, F. M. Araújo, L. A. Ferreira, and F. Farahi, *Opt. Lett.* **32**, 3074 (2007).
- [86] O. Frazao, R. Falate, J. L. Fabris, J. L. Santos, L. A. Ferreira, F. M. Araújo, *Opt. Lett.* **31**, 2960 (2006).
- [87] X. Dong, L. Su, P. Shum, Y. Chung, and C. C. Chan, *Opt. Commun.* **258**, 159 (2006).
- [88] X. Yu, P. Shum, and X. Dong, *Micro. Opt. Tech. Lett.* **48**, 1379 (2006).
- [89] H. Lefevre, *The Fiber-Optic Gyroscope* (Artech House, 1993).
- [90] W. K. Burns, *Optical Fiber Rotation Sensing* (Academic Press, 1993).
- [91] E. D. L. Rosa, L. A. Zenteno, A. N. Starodumov, D. Monzon, *Opt. Lett.* **22**, 481 (1997).
- [92] A. N. Starodumov, L. A. Zenteno, D. Monzon, and E. De La Rosa, *Appl. Phys. Lett.* **70**, 19 (1997).
- [93] M. Campbell, G. Zheng, A. S. H. Smith, P. A. Wallace, *Meas. Sci. Technol.* **10**, 218 (1999).
- [94] X. Dong, H. Y. Tam, and P. Shum, *Appl. Phys. Lett.* **90**, 151113 (2007).

- [95] Y. Liu, B. Liu, X. Feng, W. Zhang, G. Zhou, S. Yuan, G. Kai, X. Dong, *Appl. Opt.* **44**, 2382 (2005).
- [96] D. Bo, Z. Qida, L. Feng, G. Tuan, X. Lifang, L. Shuhong, G. Hong, *Appl. Opt.* **45**, 7767 (2006).
- [97] O. Frazao, L. M. Marques, S. Santos, J. M. Baptista, J.L. Santos, *IEEE Photon. Technol. Lett.* **18**, 2407 (2006).
- [98] G. Sun, D. S. Moon, Y. Chung, *IEEE Photon. Technol. Lett.* **19**, 2027 (2007).
- [99] O. Frazao, J. L. Santos, J. M. Baptista, *IEEE Photon. Technol. Lett.* **19**, 1260 (2007).
- [100] O. Frazao, D. Egypto, L. Aragao-Bittencourt, M. T. M. R. Giralardi, M. B. Marques, *IEEE Photon. Technol. Lett.* **20**, 1033 (2008).
- [101] D.-P. Zhou, W. Li, W.-K. Liu and J. W. Y. Lit, *Opt. Commun.* **281**, 4640 (2008).
- [102] X. Fang, *J. Lightwave Technol.* **14**, 2250 (1996).
- [103] S. J. Spammer, P. L. Swart, and A. A. Chtcherbakov, *Microw. Opt. Technol. Lett.* **17**, 170 (1998).
- [104] S. J. Spammer, P. L. Swart, and A. Booyesen, *Appl. Opt.* **35**, 4522 (1996).
- [105] E. Ronnekleiv, *Appl. Opt.* **36**, 2076 (1997).
- [106] X. Shu, S. Jiang, and D. Huang, *IEEE Photon. Technol. Lett.* **12**, 980 (2000).
- [107] G. Das and J. W. Y. Lit, *IEEE Photon. Technol. Lett.* **16**, 60 (2004).
- [108] G. Sun, Y. Zhou, Y. Hu, and Y. Chung, *IEEE Photon. Technol. Lett.* **22**, 766 (2010).
- [109] D. S. Moon, B. H. Kim, A. Lin, G. Sun, W.-T. Han, Y.-G. Han, and Y. Chung, *Opt. Express* **15**, 8371 (2007).
- [110] C.-H. Yeh, F.-Y. Shih, C.-T. Chen, C.-N. Lee, and S. Chi, *Laser Phys. Lett.* **5**, 210 (2008).

## Chapter 2

- [1] M. G. Kuzyk, *Polymer Fiber Optics: Materials, Physics, and Applications* (CRC, Boca Raton, FL., 2006).
- [2] K. P. Chen, B. McMillen, M. Buric, C. Jewart, and W. Xu, *Appl. Phys. Lett.* **86**, 143502 (2005).
- [3] D. Graham-Rowe, *Nature Photonics* **1**, 307 (2007).
- [4] B. McMillen, C. Jewart, M. Buric, K. P. Chen, Y. Lin, and W. Xu, *Appl. Phys. Lett.* **87**, 234101 (2005).
- [5] N. Chen, B. Yun, and Y. Cui, *Appl. Phys. Lett.* **88**, 133902 (2006).
- [6] K. K. Chin, Y. Sun, G. Feng, G. E. Georgiou, K. Guo, E. Niver, H. Roman, and K. Noe, *Appl. Opt.* **46**, 7614 (2007).
- [7] C. R. Dennison and P. M. Wild, *Meas Sci. Technol.* **19**, 125301 (2008).
- [8] M. Han and A. Wang, *Opt. Lett.* **31**, 1202 (2006).
- [9] J. A. Rogers, P. Kuo, A. Ahuja, B. J. Eggleton, and E. J. Jackman, *Appl. Opt.* **39**, 5109 (2000).
- [10] L. Cashdollar and K. P. Chen, *IEEE Sen. J.* **5**, 1327 (2005).
- [11] T. L. Yeo, T. Sun, K. T. V. Grattan, D. Parry, R. Lade, and B. D. Powell, *IEEE Sensors J.* **5**, 1082 (2005).
- [12] M. Buric, K. P. Chen, M. Bhattarai, P. R. Swinehart, and M. Maklad, *IEEE Photon. Technol. Lett.* **19**, 255 (2007).
- [13] S. T. Vohra, *Optical fiber gratings applications in Handbook of Optical Fiber Sensing Technolog.* J. M. Lopez-Higuera, Ed. (Hoboken, NJ: Wiley, 2002).
- [14] Y. J. Rao, P. J. Henderson, D. A. Jackson, L. Zhang, and I. Bennion, *Electron. Lett.* **33**, 2063 (1997).

- [15] H.-K. Kang, H.-J. Bang, C.-S. Hong, and C.-G. Kim, *Meas. Sci. Technol.* **13**, 1191 (2002).
- [16] H. Xai, M. Balasubramaniam, J. Jiang, H. Luo, A. R. A. Al-khalidi, C. M. Young, and K. T. Mccarthy, U. S. Patent 7336862 (2008).
- [17] Z. Yong, C. Zhan, J. Lee, S. Yin, and P. Ruffin, *Opt. Lett.* **31**, 1794 (2006).
- [18] C. Zhan, Y. Zhu, S. Yin, and P. Ruffin, *Opt. Fiber Technol.* **13**, 98 (2007).
- [19] T. Mawatari and D. Nelson, *Smart Mater. Struct.* **17**, 035033 (2008).
- [20] R. C. Gauthier and C. Ross, *Appl. Opt.* **36**, 6264 (1997).
- [21] H. J. Patrick, *Electron. Lett.* **36**, 1763 (2000).
- [22] D. Zhao, X. Chen, K. Zhou, L. Zhang, I. Bennion, W. N. MacPherson, J. S. Barton, and J. D. C. Jones, *Appl. Opt.* **43**, 5425 (2004).
- [23] Y. P. Wang and Y. J. Rao, *IEEE Sensors J.* **5**, 839 (2005).
- [24] T. Allsop, M. Dubov, A. Martinez, F. Floreani, I. Khrushchev, D. J. Webb, and I. Bennion, *IEEE J. Lightwave Tech.* **24**, 3147 (2006).
- [25] T. Allsop, M. Dubov, A. Martinez, F. Floreani, I. Khrushchev, D. J. Webb and I. Bennion, *Electron. Lett.* **41**, 59 (2005).
- [26] F. M. Araujo, L. A. Ferreira, J. L. Santos, and F. Farahi, *Meas. Sci. Technol.* **12**, 829 (2001)
- [27] A. Martinez, Y. Lai, M. Dubov, I. Y. Khrushchev, and I. Bennion, *Electron. Lett.* **41**, 472 (2005).
- [28] L. Jin, W. Zhang, J. Li, H. Zhang, B. Liu, Q. Tu, G. Kai, and X. Dong, *Meas. Sci. Technol.* **17**, 168 (2006).
- [29] L. Prod'homme, *Phys. Chem. Glasses* **4**, 119 (1960).
- [30] A. Bertholds and R. Dandliker, *IEEE J. Lightwave Tech.* **6**, 17 (1988).
- [31] A. D. Kersey, M. A. Davis, H. J. Patrick, M. LeBlanc, K. P. Koo, C. G. Askins, M. A. Putnam, and E. J. Friebele, *IEEE J. Lightwave Tech.* **15**, 1442 (1997).

- [32] G. Meltz and W. W. Morey, *Proc. SPIE* **1516**, 185 (1991).
- [33] S. Magne, S. Rougeault, M. Vilela, and P. Ferdinand, *Appl. Opt.* **36**, 9437 (1997).
- [34] Pyralin Product Information, HD MicroSystems, (2001).
- [35] M. J. Adamson, *J. Mater. Sci.* **15**, 1736 (1980).
- [36] Y. Terui, S. -I. Matsuda, and S. Ando, *J. Polym. Sci.* **B43**, 2109 (2005).
- [37] J. L. Mrotek, M. J. Matthewson, C. R. Kurkjian, *J. Lightwave Technol.* **19**, 988 (2001).
- [38] AngstromBond 950-200 Product Information, Fiber Optic Center™, Inc.; URL: [www.focenter.com](http://www.focenter.com).
- [39] PI2525 Product Information, HD MicroSystems L.L.C.; URL: [www.hdmicrosystems.com](http://www.hdmicrosystems.com).
- [40] Ph. Giaccari, H. G. Limberger, and R. P. Salathe, *Opt. Lett.* **28**, 598 (2003).
- [41] P. Hamel, Y. Jaouen, R. Gabet, and S. Ramachandran, *Opt. Lett.* **32**, 1029 (2007).
- [42] X. Chapeleau, D. Leduc, C. Lupi, R. Le. Ny, M. Douay, P. Niay, and C. Boisrobert *Appl. Phys. Lett.* **82**, 4227 (2003).
- [43] U. Wiedmann, P. Gallion, and G. Duan, *J. Lightwave Technol.* **16**, 1343 (1998).
- [44] P. Lambelet, P. Y. Fonjallaz, H. G. Limberger, R. P. Salathk, Ch. Zimmer, and H. H. Gilgen, *IEEE Photon. Tech. Lett.* **5**, 565 (1993)
- [45] P. P. Benham, R. J. Crawford, and C. G. Armstrong, *Mechanics of Engineering Materials* (Harlow, Essex, England: Addison Wesley Longman Ltd., Second Edition, 1996), p. 191

## Chapter 3

- [1] M. G. Kuzyk, *Polymer Fiber Optics: Materials, Physics, and Applications* (CRC, Boca Raton, FL., 2006).

- [2] M. K. Davis, G. Ghisloti, S. Balsamo, D. A. S. Loeber, G. M. Smith, M. H. Hu, and H. K. Nguyen, *IEEE J. Sel. Top. Quant. Electron.* **11**, 1197 (2005).
- [3] X. Fang and R. O. Claus, *Opt. Lett.* **20**, 2146 (1995).
- [4] G. Sun, D. S. Moon, A. Lin, W.-T. Han, and Y. Chung, *Opt. Express* **16**, 3652 (2008).
- [5] X. Shu, S. Jiang, and D. Huang, *IEEE Photonics Technol. Lett.* **12**, 980 (2000).
- [6] J. S. Wey, J. Goldhar, D. W. Rush, M. W. Chbat, G. M. Carter, and G. L. Burdge, *IEEE Photon. Technol. Lett.* **7**, 152 (1995).
- [7] H. L. An, X. Z. Lin, E. Y. B. Pun, and H. D. Liu, *Opt. Commun.* **169**, 159 (1999).
- [8] H.-G. Yu, Y. Wang, Q.-Y. Xu, and C.-Q. Xu, *J. Lightw. Technol.* **24**, 1903 (2006).
- [9] D. S. Moon, B. H. Kim, A. Lin, G. Sun, W.-T. Ham, Y.-G. Han, and Y. Chung, *Opt. Express* **15**, 8371 (2007).
- [10] D.-H. Kim and J. U. Kang, *Opt. Express* **12**, 4490 (2004).
- [11] S. Kim and J. U. Kang, *IEEE Photon. Technol. Lett.* **16**, 494 (2004).
- [12] L. R. Chen, and N. Belanger, *Electron. Lett.* **41**, 178 (2005).
- [13] M. P. Fok, K. L. Lee, and C. Shu, *IEEE Photon. Technol. Lett.* **17**, 1393 (2005).
- [14] E. D. L. Rosa, L. A. Zenteno, A. N. Starodumov, D. Monzon, *Opt. Lett.* **22**, 481 (1997).
- [15] A. N. Starodumov, L. A. Zenteno, D. Monzon, and E. De La Rosa, *Appl. Phys. Lett.* **70**, 19 (1997).
- [16] M. Campbell, G. Zheng, A. S. H. Smith, P. A. Wallace, *Meas. Sci. Technol.* **10**, 218 (1999).
- [17] X. Dong, H. Y. Tam, and P. Shum, *Appl. Phys. Lett.* **90**, 151113 (2007).
- [18] Y. Liu, B. Liu, X. Feng, W. Zhang, G. Zhou, S. Yuan, G. Kai, X. Dong, *Appl. Opt.* **44**, 2382 (2005).
- [19] D. Bo, Z. Qida, L. Feng, G. Tuan, X. Lifang, L. Shuhong, G. Hong, *Appl. Opt.* **45**, 7767 (2006).

- [20] O. Frazao, L. M. Marques, S. Santos, J. M. Baptista, J. L. Santos, *IEEE Photon. Technol. Lett.* **18**, 2407 (2006).
- [21] G. Sun, D. S. Moon, Y. Chung, *IEEE Photon. Technol. Lett.* **19**, 2027 (2007).
- [22] O. Frazao, J. L. Santos, J. M. Baptista, *IEEE Photon. Technol. Lett.* **19**, 1260 (2007).
- [23] O. Frazao, D. Egypto, L. Aragao-Bittencourt, M. T. M. R. Giraldi, M. B. Marques, *IEEE Photon. Technol. Lett.* **20**, 1033 (2008).
- [24] D.-P. Zhou, W. Li, W.-K. Liu and J. W. Y. Lit, *Opt. Commun.* **281**, 4640 (2008).
- [25] X. Yang, C.-L. Zhao, Q. Peng, X. Zhou and C. Lu, *Opt. Commun.* **250**, 63 (2004).
- [26] S. Chung, J. Kim, B.-A. Yu, B. Lee, *IEEE Photon. Technol. Lett.* **13**, 1343 (2001).
- [27] O. Frazão, L. M. Marques, J. M. Baptista, *Microwave and Optical Technology Letters* **48**, 2326 (2006).
- [28] O. Frazão, J. M. Baptista, and J. L. Santos, *Sensors* **7**, 2970 (2007).
- [29] J. Noda, K. Okamoto, and Y. Sasaki, *J. Lightw. Technol.* **4**, 1071 (1986).
- [30] K. O. Hill, *Fiber Bragg gratings in Handbook of Optics IV* (New York: McGraw-Hill, 2001).

## Chapter 4

- [1] T. E. Dimmick, G. Kakarantzas, T. A. Birks, and P. St. J. Russell, *Appl. Opt.* **38**, 6845 (1999)
- [2] J. K. Chandalia, B. J. Eggleton, R. S. Windeler, S. G. Kosinski, X. Liu, and C. Xu, *IEEE Photon. Technol. Lett.* **13**, 52 (2001).
- [3] L. Yuan, J. Yang, Z. Liu, and J. Sun, *Opt. Lett.* **31**, 2692 (2006).
- [4] O. Frazao, P. Caldas, F. M. Araújo, L. A. Ferreira, and J. L. Santos, *Opt. Lett.* **32**, 1974 (2007).
- [5] Z. Tian, S. S.-H. Yam, H.-P. Loock, *IEEE Photon. Technol. Lett.* **20**, 1387 (2008).

- [6] C. C. C. Lam, R. Mandamparambil, T. Sun, K. T. V. Grattan, S. V. Nanukuttan, S. E. Taylor, P. A. M. Basheer, *IEEE Sensors J.* **9**, 525 (2009).
- [7] L. Zhao, X. G. Tu, Y. H. Zuo, S. W. Chen, and Q. M. Wang, *Appl. Phys. Lett.* **89**, 141104 (2006).
- [8] K. Q. Kieu and M. Mansuripur, *IEEE Photon. Technol. Lett.* **18**, 2239 (2006).
- [9] P. Chen, X. G. Tu, S. P. Li, J. C. Li, W. Lin, H. Y. Chen, D. Y. Liu, J. Y. Kang, Y. H. Zuo, L. Zhao, S. W. Chen, Y. D. Yu, J. Z. Yu, and Q. M. Wang, *Appl. Phys. Lett.* **91**, 031103-1 (2007).
- [10] D. K. Gramotnev and S. I. Bozhevolnyi, *Nature Photonics* **4**, 83 (2010).
- [11] W. Z. Song, A. Q. Liu, S. Swaminathan, C. S. Lim, P. H. Yap, and T. C. Ayi, *Appl. Phys. Lett.* **91**, 223902-1 (2007).
- [12] J. H. Lim, H. S. Jang, K. S. Lee, J. C. Kim, and B. H. Lee, *Opt. Lett.* **29**, 346 (2004).
- [13] J. F. Ding, A. P. Zhang, L. Y. Shao, J. H. Yan, and S. He, *IEEE Photon. Technol. Lett.* **17**, 1247 (2005).
- [14] H. Y. Choi, M. J. Kim, and B. H. Lee, *Opt. Exp.* **15**, 5711 (2007).
- [15] Z. Tian, S. S.-H. Yam, and H.-P. Loock, *IEEE Photon. Technol. Lett.* **20**, 1387 (2008).
- [16] Z. Tian and S. S. H. Yam, *IEEE Photon. Technol. Lett.* **21**, 161 (2009).
- [17] O. Frazao, P. Caldas, F. M. Araújo, L. A. Ferreira, and J. L. Santos, *Opt. Lett.* **32**, 1974 (2007).
- [18] Z. Tian, S. S.-H. Yam, and H. P. Loock, *Opt. Lett.* **33**, 105 (2008).
- [19] W. Tao, X. Lan, and H. Xiao, *IEEE Photon. Technol. Lett.* **21**, 669 (2009).
- [20] O. Frazao, J. Viegas, P. Caldas, J. L. Santos, F. M. Araújo, L. A. Ferreira, and F. Farahi, *Opt. Lett.* **32**, 3074 (2007).
- [21] O. Frazao, R. Falate, J. L. Fabris, J. L. Santos, L. A. Ferreira, F. M. Araújo, *Opt. Lett.* **31**, 2960 (2006).

- [22] X. Dong, L. Su, P. Shum, Y. Chung, and C. C. Chan, *Opt. Commun.* **258**, 159 (2006).
- [23] X. Yu, P. Shum, and X. Dong, *Micro. Opt. Tech. Lett.* **48**, 1379 (2006).
- [24] M. Born and E. Wolf, Seventh Edition, *Principles of Optics* (Cambridge University Press, Cambridge, UK, 2005).
- [25] J. Homola, ed., *Surface Plasmon Resonance Based Sensors* (Springer, Berlin Heidelberg, 2006).
- [26] O. Esteban, M. Cruz-Navarrete, A. Gonzalez-Cano, and E. Bernabeu, *Appl. Opt.* **38**, 5267 (1999).
- [27] K. Mitsui, Y. Handa, and K. Kajikawa, *Appl. Phys. Lett.* **85**, 4231 (2004).
- [28] Y.-J. He, Y.-L. Lo, and J.-F. Huang, *J. Opt. Soc. Am. B* **23**, 801 (2006).
- [29] R. Falate, O. Frazao, G. Rego, J. L. Fabris, and J. L. Santos, *Appl. Opt.* **45**, 5066 (2006).
- [30] Y.-P. Wang, D. N. Wang, W. Jin, Y.-J. Rao, and G.-D. Peng, *Appl. Phys. Lett.* **89**, 151105 (2006).
- [31] Z. He, Y. Zhu, and H. Du, *Appl. Phys. Lett.* **92**, 044105 (2008).
- [32] G. Nemova and R. Kashyap, *Opt. Lett.* **31**, 2118 (2006).
- [33] Y. Y. Shevchenko and J. Albert, *Opt. Lett.* **32**, 211 (2007).
- [34] N. Chen, B. Yun, and Y. Cui, *Appl. Phys. Lett.* **88**, 133902 (2006).
- [35] A. P. Zhang, L.-Y. Shao, J.-F. Ding, and S. He, *IEEE Photon. Technol. Lett.* **17**, 2397 (2005).
- [36] X. Chen, K. Zhou, L. Zhang, and I. Bennion, *Appl. Opt.* **44**, 178 (2005).
- [37] A. Iadicicco, S. Campopiano, A. Cutolo, M. Giordano, and A. Cusano, *Sens. Actuators B* **120**, 231 (2006).
- [38] R. Jha, J. Villatoro, and G. Badenes, *Appl. Phys. Lett.* **93**, 191106 (2008).
- [39] Z. Tian, S. S.-H. Yam, J. Barnes, W. Bock, P. Greig, J. M. Fraser, H.-P. Looock, and R. D. Oleschuk, *Photon. Technol. Lett.* **20**, 626 (2008).

- [40] F. Xu and G. Brambilla, *Appl. Phys. Lett.* **92**, 101126 (2008).
- [41] M. G. Kuzyk, *Polymer Fiber Optics: Materials, Physics, and Applications* (Boca Raton, Florida, USA: CRC Press, 2006).
- [42] D. Monzon-Hernandez, V. P. Minkovich, J. Villatoro, M. P. Kreuzer, and G. Badenes, *Appl. Phys. Lett.* **93**, 081106 (2008).
- [43] J. M. Corres, F. J. Arregui, and I. R. Matias, *J. Lightw. Technol.* **24**, 4329 (2006).
- [44] D. R. Lide, ed., 87th Edition, *Handbook of Chemistry and Physics* (CRC Press, Boca Raton, Florida, USA, 2007).
- [45] Y.-C. Kim, W. Peng, S. Banerji, and K. S. Booksh, *Opt. Lett.* **30**, 2218 (2005).
- [46] A. Martin, R. Badcock, C. Nightingale, and G. F. Fernando, *IEEE Photon. Technol. Lett.* **9**, 982 (1997).

## Chapter 5

- [1] U. Keller, *Nature* **424**, 831 (2003).
- [2] R. R. Gattass and E. Mazur, *Nature Photonics* **2**, 219 (2008).
- [3] S. C. Jones, P. Braunlich, R. T. Casper, X. A. Shen, and P. Kelly, *Opt. Eng.* **28**, 1039 (1989).
- [4] C. B. Schaffer, A. Brodeur, and E. Mazur, *Meas. Sci. Technol.* **12**, 1784 (2001).
- [5] C. W. Carr, H. B. Radousky, and S. G. Demos, *Phys. Rev. Lett.* **91**, 127402-1 (2003).
- [6] B. C. Stuart, M. D. Feit, S. Herman, A. M. Rubenchik, B. W. Shore, and M. D. Perry, *Phys. Rev. B* **53**, 1749 (1996).
- [7] X. Liu, D. Du, and G. Mourou, *IEEE J. Quant. Electron.* **33**, 1706 (1997).
- [8] D. Du, X. Liu, G. Korn, J. Squier and G. Mourou, *Appl. Phys. Lett.* **64**, 3071 (1994).
- [9] T. Q. Jia, Z. Z. Xu, R. X. Li, D. H. Feng, X. X. Li, C. F. Cheng, H. Y. Sun, N. S. Xu, and H. Z.

Wang, *J. Appl. Phys.* **95**, 5166 (2004).

[10] C. H. Fan and J. P. Longtin, *Appl. Opt.* **40**, 3124 (2001).

[11] K. M. Davis, K. Miura, N. Sugimoto, and K. Hirao, *Opt. Lett.* **21**, 1729 (1996).

[12] E. N. Glezer and E. Mazur, *Appl. Phys. Lett.* **71**, 882 (1997).

[13] Y. Wang, Y. H. Li, C. R. Liao, D. N. Wang, M. W. Yang, and P. X. Lu, *IEEE Photon. Technol. Lett.* **22**, 39 (2010).

[14] Y.-J. Rao, M. Deng, D.-W. Duan, X.-C. Yang, T. Zhu, and G.-H. Cheng, *Opt. Express* **15**, 14123 (2007).

[15] T. Wei, Y. Han, H.-L. Tsai, and H. Xiao, *Opt. Lett.* **33**, 536 (2008).

[16] T. Wei, Y. Han, Y. Li, H.-L. Tsai, and H. Xiao, *Opt. Express* **16**, 5764 (2008).

[17] Y. Wang, D. N. Wang, M. Yang, W. Hong, and P. Lu, *Opt. Lett.* **34**, 3328 (2009).

[18] Y. Wang, M. Yang, D. N. Wang, S. Liu, and P. Lu, *J. Opt. Soc. Am. B* **27**, 370 (2010).

[19] D. Marcuse, *Bell Syst. Tech. J.* **56**, 703 (1977).

[20] S. J. Mihailov, C. W. Smelser, D. Grobnic, R. B. Walker, P. Lu, H. Ding, and J. Unruh, *J. Lightw. Technol.* **22**, 94 (2004).

[21] H. C. Van de Hulst, *Light scattering by small particles* (Dover Publications, 1981).

[22] X. Shu, L. Zhang, and I. Bennion, *J. Lightw. Technol.* **20**, 255 (2002).

[23] J. Canning, *J. Sensors*, 2009, 871580 (2009).

[24] Y. Kondo, K. Nouchi, T. Mitsuyu, M. Watanabe, P. Kazansky, and K. Hirao, *Opt. Lett.* **24**, 646 (1999).

[25] SMF-28e Product Information, Corning Inc.; <http://www.corning.com>.

---

**Chapter 6**

- [1] A. M. Vengsarkar, P. J. Lemaire, J. B. Judkins, V. Bhatia, T. Erdogan, J. E. Sipe, *J. Lightwave Technol.* **14**, 58 (1996).
- [2] T. Erdogan, *J. Opt. Soc. Am. A* **14**, 1760 (1997).
- [3] V. Bhatia and A. M. Vengsarkar, *Opt. Lett.* **21**, 692 (1996).
- [4] Y. Wang, *J. Appl. Phys.* **108**, 081101 (2010).
- [5] G. Humbert, A. Malki, S. Fhvrier, P. Roy and D. Pagnoux, *Electron. Lett.* **39**, 349 (2003)
- [6] A. Malki, G. Humbert, Y. Ouerdane, A. Boukhenter, and A. Boudrioua, *Appl. Opt.* **42**, 3776 (2003).
- [7] S. Savin, M. J. Digonnet, G. S. Kino and H. J. Shaw, *Opt. Lett.* **25**, 710 (2000).
- [8] X. Yu, P. Shum, S. Fu and L. Deng, *J. Opt. Adv. Mat.* **8**, 1247 (2006).
- [9] J. H. Lim, K. S. Lee, J. C. Kim and B. H. Lee, *Opt. Lett.* **29**, 331 (2004).
- [10] Y. Kondo, K. Nouchi, T. Mitsuyu, M. Watanabe, P. Kazansky, and K. Hirao, *Opt. Lett.* **24**, 646 (1999).
- [11] E. Fertein, C. Przygodzki, H. Delbarre, A. Hidayat, M. Douay, and P. Niay, *Appl. Opt.* **40**, 3506 (2001).
- [12] F. Hindle, E. Fertein, C. Przygodzki, F. Dürr, L. Paccou, R. Bocquet, P. Niay, H. G. Limberger, and M. Douay, *IEEE Photon. Technol. Lett.* **16**, 1861 (2004).
- [13] A. I. Kalachev, V. Pureur, D. N. Nikogosyan, *Opt. Commun.* **246**, 107 (2005).
- [14] C. Caucheteur, A. Fotiadi, P. Mégret, S. A. Slattery, and D. N. Nikogosyan, *IEEE Photon. Technol. Lett.* **17**, 2346 (2005).
- [15] A. I. Kalachev, D. N. Nikogosyan, and G. Brambilla, *J. Lightwave Technol.* **23**, 2568 (2005).
- [16] T. Allsop, M. Dubov, A. Martinez, F. Floreani, I. Khrushchev, D. J. Webb, and I. Bennion, *J.*

*Lightwave Technol.* **24**, 3147 (2006).

- [17] T. Allsop, K. Kalli, K. Zhou, Y. Lai, G. Smith, M. Dubov, D. J. Webb, I. Bennion, *Opt. Commun.* **281**, 5092 (2008).
- [18] K. M. Davis, K. Miura, N. Sugimoto, and K. Hirao, *Opt. Lett.* **21**, 1729 (1996).
- [19] D. S. Starodubov, V. Grubsky, and J. Feinberg, *IEEE Photon. Technol. Lett.* **10**, 1590 (1998).
- [20] S. Choi, T. J. Eom, Y. Jung, B. H. Lee, J. W. Lee, and K. Oh, *IEEE Photon. Technol. Lett.* **14**, 1701 (2002).
- [21] Y.-G. Han, S. H. Kim, S. B. Lee, U.-C. Paek, and Y. Chung, *Electron. Lett.* **39**, 1107 (2003).
- [22] S. Choi, T. J. Eom, J. W. Yu, B. H. Lee, and K. Oh, *IEEE Photon. Technol. Lett.* **17**, 115 (2005).
- [23] H. Sakata, Y. Takata, and S. Suzuki, *IEEE Photon. Technol. Lett.* **19**, 1661 (2007).
- [24] H. Sakata, S. Suzuki, H. Ito, Y. Takata, *Opt. Fiber Technol.* **14**, 93 (2008).
- [25] K. J. Lee, D. Yeom, and B. Y. Kim, *Opt. Express* **15**, 2987 (2007).
- [26] S. Suzuki, H. Ito, Y. Takata, and H. Sakata, *Electron. Lett.* **43**, 23 (2007).
- [27] H. Sakata and H. Ito, *Opt. Commun.* **280**, 87 (2007).
- [28] M. Stevenson, C. Martelli, J. Canning, B. Ashton, and K. Lyytikainen, *Electron. Lett.* **41**, 20052649 (2005).
- [29] D. Hwang, L. V. Nguyen, D. S. Moon, and Y. Chung, *Meas. Sci. Technol.* **20**, 034020 (2009).
- [30] Y. Himei, J. Qiu, S. Nakajima, A. Sakamoto, and K. Hirao, *Opt. Lett.* **29**, 2728 (2004).
- [31] S. D. Lim, J. G. Kim, K. Lee, S. B. Lee, and B. Y. Kim, *Opt. Express* **17**, 18449 (2009).
- [32] K. McCallion, W. Johnstone, and G. Fawcett, *Opt. Lett.* **19**, 542 (1994).
- [33] F. Bakhti and P. Sansonetti, *Electron. Lett.* **32**, 581 (1996).
- [34] K. Sugden, L. Zhang, J. A. R. Williams, R. W. Fallon, L. A. Everall, K. E. Chisholm, and I. Bennion, *J. Lightw. Technol.* **15**, 1424 (1997).

- [35] Z. Wei, L. Qin, Q. Wang, H. Li, W. Zheng, Y. Zhang, *Opt. Commun.* **177**, 201 (2000).
- [36] W. S. Mohammed, P. W. E. Smith, and X. Gu, *Opt. Lett.* **31**, 2547 (2006).
- [37] V. Bhatia, D. K. Campbell, D. Sherr, T. G. D'Albarto, N. A. Zabaronick, G. A. Ten Eyck, K. A. Murphy, and R. O. Claus, *Opt. Eng.* **36**, 1872 (1997).
- [38] G. Meltz and W. W. Morey, *Proc. SPIE* **1516**, 185 (1991).
- [39] K. Shima, K. Himeno, T. Sakai, S. Okude, A. Wada, and R. Yamauchi, *Proc. Optical Fibre Communication (OFC'97) Conf.* FB2 (1997).
- [40] C. Durniak and J. D. Love, *J. Lightw. Technol.* **25**, 3634 (2007).
- [41] S. L. Logunov and M. E. DeRosa, *Electron. Lett.* **39**, 897 (2003).





